NLO QCD CORRECTIONS TO THE JET ACTIVITY IN HIGGS BOSON PRODUCTION VIA VECTOR-BOSON FUSION

by

Terrance Maynard Figy

A dissertation submitted in partial fulfillment of
the requirements for the degree of

Doctor of Philosophy

(Physics)

at the

UNIVERSITY OF WISCONSIN–MADISON

2006

To my wife.

ACKNOWLEDGMENTS

I am very thankful to have run into Professor Dieter Zeppenfeld in the hallway 6 years ago, and I thank him for taking me as a graduate student. His advice and teaching has been invaluable. You could not ask for a better advisor. I would also like to thank Professors Vernon Barger, Tao Han, and Frank Petriello for giving me their advice and support. I also would like to thank my collaborators, Carlo Oleari and Piyabut Burikam, for working with me on various projects.

I thank my wife for being patient with me throughout my years in graduate school at the University of Wisconsin-Madison. She has sacrificed much so that I could pursue a career in physics. I thank my parents for their love and support. Lastly, I would like to thank my wife's parents for all the kind things they have done for us.

DISCARD THIS PAGE

TABLE OF CONTENTS

Page

DISCARD THIS PAGE

LIST OF TABLES

DISCARD THIS PAGE

LIST OF FIGURES

Appendix
Figure Page

Appendix
Figure Page

Appendix
Figure Page

NLO QCD CORRECTIONS TO THE JET ACTIVITY IN HIGGS BOSON PRODUCTION VIA VECTOR-BOSON FUSION

Terrance Maynard Figy

Under the supervision of Professor Dieter Zeppenfeld

At the University of Wisconsin-Madison

Higgs production plus two jets via vector-boson fusion is expected to provide crucial information on the Higgs boson couplings at the CERN Large Hadron Collider. The achievable statistical accuracy demands comparison with next-to-leading order QCD calculations, which are presented here in the form of a fully flexible partonic Monte Carlo program. QCD corrections are determined for jet distributions and are shown to be modest, of the order of 5%-10% in most cases, but reaching 30% occasionally. Remaining scale uncertainties range from the order of 5% or less for distributions to below $\pm 2\%$ for the Higgs boson cross section in typical vector-boson fusion search regions.

Higgs boson production plus two jets via vector-fusion is sensitive to the tensor of the HVV ($V = W, Z$) couplings, which distinguishes loop induced vertices from SM expectations. At the CERN Large Hadron Collider this information shows up in the azimuthal angle correlations of the two forward and backward quark jets which are typical for weak boson fusion. The next-to-leading order QCD corrections to this process, in the presence of anomalous HVV couplings are computed. It is shown that gluon emission does not significantly change the azimuthal jet correlations.

For Higgs production via vector boson fusion (VBF), there is suppressed jet activity in the central region of rapidity. Higgs production via VBF in the association of three jets ($Hjjj$) is computed to NLO accuracy in QCD. K factors for $Hjjj$ are modest, typically, 1.03 to 1.06. Scale uncertainties for the total cross section at NLO are less than 5%. 3-jet ratios for Higgs production

via VBF are computed at LO and NLO. The scale dependence of 3-jet ratios is shown to be reduced at NLO.

Dieter Zeppenfeld

ABSTRACT

Higgs production plus two jets via vector-boson fusion is expected to provide crucial information on the Higgs boson couplings at the CERN Large Hadron Collider. The achievable statistical accuracy demands comparison with next-to-leading order QCD calculations, which are presented here in the form of a fully flexible partonic Monte Carlo program. QCD corrections are determined for jet distributions and are shown to be modest, of the order of 5%-10% in most cases, but reaching 30% occasionally. Remaining scale uncertainties range from the order of 5% or less for distributions to below $\pm 2\%$ for the Higgs boson cross section in typical vector-boson fusion search regions.

Higgs boson production plus two jets via vector-fusion is sensitive to the tensor of the HVV ($V = W, Z$) couplings, which distinguishes loop induced vertices from SM expectations. At the CERN Large Hadron Collider this information shows up in the azimuthal angle correlations of the two forward and backward quark jets which are typical for weak boson fusion. The next-to-leading order QCD corrections to this process, in the presence of anomalous HVV couplings are computed. It is shown that gluon emission does not significantly change the azimuthal jet correlations.

For Higgs production via vector boson fusion (VBF), there is suppressed jet activity in the central region of rapidity. Higgs production via VBF in the association of three jets ($Hjjj$) is computed to NLO accuracy in QCD. K factors for $Hjjj$ are modest, typically, 1.03 to 1.06. Scale uncertainties for the total cross section at NLO are less than 5%. 3-jet ratios for Higgs production via VBF are computed at LO and NLO. The scale dependence of 3-jet ratios is shown to be reduced at NLO.

Chapter 1

Introduction

1.1 Introduction

Assuming the Higgs boson is discovered, the measurement of its couplings to the gauge bosons and fermions will be of high importance to researchers in high energy physics. An exact determination of the properties of the Higgs-like resonance will be needed in order to definitely confirm the discovered particle is actually the Higgs boson. However, the CERN Large Hadron Collider (LHC) is a hadron collider. For Higgs production at the LHC there are a large number of QCD backgrounds. These backgrounds constitute a problem if one wants to measure Higgs boson couplings or even discover the Higgs boson. Recently, there has been a great deal of study of the vector boson fusion (VBF) process $qQ \to qQVV \to qQH$ at the LHC. The t-channel color singlet nature of the VBF process allows for background reduction, which in turn leads to higher sensitivity for the measurement of the couplings HWW and HZZ. If one wants to maximize the statistical accuracy of the LHC, it is imperative that our theoretical predictions for both the total cross section and differential cross sections involve QCD corrections. This thesis will be dedicated to the computation of one-loop QCD corrections for Higgs production via vector boson fusion.

In Section 1.2 a brief introduction to the Standard Model will be given. The Glashow-Weinberg-Salam electroweak theory will be discussed in Subsection 1.2.1. Here the *Higgs Mechanism* will be presented. In Subsection 1.2.2 the theory of Quantum Chromodynamics will be outlined. Higgs production via vector boson fusion will be discussed in Section 1.3. There will be a discussion in Section 1.4 of the *Catani-Seymour* dipole subtraction method.

1.2 The Standard Model

The Glashow-Weinberg-Salam electroweak theory [1], which is a Yang-Mills theory [2], is based on the symmetry group $SU(2)_L \times U(1)_Y$ describing the electromagnetic and weak interactions between quarks and leptons. Quantum Chromodynamics (QCD), an $SU(3)_C$ gauge theory, describes the strong interactions of the quarks and gluons [3]. The direct product of the above two groups, $SU(3)_C \times SU(2)_L \times U(1)_Y$, is known as the Standard Model (SM).

Table 1.1 The electroweak quantum numbers for the first generation of quarks and leptons.

	T_L	T_3	$\frac{1}{2}Y$	Q
ν_{eL}	$\frac{1}{2}$	$\frac{1}{2}$	$-\frac{1}{2}$	0
e_L	$\frac{1}{2}$	$-\frac{1}{2}$	$-\frac{1}{2}$	-1
u_L	$\frac{1}{2}$	$\frac{1}{2}$	$\frac{1}{6}$	$\frac{2}{3}$
d_L	$\frac{1}{2}$	$-\frac{1}{2}$	$\frac{1}{6}$	$-\frac{1}{3}$
e_R	0	0	-1	-1
u_R	0	0	$\frac{2}{3}$	$\frac{2}{3}$
d_R	0	0	$-\frac{1}{3}$	$-\frac{1}{3}$

Essential to the SM is the *Higgs mechanism* which was proposed forty years ago by Higgs, Brout, Englert, Guralnik, Hagen and Kibble [4]. The *Higgs mechanism* provides a way in which the gauge group $SU(2)_L \times U(1)_Y$ is spontaneously broken down to $U(1)_{\mathrm{EM}}$ which describes the electromagnetic interaction and in the process generates mass for gauge bosons and fermions.

1.2.1 Glashow-Weinberg-Salam Electroweak Model

The Glashow-Weinberg-Salam Electroweak model (GWS) is based on the gauge group $SU(2)_L \times U(1)_Y$[1] . There are three generations of left-handed and right-handed chiral quarks and leptons, $\psi_{L.R} = \frac{1}{2}(1 \mp \gamma_5)\psi$. The conserved quantum number associated with $SU(2)_L$ is *weak isospin* $\mathbf{T}_L$. The *weak hypercharge* quantum number Y is associated with the gauge group $U(1)_Y$. In order to incorporate the electric charge Q and unify the weak and electromagnetic interactions in a common gauge structure, $U(1)_Y$ symmetry is essential. Weak hypercharges are specified according to the formula

$$Q = T_3 + \frac{1}{2}Y. \qquad [1.1]$$

Right-handed fermions are assigned to transform under $U(1)_Y$ only whereas left-handed fermions transform under both $SU(2)_L$ and $U(1)_Y$ in a non-trivial fashion. Weak quantum numbers for the first generation of quarks and leptons are shown in Table 1.1. Due to the fact that there are equal numbers of quarks and leptons and three quark colors, chiral anomalies [5] are canceled [6] and the renormalizability of electroweak theory is preserved [7].

The gauge fields for the unbroken electroweak sector consist of the B_μ field which corresponds to the generator Y of the $U(1)_Y$ group and the three W_μ^a ($a = 1, 2, 3$) fields which correspond to the generators T^a ($a = 1, 2, 3$) of the $SU(2)_L$ group. The generators T^a are equivalent to half the Pauli matrices

$$T^a = \frac{1}{2}\tau^a \qquad [1.2]$$

with commutation relations

$$[T^a, T^b] = i\epsilon^{abc}T^c, \qquad [Y, Y] = 0 \qquad [1.3]$$

where ϵ^{abc} are antisymmetric structure constants for an $SU(2)$ group.

The unbroken $SU(2)_L \times U(1)_Y$ Lagrangian is given by

$$\mathcal{L} = -\frac{1}{4}W^{\mu\nu a}W_{\mu\nu}^a - \frac{1}{4}B^{\mu\nu}B_{\mu\nu} + \bar{\psi}i\gamma^\mu\mathcal{D}_\mu\psi \qquad [1.4]$$

with a separate fermion term for each field ψ_L and ψ_R. The covariant derivative $\mathcal{D}_\mu$ is given by

$$\mathcal{D}_\mu = \partial_\mu + ig_2W_\mu^aT^a + ig_1\frac{1}{2}B_\mu Y. \qquad [1.5]$$

The field strengths for the W and B fields are

$$W_{\mu\nu}^a = \partial_\mu W_\nu^a - \partial_\nu W_\mu^a + g_2\epsilon^{abc}W_\mu^bW_\nu^c, \qquad [1.6]$$

$$B_{\mu\nu} = \partial_\mu B_\nu - \partial_\nu B_\mu \qquad [1.7]$$

where g_2 is the coupling constant of $SU(2)_L$ and g_1 is the coupling constant of $U(1)_Y$.

The unbroken Lagrangian (Eq. (1.4)) is invariant under the infinitesimal local gauge transformations for $SU(2)_L$ and $U(1)_Y$ independently. The masses of the fermion and gauge fields are taken as zero to insure gauge invariance.

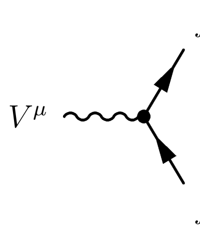

$$= -ieg_\tau^{Vf_1f_2}\gamma^\mu\frac{1}{2}(1+\tau\gamma_5)$$

Figure 1.1 qqV vertex for fermion of chirality $\tau = \pm$.

In the GWS model, the W_3 and B fields are linear combinations of the photon field A and another neutral field Z. The relation between these fields is

$$\begin{pmatrix} W_3 \\ Z \end{pmatrix} = \begin{pmatrix} \cos\theta_w & \sin\theta_w \\ -\sin\theta_w & \cos\theta_w \end{pmatrix} \begin{pmatrix} Z \\ A \end{pmatrix}, \tag{1.8}$$

where θ_w is the electroweak or *Weinberg* mixing angle. Substituting the above relation into the neutral term $i(g_2 W_{3\mu} + g_1\frac{1}{2}B_\mu Y)$ of the covariant derivative yields

$$\begin{aligned} i(g_2 W_{3\mu} + g_1\frac{1}{2}B_\mu Y) &= iA_\mu[g_2\sin\theta_w T_3 + g_1\cos\theta_w\frac{1}{2}Y] && [1.9] \\ &+ iZ_\mu[g_2\cos\theta_w T_3 - g_1\sin\theta_w\frac{1}{2}Y]. && [1.10] \end{aligned}$$

In order to unify the electromagnetic interaction with the weak interactions, the coefficient in front of the A field must be equal to $ieQ = ie(T_3 + \frac{1}{2}Y)$. This implies the following coupling relations

$$g_1 = \frac{e}{\cos\theta_w}, \qquad g_2 = \frac{e}{\sin\theta_w}. \tag{1.11}$$

The interaction of the gauge bosons and fermions shown in Figure 1.1 originates from the term $\bar\psi i\gamma^\mu D_\mu\psi$ of Eq. (1.4) which can be written as

$$-\mathcal{L}_{\rm int} = eJ^\mu_{\rm EM}A_\mu + \frac{g_1}{\sqrt{2}}\left(J_L^{+\mu}W_\mu^+ + J_L^{-\mu}W_\mu^-\right) + g_Z J_Z^\mu Z_\mu. \tag{1.12}$$

$J_L^\pm$, J_Z, and $J_{\rm EM}$ are currents with the following definitions

$$\begin{aligned} J_L^{\pm\mu} &= \sqrt{2}\bar\psi\gamma^\mu T_L^\pm\psi, && [1.13] \\ J_Z^\mu &= \bar\psi\gamma^\mu[T_{3L} - x_w Q]\psi, && [1.14] \\ J_{\rm EM}^\mu &= \bar\psi\gamma^\mu Q\psi, && [1.15] \end{aligned}$$

	T	T_3	$\frac{1}{2}Y$	Q
ϕ^+	$\frac{1}{2}$	$\frac{1}{2}$	$\frac{1}{2}$	1
ϕ^0	$\frac{1}{2}$	$-\frac{1}{2}$	$\frac{1}{2}$	1

Table 1.2 Quantum numbers

with

$$g_Z = \frac{e}{\sin\theta_w \cos\theta_w}, \qquad x_w = \sin^2\theta_w. \tag{1.16}$$

In the SM a $SU(2)$ doublet Φ of hypercharge $Y_\Phi = 1/2$ is introduced. Its self-interactions provide the mechanism for spontaneous symmetry breaking (SSB), giving rise to gauge boson and fermion masses [4] in gauge invariant fashion. Also, as the result of SSB, a new neutral scalar called the Higgs boson (H^0) arises. The isodoublet is specified to be

$$\Phi = \begin{pmatrix} \phi^+ \\ \phi^0 \end{pmatrix}, \tag{1.17}$$

with Lagrangian

$$\mathcal{L}_\Phi = (\mathcal{D}^\mu\Phi)^\dagger\mathcal{D}_\mu\Phi - \mu^2|\Phi|^2 + \lambda|\Phi|^4 \tag{1.18}$$

where $\mathcal{D}_\mu\Phi = (\partial_\mu + ig_2W_\mu^a\tau^a + ig_1Y_\Phi B_\mu)\Phi$. For $\mu^2 < 0$ in the classical theory the ground state of $|\Phi|^2$ occurs at $|\Phi|^2 = -\frac{1}{2}\mu^2/\lambda$. In quantum field theory, the field Φ develops a non-vanishing vacuum expectation value. The appearance of this non-vanishing vacuum expectation value selects a preferred direction in weak isospin plus hypercharge space and thereby “spontaneously breaks” the $SU(2)_L \times U(1)_Y$ symmetry down to $U(1)_{\text{EM}}$ which describes the electromagnetic interaction.

Here the modulus $v/\sqrt{2} = (-\mu^2/2\lambda)^{\frac{1}{2}}$ of the vacuum expectation value (vev) of $|\Phi|$ is introduced. Since conventional perturbation theory is formulated for fields with zero vev, it is appropriate to separate out the vev and to redefine the scalar doublet Φ as

$$\Phi = \begin{pmatrix} \theta_2 + i\theta_1 \\ \frac{1}{\sqrt{2}}(v+H) - i\theta_3 \end{pmatrix} = \exp\left(\frac{i\theta\cdot\tau}{v}\right)\begin{pmatrix} 0 \\ (v+H)/\sqrt{2} \end{pmatrix}, \tag{1.19}$$

where the fields θ_1, θ_2, θ_3, and H have zero vev. By a finite gauge transformation under $SU_L(2)$ with $\alpha = \theta/v$, the above phase factor can be removed from Φ. This is the "unitary gauge". The θ fields in unitary gauge become longitudinal components to the $W^\pm$ and Z^0 fields.

The covariant derivative operation on an isodoublet field expressed in terms of the physical A, $W^\pm$, and Z fields is

$$\mathcal{D} = \partial + ieQA + i\frac{1}{\sqrt{2}}g_2(\tau^+W^+ + \tau^-W^-) + ig_Z(\frac{1}{2}\tau_3 - x_wQ)Z, \qquad [1.20]$$

where the space-time index μ has been suppressed. The 2×2 matrices $\tau^\pm$ are defined as

$$\tau^+ = \sqrt{2}T^+ = \begin{pmatrix} 0 & 1 \\ 0 & 0 \end{pmatrix}, \qquad \tau^- = \sqrt{2}T^- = \begin{pmatrix} 0 & 0 \\ 1 & 0 \end{pmatrix}. \qquad [1.21]$$

In the unitary gauge Φ has only a neutral component

$$\Phi = \frac{1}{\sqrt{2}}\begin{pmatrix} 0 \\ v+H \end{pmatrix} \qquad [1.22]$$

and

$$\mathcal{D}\Phi = \frac{1}{\sqrt{2}}\begin{pmatrix} \frac{1}{\sqrt{2}}ig_2W^+(v+H) \\ \partial H - \frac{1}{2}ig_ZZ(v+H) \end{pmatrix}. \qquad [1.23]$$

By inserting Eq.(1.23) into Eq.(1.18), the Lagrangian $\mathcal{L}_\Phi$ becomes,

$$\mathcal{L}_\Phi = \frac{1}{2}(\partial H)^2 + \frac{1}{4}g_2^2W^+W^-(v+H)^2 + \frac{1}{8}g_Z^2ZZ(v+H)^2 - V\left(\frac{1}{2}(v+H)^2\right). \qquad [1.24]$$

The v^2 terms provide W and Z boson mass terms

$$M_W^2W^+W^- + \frac{1}{2}M_Z^2ZZ \qquad [1.25]$$

with

$$M_W = \frac{1}{2}gv, \qquad M_Z = \frac{1}{2}g_Zv = \frac{M_W}{\cos\theta_w}, \qquad [1.26]$$

while the photon remains massless.

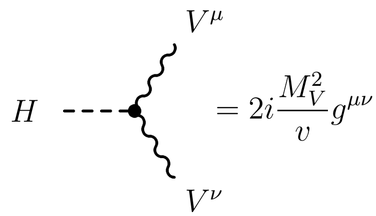

Figure 1.2 HVV vertex

The interactions between the Higgs boson, H, and the gauge bosons, W and Z, are given by the cubic and quartic terms,

$$(\frac{1}{4}g^2W^+W^- + \frac{1}{8}g_Z^2 ZZ)(H^2 + 2vH), \qquad [1.27]$$

which are completely specified by the gauge couplings. Notice, if $v = 0$ there can be no tree-level trilinear couplings of the Higgs boson to the weak bosons. Figure 1.2 shows the Feynman rule for the HVV interaction vertex.

1.2.2 Quantum Chromodynamics

Quantum Chromodynamics (QCD) is a $SU(3)$ gauge theory of quarks and gluons [3]. The Lagrangian for QCD is

$$\mathcal{L}_{\mathrm{QCD}} = -\frac{1}{4}F^a_{\mu\nu}F^{a\mu\nu} + \sum_q \bar{q}_i(i\gamma^\mu D_\mu - m_q)_{ij}q_j. \qquad [1.28]$$

The field strength $F^a_{\mu\nu}$ and the covariant derivative D_μ are given by

$$F^a_{\mu\nu} = \partial_\mu A^a_\nu - \partial_\nu A^a_\mu + g_s f^{abc}A^b_\mu A^c_\nu \qquad [1.29]$$

$$(\mathcal{D}_\mu)_{ij} = \delta_{ij}\partial_\mu + ig_s T^a_{ij}A^a_\mu \qquad [1.30]$$

$$(m_q)_{ij} = m_q\delta_{ij} \qquad [1.31]$$

where A^a_μ are the gluon fields and q_i are quark fields. f^{abc} are the structure constants and T^a_{ij} are the generators of the Lie group which defines the gauge symmetry. The structure constants f^{abc} are defined by the commutation relation

$$[T^a, T^b] = i\, f^{abc}T^c. \qquad [1.32]$$

The Lagrangian (Eq.(1.28)) is invariant under infinitesimal gauge transformations

$$q(x) \rightarrow [1 - ig_s\theta^a(x)T^a]q(x), \quad [1.33]$$

$$A^a_\mu(x) \rightarrow A^a_\mu(x) + \partial_\mu\theta^a(x) + g_s f^{abc}\theta^b(x)A^c_\mu. \quad [1.34]$$

The self-interactions of the gluons shown in Figure 1.3 arise from the non-Abelian structure of the theory and has no analogue in quantum electrodynamics (QED).

Loop integrals in QCD lead to ultraviolet divergences. These ultraviolet divergences can be absorbed through the redefinition of coupling parameters. However, renormalization introduces a dependence on an arbitrary scale μ in couplings. The renormalization scale dependence of the effective QCD coupling $\alpha_s = g_s^2/4\pi$ is controlled by the β-function,

$$\mu\frac{\partial\alpha_s}{\partial\mu} = 2\beta(\alpha_s) = -\frac{\beta_0}{2\pi}\alpha_s^2 - \frac{\beta_1}{4\pi^2}\alpha_s^3 - \ldots, \quad [1.35]$$

$$\beta_0 = 11 - \frac{2}{3}n_f, \quad [1.36]$$

$$\beta_1 = 51 - \frac{19}{3}n_f; \quad [1.37]$$

where n_f is the number of quarks less than the energy scale μ. Solution of the above differential equation requires the introduction of an integration constant. This integration constant must be determined experimentally. The most sensible choice for this constant is the value of α_s at a fixed references scale μ_0. The standard choice is $\mu_0 = m_Z$.

$$\alpha_s(\mu) = \frac{4\pi}{\beta_0 \ln(\mu^2/\Lambda^2)}\left[1 - \frac{2\beta_1}{\beta_0^2}\frac{\ln\left[\ln(\mu^2/\Lambda^2)\right]}{\ln(\mu^2/\Lambda^2)} + \ldots\right] \quad [1.38]$$

The solution above to the renormalization group equations illustrates the asymptotic freedom property: $\alpha_s \rightarrow 0$ as $\mu \rightarrow \infty$ and shows that QCD becomes a strongly coupled theory for $\mu \sim \Lambda$ [3].

1.3 Higgs Production via Vector Boson Fusion

The vector boson fusion process [1] $qq \rightarrow qqVV \rightarrow qqH$ (VBF) has the second largest production cross section to that of the gluon fusion process $gg \rightarrow H$ in the Higgs mass range

[1] The term *vector-boson fusion* (VBF) and the term *weak-boson fusion* (WBF) can be used interchangeably since the Higgs production process $qQ \rightarrow qQVV \rightarrow qQH$ involves only the weak bosons W and Z.

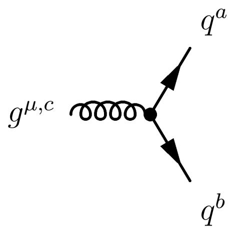

$$= -ig_s T^c_{ab}\gamma^\mu$$

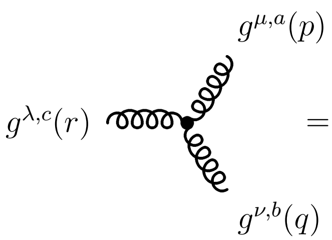

$$= ig_s f^{abc}[(p-q)_\lambda g_{\mu\nu} + (p-r)_\mu g_{\nu\lambda} + (r-p)_\nu g_{\lambda\mu}]$$

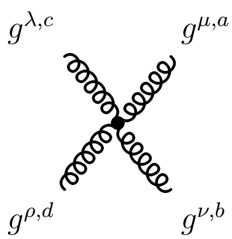

$$\begin{aligned} = -ig_s^2[&f^{abe}f^{cde}(g_{\lambda\nu}g_{\mu\rho} - g_{\lambda\rho}g_{\mu\nu}) \\ &+ f^{ace}f^{bde}(g_{\lambda\mu}g_{\nu\rho} - g_{\lambda\rho}g_{\mu\nu}) \\ &+ f^{ade}f^{bce}(g_{\lambda\mu}g_{\nu\rho} - g_{\lambda\nu}g_{\mu\rho})] \end{aligned}$$

Figure 1.3 Feynman rules for QCD. The momenta r, p, and q are incoming.

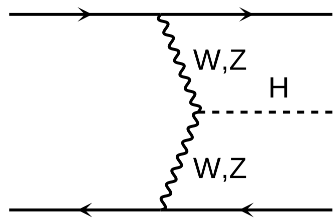

Figure 1.4 Higgs production via vector boson fusion.

$M_H \approx 100-200$ GeV. The VBF process shown in Figure 1.4 can be visualized as the exchange of a vector boson V ($V = W, Z$) in the t-channel with the Higgs boson attached to the vector boson propagator. Even though gluon fusion has the highest cross section, it is difficult to extract the Higgs boson signal out of the QCD backgrounds. Besides the issue of signal extraction for gluon fusion is the issue of theoretical uncertainty of the cross section. K-factors for gluon fusion are typically larger than 2 with a residual uncertainty of 10-20% remaining after the 2-loop corrections have been evaluated [8, 9]. However, for VBF, the situation is quite different with K-factors in the range of 1.08-1.1 over the range of Higgs mass $M_H \approx 100 - 200$ GeV with scale variation on the order of $\pm 2\%$ [10, 11, 12].

Typical for a VBF event, is the presence of two forward tagging jets which at LO corresponds to processes like $q\bar{Q} \rightarrow q\bar{Q}H$ shown in Figure 1.4. The observation of forward tagging jets in addition to any kinematic cuts on the Higgs decay products is crucial for the suppression of backgrounds [25, 26, 28, 29]. In Chapter 2, tagging jet properties for Higgs production via VBF in the association of two jets (VBF Hjj) are investigated at NLO in QCD and in Chapter 3, the NLO QCD corrections for VBF Hjj are computed in the presence of anomalous Higgs couplings. Much of the material in Chapters 2 and 3 has appeared previously in Refs. [10, 13].

Another useful technique for the suppression of QCD backgrounds to VBF is the veto of any additional jet activity in the central region of rapidity [14, 15, 16, 17, 18, 19, 20]. For VBF processes there tends to be suppressed jet activity in the central region due to t-channel color singlet exchange. Since QCD backgrounds are characterized by quark or gluon exchange in the t-channel, a veto of any additional jet activity in the central rapidity region is expected to suppress more of the backgrounds than the signal. The effect of the central jet veto has been estimated at leading order in Ref. [15]. In Chapter 4 the ratios for Higgs $+\ 3$ jet distributions to Higgs $+\ 2$ jet distributions for VBF are analyzed at next-to-leading order in QCD.

1.4 The Dipole Subtraction Method

A typical NLO cross section σ consists of three pieces: the LO (Born-level) cross section, σ^{LO}, the virtual loop corrections, σ^{V}, and the real emission corrections, σ^{R};

$$\sigma = \sigma^{LO} + \sigma^{NLO} = \int_n d\sigma^B + \int_{n+1} d\sigma^R + \int_n d\sigma^V. \qquad [1.39]$$

Phase space integrals over the $d\sigma^R$ and $d\sigma^V$ are separately divergent in $d = 4$ space-time dimensions. However, their sum in Eq.(1.39) is finite. In order to carryout the phase space integration numerically, one first needs to regulate the divergences of $d\sigma^R$ and $d\sigma^V$ separately. By carrying out the integrations in $d = 4 - 2\epsilon$ dimensions using dimensional regularization, the divergences are replaced by double (soft and collinear) poles, $1/\epsilon^2$, and single (soft, collinear, or ultraviolet) poles, $1/\epsilon$. Ultraviolet divergences are absorbed into coupling constants through the renormalization procedure. The infrared divergences of the real corrections, $d\sigma^R$, are subtracted off by a local counter-term, $d\sigma^A$. The integrated local counter-term σ^A cancels the infrared divergences of the virtual corrections. The general idea of the subtraction method is to use the identity

$$\sigma^{NLO} = \int_{n+1} d\sigma^R - \int_{n+1} d\sigma^A + \int_n \int_1 d\sigma^A + \int_n d\sigma^V, \qquad [1.40]$$

where $d\sigma^A$ is such that it has the same pointwise singular structure as $d\sigma^R$. The *Catani-Seymour* dipole subtraction method [21] provides a recipe for constructing $d\sigma^A$ for arbitrary processes. The dipole subtraction method uses an improved factorization formula for the soft and collinear divergences of the $n+1$-parton matrix elements, called dipole formulae:

$$d\sigma^A = \sum_{\text{dipoles}} d\sigma^B \otimes dV_{\text{dipole}} \qquad [1.41]$$

The notation used in Eq.(1.41) is symbolic. $d\sigma^B$ denotes an appropriate color and spin projection of the Born-level exclusive cross section. The symbol $\otimes$ denotes properly defined phase space convolutions and sums over color and spin indices. The dipole factors dV_{dipole}, which match the singular behavior of $d\sigma^R$, are completely independent of the process. The explicit form of the dipole factors are not shown here but are given in Appendix A. Introducing the phase space integration,

$$\sigma^{NLO} = \int_{n+1} \left[d\sigma^R - d\sigma^A \right] + \int_{n+1} d\sigma^A + \int_n d\sigma^V, \qquad [1.42]$$

one can safely perform the limit $\epsilon \rightarrow 0$ under the integral sign of the first term on the right-hand-side of Eq.(1.42). Now, the first term can be integrated in $d = 4$ space-time dimensions. That being the case one, can perform the phase space integration numerically.

At this stage, all of the singularities reside in the last two terms in the right-hand-side of Eq.(1.42). Now, since a convenient choice of $d\sigma^A$ has been made in Eq.(1.41), one can carry out analytically the integration of $d\sigma^A$ over the one-parton subspace. Again, using symbolic notation, one can write:

$$\int_{n+1} d\sigma^A = \sum_{\text{dipoles}} \int_n d\sigma^B \otimes \int_1 dV_{\text{dipoles}} = \int_n \left[d\sigma^B \otimes \mathbf{I} \right], \qquad [1.43]$$

where the universal factor **I** is defined as

$$\mathbf{I} = \sum_{\text{dipoles}} \int_1 dV_{\text{dipoles}}, \qquad [1.44]$$

and contains the $1/\epsilon^2$ and $1/\epsilon$ poles. These poles can be combined with poles in $d\sigma^V$ thereby canceling all divergences. After the cancellation has been carried out, one can take the limit $\epsilon \rightarrow 0$ and perform the remaining n-parton phase space integration numerically. The final structure of the calculation is

$$\sigma^{NLO} = \int_{n+1} \left[\left(d\sigma^R \right)_{\epsilon=0} - \left(\sum_{\text{dipoles}} d\sigma^B \otimes dV_{\text{dipoles}} \right)_{\epsilon=0} \right] + \int_n \left[d\sigma^V + d\sigma^B \otimes \mathbf{I} \right]_{\epsilon=0}. \qquad [1.45]$$

In Chapters 2 and 4 the dipole subtraction method described here is used to compute the next-to-leading order (NLO) QCD corrections for Higgs production in association of two and three jets via VBF.

Chapter 2

Next-to-Leading Order Jet Distributions For Higgs Boson Production Via Vector-Boson Fusion

2.1 Introduction

The vector-boson fusion (VBF) process, $qQ \to qQH$, is expected to provide a copious sources of Higgs bosons in pp-collisions at the Large Hadron Collider (LHC) at CERN. It can be visualized (see Fig. 2.1) as the elastic scattering of two (anti-)quarks, mediated by t-channel W or Z-exchange, with the Higgs boson radiated off the vector-boson propagator. Together with gluon fusion, it represents the most promising production process for Higgs boson discovery [22, 23]. Once the Higgs boson has been found and its mass determined, the measurement of its couplings to gauge bosons and fermions will be of main interest [24]. Here VBF will be of central importance since it allows for independent observation in the $H \to \tau\tau$ [25], $H \to WW$ [17, 26, 27], $H \to \gamma\gamma$ [28] and $H \to$ invisible [29] channels. This multitude of channels is crucial for separating the effects of different Higgs boson couplings.

The VBF measurements can be performed at the LHC with statistical accuracies on cross sections times decay branching ratios, $\sigma \cdot B$, reaching 5 to 10% [24]. In order to extract Higgs boson coupling constants with this full statistical power, a theoretical prediction of the Standard Model (SM) production cross section with error well below 10% is required, and this clearly entails knowledge of the next-to-leading order (NLO) QCD corrections.

For the total Higgs boson production cross section via VBF these NLO corrections have been available for a decade [12] and they are relatively small, with K-factors around 1.05 to 1.1. These modest K-factors are another reason for the importance of Higgs boson production via VBF: theoretical uncertainties will not limit the precision of the coupling measurements. This is in contrast to the dominant gluon fusion channel where the K-factor is larger than 2 and residual uncertainties of 10-20% remain, even after the 2-loop corrections have been evaluated [8, 9].

In order to distinguish the VBF Higgs boson signal from backgrounds, stringent cuts are required on the Higgs boson decay products as well as on the two forward quark jets which are characteristic for VBF. Typical cuts have an acceptance of less than 25% of the starting value for $\sigma \cdot B$. The question then arises whether the K-factors and the scale dependence determined for the inclusive production cross section [12] are valid for the Higgs boson search region also. This is best addressed by implementing the one-loop QCD corrections in a fully flexible NLO parton-level Monte Carlo program.

The purpose of this Chapter then is twofold. First, we use the Higgs boson signal process as our example to discuss the generic features of NLO QCD corrections to VBF processes. We use the subtraction method of Catani and Seymour [21] throughout. In Section 2.2 we describe the handling of real emission singularities. We give explicit formulas for the finite contributions which remain after factorization of the initial-state collinear singularities and after cancellation of divergences produced by soft and collinear final-state gluons against the corresponding terms in the virtual corrections.

This procedure yields a regularized Monte Carlo program which allows us to determine infrared safe observables at NLO. The main features of the program, numerical tests, and parameters to be used in the later phenomenological discussion are described in Section 2.3. In Section 2.4 we then use this tool to address our second objective, a discussion of the QCD radiative corrections as a function of jet observables. We determine the K-factors and the residual scale uncertainties for distributions of the tagging jets which represent the scattered quarks in VBF. In addition, we quantify the cross section error induced by uncertainties in the determination of parton distribution functions (pdf's). Pdf errors and scale variations in the phase-space regions relevant for the Higgs boson search turn out to be quite small (approximately 4% when combined) and thus indicate the small theoretical uncertainties required for reliable coupling measurements. Conclusions are presented in Section 2.5.

2.2 Subtraction terms for soft and collinear radiation

At lowest order, Higgs boson production via vector-boson fusion is represented by a single Feynman graph, like the one depicted in Fig. 2.1(a) for $\bar{q}Q\to\bar{q}QH$. We use this particular process to describe the QCD radiative corrections. Generalization to crossed processes ($\bar{q}\to q$ and/or $Q\to\bar{Q}$) is straightforward. Strictly speaking, the single Feynman graph picture is valid for different quark flavors on the two fermion lines only. For identical flavors annihilation processes, like $\bar{q}q\to Z^*\to ZH$ with subsequent decay $Z\to\bar{q}q$ or similar WH production channels, contribute as

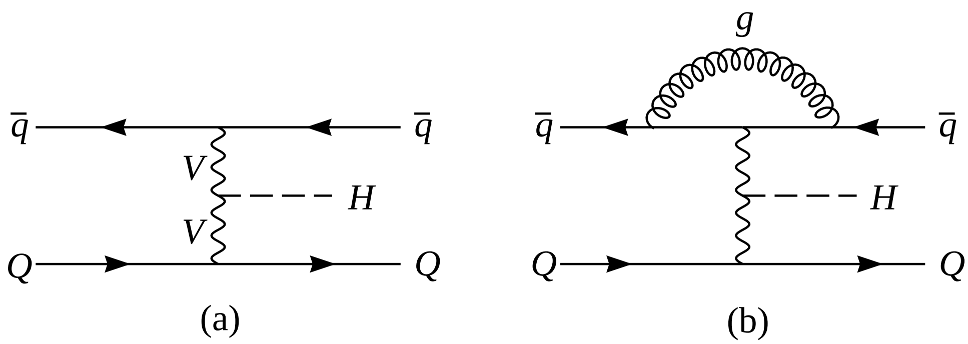

Figure 2.1 Feynman graphs contributing to $\bar{q}Q\rightarrow\bar{q}QH$ at (a) tree level and (b) including virtual corrections to the upper quark line.

well. For $qq\rightarrow qqH$ or $\bar{q}\bar{q}\rightarrow\bar{q}\bar{q}H$ the interchange of identical quarks in the initial or final state needs to be considered in principal. However, in the phase-space regions where VBF can be observed experimentally, with widely separated quark jets of very large invariant mass, the interference of these additional graphs is strongly suppressed by large momentum transfer in the vector-boson propagators. Color suppression further makes these effects negligible. In the following we systematically neglect any identical fermion effects.

At NLO, the vertex corrections of Fig. 2.1(b) and the real emission diagrams of Fig. 2.2 must be included. Because of the color singlet nature of the exchanged vector boson, any interference terms between sub-amplitudes with gluons attached to both the upper and the lower quark lines vanish identically at order α_s. Hence, it is sufficient to consider radiative corrections to a single quark line only, which we take here as the upper one. Corrections to the lower fermion line are an exact copy. We denote the amplitude for the real emission process

$$\bar{q}(p_a) + Q(p_b)\rightarrow g(p_1) + \bar{q}(p_2) + Q(p_3) + H(P) \qquad [2.1]$$

depicted in Fig. 2.2(a) and (b) as $\mathcal{M}_r^{\bar{q}} = \mathcal{M}_r^{\bar{q}}(p_a, p_1, p_2; q)$, where $q = p_1 + p_2 - p_a$ is the four momentum of the virtual vector boson, V, of virtuality $Q^2 = -q^2$.

The 3-parton phase-space integral of $|\mathcal{M}_r^{\bar{q}}|^2$ suffers from soft and collinear divergences. They are absorbed in a single counter term, which, in the notation of Ref. [21], contains the two dipole

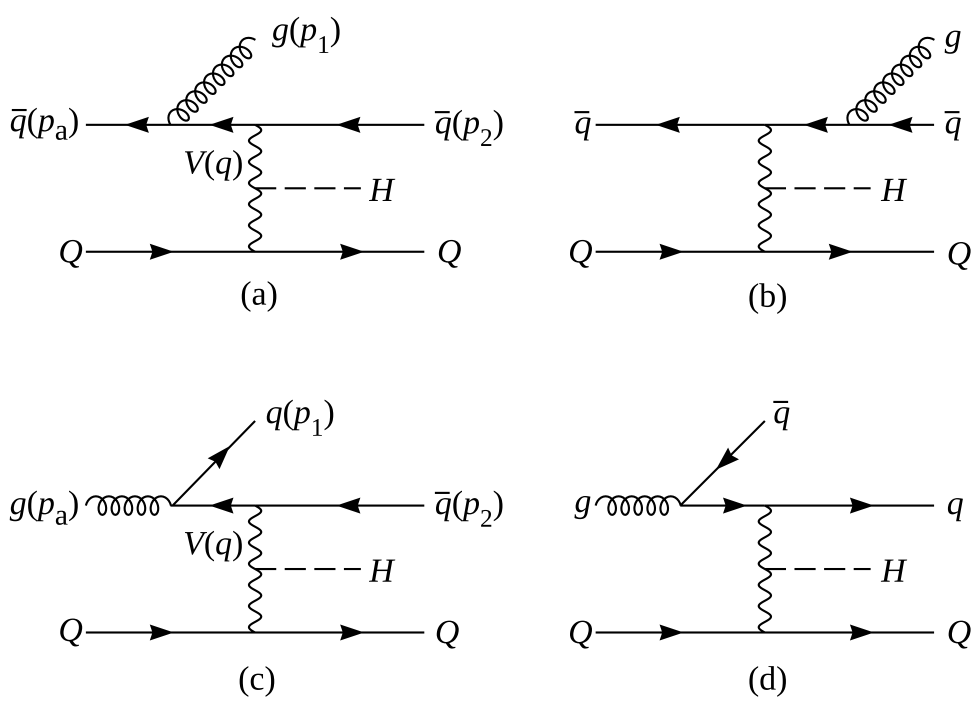

Figure 2.2 Real emission contributions to Higgs boson production via vector-boson fusion. Corrections for the upper quark line only are shown: gluon radiation ((a) and (b)) and gluon initiated processes ((c) and (d)).

factors $\mathcal{D}_2^{\bar{q}1}$ and $\mathcal{D}_{12}^{\bar{q}}$

$$|\mathcal{M}^{\bar{q}}|^2_{\rm sing} = \mathcal{D}_2^{\bar{q}1} + \mathcal{D}_{12}^{\bar{q}} = 8\pi\alpha_s(\mu_R)\, C_F\, \frac{1}{Q^2}\, \frac{x^2+z^2}{(1-x)(1-z)} \left|\mathcal{M}_B^{\bar{q}}\right|^2 , \qquad [2.2]$$

where $C_F = \frac{4}{3}$ and $\mathcal{M}_B^{\bar{q}} = \mathcal{M}_B^{\bar{q}}(\tilde{p}_a, \tilde{p}_2; q)$ is the Born amplitude for the lowest order process

$$\bar{q}(\tilde{p}_a) + Q(p_b) \rightarrow \bar{q}(\tilde{p}_2) + Q(p_3) + H(P) , \qquad [2.3]$$

evaluated at the phase-space point

$$\tilde{p}_a = x p_a , \qquad \tilde{p}_2 = p_1 + p_2 - (1-x) p_a , \qquad [2.4]$$

with

$$x = 1 - \frac{p_1 \cdot p_2}{(p_1 + p_2)\cdot p_a} , \qquad [2.5]$$
$$z = 1 - \frac{p_1 \cdot p_a}{(p_1 + p_2)\cdot p_a} = \frac{p_2 \cdot p_a}{(p_1 + p_2)\cdot p_a} . \qquad [2.6]$$

This choice continuously interpolates between the singularities due to final-state soft gluons ($p_1 \rightarrow 0$ corresponding to $x \rightarrow 1$ and $z \rightarrow 1$), collinear final-state partons ($p_1 || p_2$ resulting in $p_1 \cdot p_2 \rightarrow 0$ or $x \rightarrow 1$) and gluon emission collinear to the initial-state anti-quark ($p_1 \rightarrow (1-x) p_a$ and $z \rightarrow 1$). The subtracted real emission amplitude squared, $|\mathcal{M}_r^{\bar{q}}|^2 - |\mathcal{M}^{\bar{q}}|^2_{\rm sing}$, leads to a finite phase-space integral of the real parton emission cross section

$$\sigma_3^{NLO}(\bar{q}Q \rightarrow \bar{q}QHg) = \int_0^1 dx_a \int_0^1 dx_b\, f_{\bar{q}/p}(x_a, \mu_F)\; f_{Q/p}(x_b, \mu_F)\; \frac{1}{2\hat{s}}\, d\Phi_4(p_1, p_2, p_3, P; p_a + p_b)$$
$$\times \left\{ |\mathcal{M}_r^{\bar{q}}|^2\, F_J^{(3)}(p_1, p_2, p_3) - |\mathcal{M}^{\bar{q}}|^2_{\rm sing}\, F_J^{(2)}(\tilde{p}_2, p_3) \right\} , \qquad [2.7]$$

where $\hat{s} = (p_a + p_b)^2$ is the center-of-mass energy. The functions $F_J^{(3)}$ and $F_J^{(2)}$ define the jet algorithm for 3-parton and 2-parton final states and we obviously need $F_J^{(3)} \rightarrow F_J^{(2)}$ in the singular limits discussed above, i.e. the jet algorithm (and all observables) must be infrared and collinear safe. Being finite, the phase-space integral of Eq. (2.7) is evaluated numerically in $D = 4$ dimensions. Similarly, for the gluon initiated process

$$g(p_a) + Q(p_b) \rightarrow q(p_1) + \bar{q}(p_2) + Q(p_3) + H(P) , \qquad [2.8]$$

the singular behavior for $g \to q\bar{q}$ splitting is absorbed into the singular counter term

$$|\mathcal{M}^g|^2_{\rm sing} = \mathcal{D}_2^{g1} + \mathcal{D}_1^{g2} \;=\; 8\pi\alpha_s(\mu_R)\, T_F\, \frac{1}{Q^2}\left[\frac{x^2+(1-x)^2}{1-z}\left|\mathcal{M}_B^{\bar{q}}\left(\tilde{p}_a,\tilde{p}_2;q\right)\right|^2 + \frac{x^2+(1-x)^2}{z}\left|\mathcal{M}_B^{q}\left(\tilde{p}_a,\tilde{p}_2;q\right)\right|^2\right], \quad [2.9]$$

where $T_F = \frac{1}{2}$ and $\mathcal{M}_B^{\bar{q}}$ and $\mathcal{M}_B^{q}$ denote the Born amplitudes for the leading-order (LO) processes $\bar{q}(\tilde{p}_a) + Q(p_b) \to \bar{q}(\tilde{p}_2) + Q(p_3) + H(P)$ and $q(\tilde{p}_a) + Q(p_b) \to q(\tilde{p}_2) + Q(p_3) + H(P)$, respectively. The subtraction of $|\mathcal{M}^g|^2_{\rm sing}$ from the real emission amplitude squared leads to a contribution to the subtracted 3-parton cross section analogous to the one given in Eq. (2.7).

The singular counter terms are integrated analytically, in $D = 4-2\epsilon$ dimensions, over the phase space of the collinear and/or soft final-state parton. Integrating Eq. (2.2) yields the contribution (we are using the notation of Ref. [21])

$$< I(\epsilon) >= |\mathcal{M}_B^{\bar{q}}|^2 \frac{\alpha_s(\mu_R)}{2\pi} C_F \left(\frac{4\pi\mu_R^2}{Q^2}\right)^{\epsilon} \Gamma(1+\epsilon)\left[\frac{2}{\epsilon^2} + \frac{3}{\epsilon} + 9 - \frac{4}{3}\pi^2\right] . \quad [2.10]$$

We have regularized the divergences using dimensional reduction. If we had used conventional dimensional regularization we would have obtained a finite piece equal to $(10 - 4\pi^2/3)$. The $1/\epsilon^2$ and $1/\epsilon$ divergences cancel against the poles of the virtual correction, depicted in Fig. 2.1(b). For the case at hand, the virtual correction amplitude $\mathcal{M}_V$ is particularly simple, leading to the divergent interference term

$$2{\rm Re}\left[\mathcal{M}_V \mathcal{M}_B^*\right] = |\mathcal{M}_B^{\bar{q}}|^2 \frac{\alpha_s(\mu_R)}{2\pi} C_F \left(\frac{4\pi\mu_R^2}{Q^2}\right)^{\epsilon} \Gamma(1+\epsilon)\left[-\frac{2}{\epsilon^2} - \frac{3}{\epsilon} + c_{\rm virt}\right] . \quad [2.11]$$

Here we have included the finite contribution of the virtual diagram which is proportional to the Born amplitude. In dimensional reduction this contribution is given by $c_{\rm virt} = \pi^2/3 - 7$ ($c_{\rm virt} = \pi^2/3 - 8$ in conventional dimensional regularization).

Summing together the contributions from Eq. (2.10) and Eq. (2.11), we obtain the following finite 2-parton contribution to the NLO cross section

$$\sigma_2^{NLO}(\bar{q}Q \to \bar{q}QH) = \int_0^1 dx_a \int_0^1 dx_b\, f_{\bar{q}/p}\left(x_a,\mu_F\right)\, f_{Q/p}\left(x_b,\mu_F\right)\, \frac{1}{2\hat{s}}\, d\Phi_3\left(p_2,p_3,P;p_a+p_b\right) \times \left|\mathcal{M}_B^{\bar{q}}\right|^2 F_J^{(2)}(p_2,p_3)\left[1 + \frac{\alpha_s(\mu_{Ra}) + \alpha_s(\mu_{Rb})}{2\pi}\, C_F\left(9 - \frac{4}{3}\pi^2 + c_{\rm virt}\right)\right]. \quad [2.12]$$

The two α_s terms, at distinct renormalization scales μ_{Ra} and μ_{Rb}, correspond to virtual corrections to the upper and the lower fermion line in Fig. 2.1, respectively, and we have anticipated the possibility of using different scales (like the virtuality of the attached vector boson V) for the QCD corrections to the two fermion lines.

The remaining divergent piece of the integral of the counter terms in Eqs. (2.2) and (2.9) is proportional to the P^{qq} and P^{gq} splitting functions and disappears after renormalization of the parton distribution functions. The surviving finite collinear terms are given by

$$\begin{aligned}\sigma_{2,\mathrm{coll}}^{NLO}(\bar{q}Q\to\bar{q}QH) &= \int_0^1 dx_a \int_0^1 dx_b\, f_{\bar{q}/p}^c(x_a,\mu_F,\mu_{Ra})\ f_{Q/p}(x_b,\mu_F) \\ &\quad\times\frac{1}{2\hat{s}}\, d\Phi_3(p_2,p_3,P;p_a+p_b)\left|\mathcal{M}_B^{\bar{q}}\right|^2 F_J^{(2)}(p_2,p_3)\ , \qquad [2.13]\end{aligned}$$

and similarly for quark initiated processes. Here the anti-quark function $f_{\bar{q}/p}^c(x,\mu_F,\mu_R)$ is given by

$$\begin{aligned}f_{\bar{q}/p}^c(x,\mu_F,\mu_R) &= \frac{\alpha_s(\mu_R)}{2\pi}\int_x^1 \frac{dz}{z}\left\{f_{g/p}\left(\frac{x}{z},\mu_F\right)A(z)\right. \\ &\quad+\left[f_{\bar{q}/p}\left(\frac{x}{z},\mu_F\right)-zf_{\bar{q}/p}(x,\mu_F)\right]B(z)+\left.f_{\bar{q}/p}\left(\frac{x}{z},\mu_F\right)C(z)\right\} \\ &\quad+\frac{\alpha_s(\mu_R)}{2\pi}f_{\bar{q}/p}(x,\mu_F)D(x)\ , \qquad [2.14]\end{aligned}$$

with the integration kernels

$$A(z) = T_F\left[z^2+(1-z)^2\right]\ln\frac{Q^2(1-z)}{\mu_F^2 z}+2T_F\, z(1-z)\ , \qquad [2.15]$$

$$B(z) = C_F\left[\frac{2}{1-z}\ln\frac{Q^2(1-z)}{\mu_F^2}-\frac{3}{2}\frac{1}{1-z}\right]\ , \qquad [2.16]$$

$$C(z) = C_F\left[1-z-\frac{2}{1-z}\ln z-(1+z)\ln\frac{Q^2(1-z)}{\mu_F^2 z}\right]\ , \qquad [2.17]$$

$$D(x) = C_F\left[\frac{3}{2}\ln\frac{Q^2}{\mu_F^2(1-x)}+2\ln(1-x)\ln\frac{Q^2}{\mu_F^2}+\ln^2(1-x)+\pi^2-\frac{27}{2}-c_{\mathrm{virt}}\right]. \qquad [2.18]$$

Note that c_{virt} exactly cancels between the contributions from Eq. (2.12) and Eq. (2.18). This fact will be used below to numerically test our program.

The same kernels define the quark functions $f_{q/p}^c(x,\mu_F,\mu_R)$, which appear with the Born amplitude $\mathcal{M}_B^q(p_a,p_2;q)$ in the analog of Eq. (2.13) for the $qQ\to qQH$ processes. The gluon distribution $f_{g/p}(x,\mu_f)$ thus appears twice, multiplying the Born amplitudes squared $|\mathcal{M}_B^q|^2$ and $|\mathcal{M}_B^{\bar{q}}|^2$

in the quark and anti-quark functions. These two terms correspond to the two terms in Eq. (2.9), after the $1/\epsilon$ collinear divergences have been factorized into the NLO parton distributions.

Formulae identical to the ones given above for corrections to the upper line in the diagrams of Fig. 2.2 apply to the case where the gluon is attached to the lower line (with $a \leftrightarrow b$, $p_2 \leftrightarrow p_3$). As for the renormalization scale μ_R in Eq. (2.12), we distinguish between the two factorization scales that appear for the upper and lower quark lines, calling them μ_{Fa} and μ_{Fb}, when needed.

A second class of gluon initiated processes arises from crossing the final-state gluon and the initial-state quark Q in the Feynman graphs of Fig. 2.2(a) and (b). The resulting process can be described as $g\bar{q}\to\bar{q}VH$ with the virtual vector boson V undergoing the hadronic decay $V\to Q\bar{Q}$. Such contributions are part of the radiative corrections to $\bar{q}q\to VH$, they are suppressed in the VBF search regions with their large dijet invariant mass, and we do not include them in our calculation.

2.3 The NLO parton Monte Carlo program

The cross section contributions discussed above for the $\bar{q}Q\to\bar{q}QH$ process and crossing related channels have been implemented in a parton-level Monte Carlo program. The tree-level amplitudes are calculated numerically, using the helicity-amplitude formalism of Ref. [30]. The Monte Carlo integration is performed with a modified version of VEGAS [31].

The subtraction method requires the evaluation of real-emission amplitudes and, simultaneously, Born amplitudes at related phase-space points (see e.g. Eqs. (2.7) and (2.13)). In order to speed up the program, the contributions from σ_3^{NLO} and $\sigma_{2,\text{coll}}^{NLO}$ are calculated in parallel, as part of the 3-parton phase-space integral. Since the phase-space element factorizes [21],

$$\int d\Phi_4\left(p_1,p_2,p_3,P;p_a+p_b\right) = \int_0^1 dx \int_0^1 dz\, d\Phi_3\left(\tilde{p}_2,p_3,P;xp_a+p_b\right)\frac{Q^2}{16\pi^2 x}\,, \qquad [2.19]$$

we can rewrite the finite collinear term of Eq. (2.13) as

$$\begin{aligned}\sigma_{2,\text{coll}}^{NLO}\left(\bar{q}Q\to\bar{q}QH\right) \;=\;& \int_0^1 dx_a \int_0^1 dx_b\, \frac{1}{2(p_a+p_b)^2}\, d\Phi_4\left(p_1,p_2,p_3,P;p_a+p_b\right) \\ &\times\Bigg\{ f_{g/p}(x_a,\mu_F)A(x) + f_{\bar{q}/p}(x_a,\mu_F)\Big[B(x)+C(x)\Big] \\ &\quad + x f_{\bar{q}/p}(xx_a,\mu_F)\left[\frac{D(xx_a)}{1-xx_a} - B(x)\right]\Bigg\}\end{aligned}$$

$$\times f_{Q/p}\left(x_b, \mu_F\right) \; \frac{8\pi\alpha_s(\mu_R)}{Q^2} \left|\mathcal{M}_B^{\bar{q}}\right|^2 F_J^{(2)}\left(\tilde{p}_2, p_3\right) \;, \qquad [2.20]$$

where x and z are determined as in Eqs. (2.5) and (2.6). Equation (2.20) allows for stringent consistency checks of our program, since we can determine the finite collinear cross section either as part of the 2-parton or as part of the 3-parton phase-space integral. For example, because of the cancellation of $c_{\rm virt}$ mentioned below Eq. (2.18), the final result cannot depend on its value. We have checked this independence numerically, at the 3×10^{-4} level. Another method to test the program is to determine the (anti-)quark functions $f^c_{a/p}(x, \mu_F, \mu_R)$ by numerical integration of Eq. (2.14), to then compute the finite collinear cross section together with the Born cross section, and to compare with the results of Eq. (2.20). For all phase-space regions considered, our numerical program passes this test, with relative deviations of less than 2×10^{-4} of the total Higgs boson cross section, which is the level of the Monte Carlo error.

As a final check we have compared our total Higgs boson cross section with previous analytical results [12], as calculated with the program of Spira [32]. We find agreement at or below the 1×10^{-3} level which is inside the Monte Carlo accuracy for this comparison.

The cross sections to be presented below are based on CTEQ6M parton distributions [33] with $\alpha_s(M_Z) = 0.118$ for all NLO results and CTEQ6L1 parton distributions with $\alpha_s(M_Z) = 0.130$ for all leading order cross sections. For all Z-exchange contributions, the b-quark is included as an initial and/or final-state massless parton. The b-quark contributions are quite small, however, affecting the Higgs boson production cross section at the 3% level only. We choose $m_Z = 91.188$ GeV, $\alpha_{QED} = 1/128.93$ and the measured value of G_F as our electroweak input parameters from which we obtain $m_W = 79.96$ GeV and $\sin^2\theta_W = 0.2310$, using LO electroweak relations. In order to reconstruct jets from the final-state partons, the k_T-algorithm [34] as described in Ref. [35] is used, with resolution parameter $D = 0.8$.

2.4 Tagging jet properties at NLO

The defining feature of vector-boson fusion events at hadron colliders is the presence of two forward tagging jets, which, at LO, correspond to the two scattered quarks in the process $qQ \to qQH$.

Their observation, in addition to exploiting the properties of the Higgs boson decay products, is crucial for the suppression of backgrounds [17, 25, 26, 27, 28, 29]. The stringent acceptance requirements imply that tagging jet distributions must be known precisely for a reliable prediction of the SM Higgs signal rate. Comparison of the observed Higgs production rate with this SM cross section, within cuts, then allows us to determine Higgs boson couplings [24] and, thus, the theoretical error of the SM cross section directly feeds into the uncertainty of measured couplings.

The NLO corrections to the Higgs boson cross section do not depend on the phase space of the Higgs boson decay products because the Higgs boson, as a scalar, does not induce any spin correlations. It is therefore sufficient to analyze tagging jet distributions to gain a reliable impression of the size and the uncertainties of higher order QCD corrections. Since search strategies depend on the decay mode considered and will evolve with time, we here consider generic vector-boson fusion cuts only. They are chosen, however, to give a good approximation of the cuts suggested for specific Higgs boson search channels at the LHC. The phase space dependence of the QCD corrections and uncertainties, within these cuts, should then provide a reasonably complete and reliable picture.

Using the k_T-algorithm, we calculate the partonic cross sections for events with at least two hard jets, which are required to have

$$p_{Tj} \geq 20\ \mathrm{GeV}\,, \qquad\qquad |y_j| \leq 4.5\,. \tag{2.21}$$

Here y_j denotes the rapidity of the (massive) jet momentum which is reconstructed as the four-vector sum of massless partons of pseudorapidity $|\eta| < 5$. The Higgs boson decay products (generically called "leptons" in the following) are required to fall between the two tagging jets in rapidity and they should be well observable. While an exact definition of criteria for the Higgs boson decay products will depend on the channel considered, we here substitute such specific requirements by generating isotropic Higgs boson decay into two massless "leptons" (which represent $\tau^+\tau^-$ or $\gamma\gamma$ or $b\bar{b}$ final states) and require

$$p_{T\ell} \geq 20\ \mathrm{GeV}\,, \qquad |\eta_\ell| \leq 2.5\,, \qquad \triangle R_{j\ell} \geq 0.6\,, \tag{2.22}$$

where $R_{j\ell}$ denotes the jet-lepton separation in the rapidity-azimuthal angle plane. In addition the two "leptons" are required to fall between the two tagging jets in rapidity

$$y_{j,min} < \eta_{\ell_{1,2}} < y_{j,max} \, . \tag{2.23}$$

We do not specifically require the two tagging jets to reside in opposite detector hemispheres for the present analysis. Note that no reduction due to branching ratios for specific final states is included in our calculation: the cross section without any cuts corresponds to the total Higgs boson production cross section by vector-boson fusion.

At LO, the signal process has exactly two massless final-state quarks, which are identified as the tagging jets, provided they pass the k_T-algorithm and the cuts described above. At NLO these jets may be composed of two partons (recombination effect) or we may encounter three well-separated partons, which satisfy the cuts of Eq. (2.21) and would give rise to three-jet events. As with LHC data, a choice needs to be made for selecting the tagging jets in such a multijet situation. We consider here the following two possibilities:

1) Define the tagging jets as the two highest p_T jets in the event. This ensures that the tagging jets are part of the hard scattering event. We call this selection the "p_T-method" for choosing tagging jets.

2) Define the tagging jets as the two highest energy jets in the event. This selection favors the very energetic forward jets which are typical for vector-boson fusion processes. We call this selection the "E-method" for choosing tagging jets.

Backgrounds to vector-boson fusion are significantly suppressed by requiring a large rapidity separation of the two tagging jets. As a final cut, we require

$$\Delta y_{jj} = |y_{j_1} - y_{j_2}| > 4 \, , \tag{2.24}$$

which will be called the "rapidity gap cut" in the following.

Cross sections, within the cuts of Eqs. (2.21)–(2.24), are shown in Fig. 2.3(a), as a function of the Higgs boson mass, m_H. As for the total VBF cross section, the NLO effects are modest for

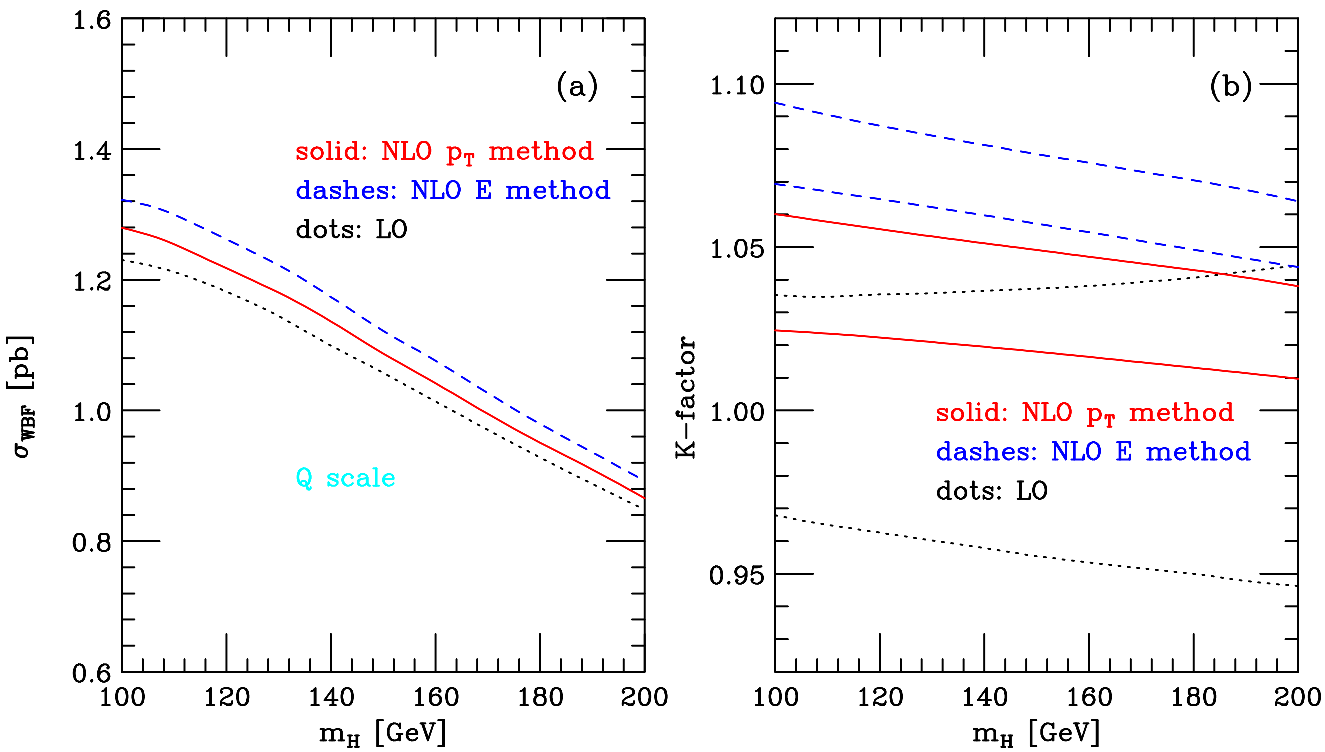

Figure 2.3 Effect of QCD radiative corrections on the Higgs boson production cross section via VBF, as a function of the Higgs boson mass, m_H. Results are given at LO (black dotted) and at NLO for the p_T-method (solid red) and the E-method (dashed blue) for defining tagging jets. Panel (a) gives the total cross section within the cuts of Eqs. (2.21)–(2.24). The corresponding scale dependence, for variation of μ_R and μ_F by a factor of 2, is shown in panel (b). See text for details.

the cross section within cuts, amounting to a 3-5% increase for the p_T-method of selecting tagging jets (solid red) and a 6-9% increase when the E-method is used[1]. These K-factors, and their scale dependence, are shown in Fig. 2.3(b). Here the K-factor is defined as

$$K = \frac{\sigma(\mu_R, \mu_F)}{\sigma^{LO}(\mu_F = Q_i)} \ , \qquad [2.25]$$

i.e. the cross section is normalized to the LO cross section, determined with CTEQ6L1 parton distributions, and a factorization scale which is set to the virtuality of the vector boson which is attached to a given quark line.

We have investigated two general scale choices. First we consider the Higgs boson mass as the relevant hard scale, i.e. we set

$$\mu_F = \xi_F m_H \ , \qquad \mu_R = \xi_R m_H \ . \qquad [2.26]$$

As a second option, we consider the virtuality of the exchanged vector boson. Specifically, independent scales Q_i are determined for radiative correction on the upper and the lower quark line, and we set

$$\mu_{Fi} = \xi_F Q_i \ , \qquad \mu_{Ri} = \xi_R Q_i \ . \qquad [2.27]$$

This choice is motivated by the picture of VBF as two independent DIS events, with independent radiative corrections on the two electrovector boson vertices. In general we find the largest scale variations when we vary the renormalization scale and the factorization scale in the same direction. We only show results for this case, $\xi = \xi_R = \xi_F$, in the following. The curves in Fig. 2.3(b) correspond to the largest variations found for $\xi = 1/2$ and $\xi = 2$ when considering both scale choices simultaneously. The residual scale uncertainty is about $\pm 5\%$ at LO and reduces to below $\pm 2\%$ at NLO.

In addition to missing higher order corrections, the theoretical error of the VBF cross section is dominated by uncertainties in the determination of the parton distribution functions. We have

[1]The larger cross section for the E-method is due to events with a fairly energetic extra central jet. A veto on central jets of $p_{Tj} > 20$ GeV and rapidity between the two tagging jets, as suggested for the VBF selection, lowers the NLO cross section to $0.97 \times \sigma_{LO}$ for the p_T-method and $0.93 \times \sigma_{LO}$ for the E-method.

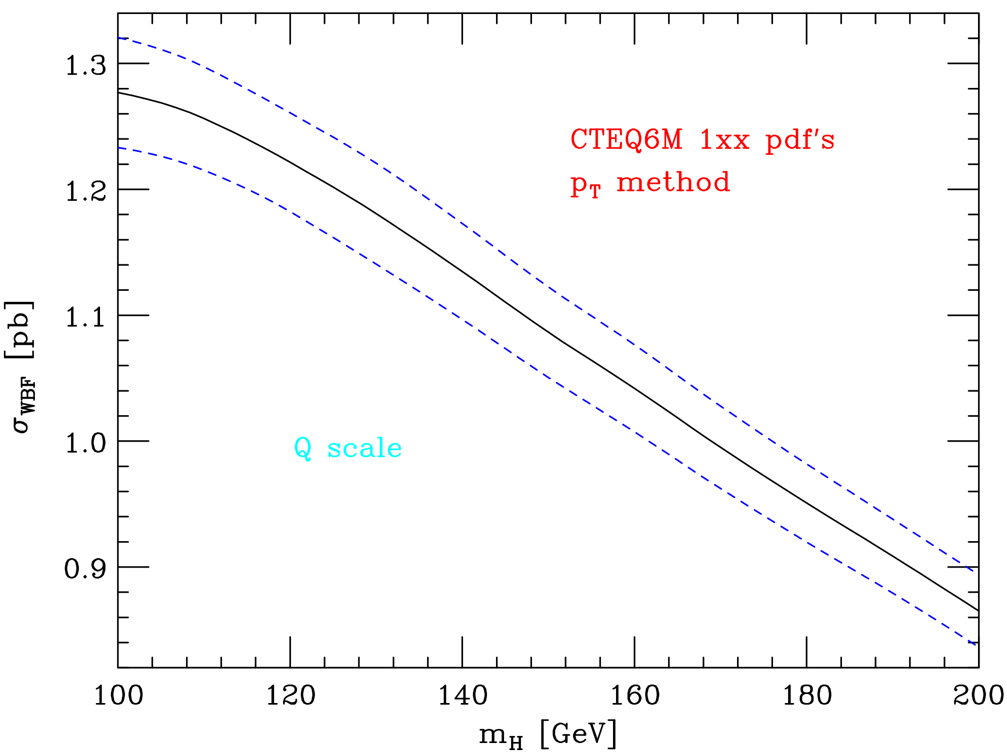

Figure 2.4 Variation of the total cross section, within cuts, due to errors in the parton distribution functions, as a function of m_H. The central solid line corresponds to the “best fit” CTEQ6M pdf, while the upper and lower curves define the pdf error band, which is determined from the 40 error eigenvectors in the CTEQ6M set (CTEQ6M101–CTEQ6M140), adding cross section deviations in quadrature.

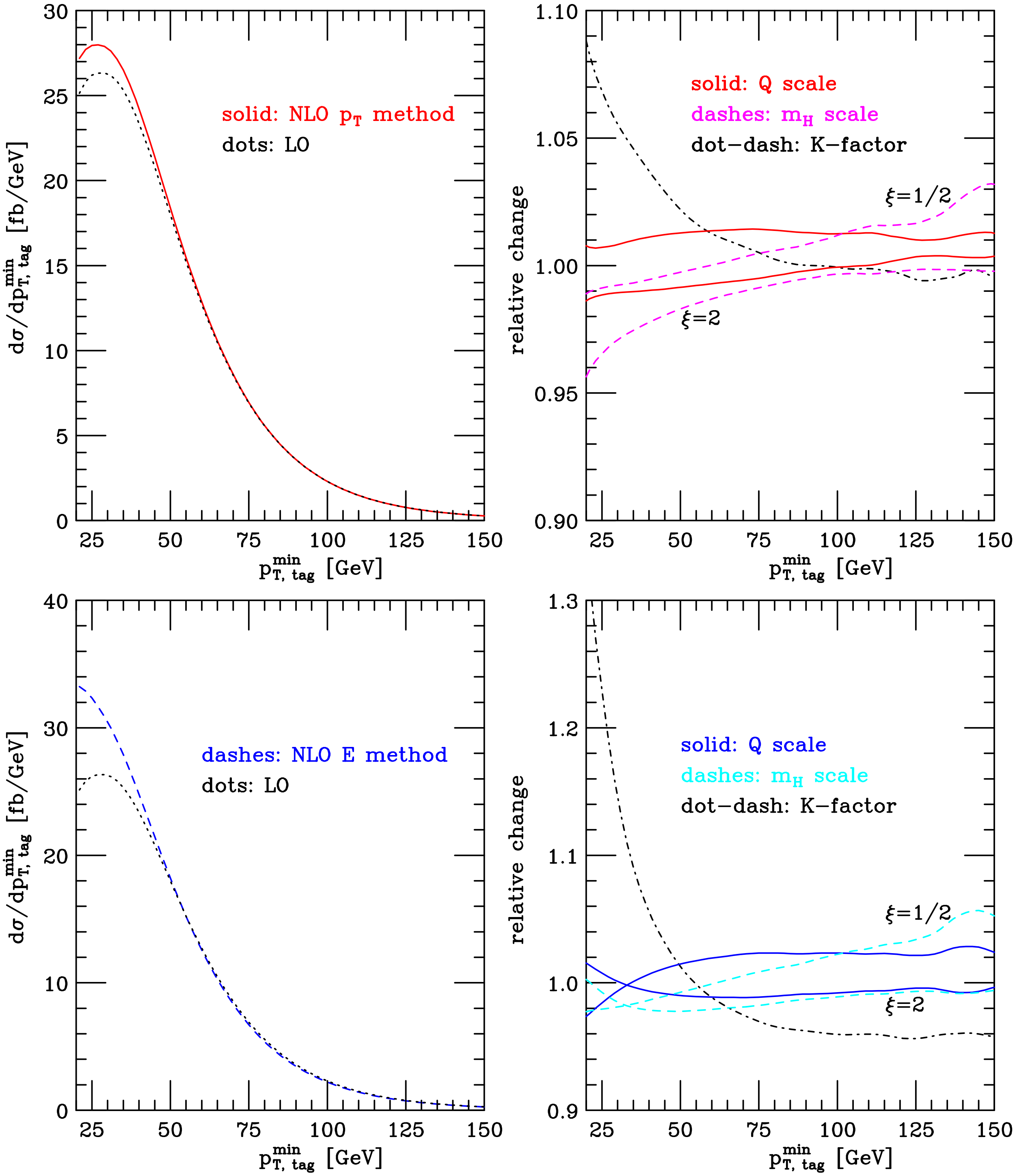

Figure 2.5 Transverse momentum distribution of the softer tagging jet for the the p_T-method (solid red) and the E-method (dashed blue) of defining tagging jets, for $m_H = 120$ GeV. The right-hand panels give the K-factors (black dash-dotted line) and the scale variation of the NLO results. Solid colored curves correspond to $\mu_F = \mu_R = \xi Q_i$ and dashed colored curves are for $\mu_F = \mu_R = \xi m_H$ with $\xi = 1/2$ and 2.

investigated this dependence by calculating the total Higgs boson cross section, within the cuts of Eqs. (2.21)–(2.24), for the 40 pdf's in the CTEQ6Mxxx (xxx = 101–140) set. They correspond to extremal plus/minus variations in the directions of the 20 error eigenvectors of the Hessian of the CTEQ6M fitting parameters [33]. Adding the maximum deviations for each error eigenvector in quadrature, one obtains the blue dashed lines in Fig. 2.4, which define the pdf error band. We find a uniform $\pm 3.5\%$ pdf uncertainty of the total cross section over the entire range of m_H shown.

Scale and pdf uncertainties exhibit little dependence on the Higgs boson mass. We therefore limit our investigation to a single, representative Higgs boson mass for the remaining discussion, which we take as $m_H = 120$ GeV.

While the scale dependence of the integrated Higgs boson production cross section is quite weak, the same need not be true for the shape of distributions which will be used to discriminate between Higgs boson signal and various backgrounds. Having a fully flexible NLO Monte Carlo program at hand, we can investigate this question. Crucial distributions for the detection efficiency of the signal are the transverse momentum and the rapidity of the tagging jets. In Fig. 2.5 the cross section is shown as a function of $p_{T,\mathrm{tag}}^{\min}$, the smaller of the two tagging jet transverse momenta. At LO, the tagging jets are uniquely defined, but at NLO one finds relatively large differences between the p_T-method (solid red curves in the top panels) and the E-method (dashed blue curves in bottom panels). The right-hand-side panels give the corresponding K-factors, as defined in Eq. (2.25), (black dash-dotted lines) and the ratio of NLO differential distributions for different scale choices. Shown are the ratios

$$R = \frac{d\sigma^{NLO}(\mu_F = \mu_R = Q_i)}{d\sigma^{NLO}(\mu_F = \mu_R = \mu)} \qquad [2.28]$$

for $\mu = 2^{\pm 1} Q_i$ (solid lines) and $\mu = 2^{\pm 1} m_H$ (dashed lines). While the K-factor is modest for the p_T-method, it reaches values around 1.3 in the threshold region for the E-method. This strong rise at NLO is due to hard forward gluon jets being misidentified as tagging jets in the E-method. This problem was recognized previously in parton shower Monte Carlo simulations and has prompted a preference for the p_T-method [36]. In spite of the large K-factor, however, the residual scale uncertainty is small, ranging from -4% to +2% for the p_T-method and -2% to +5% for the E-method.

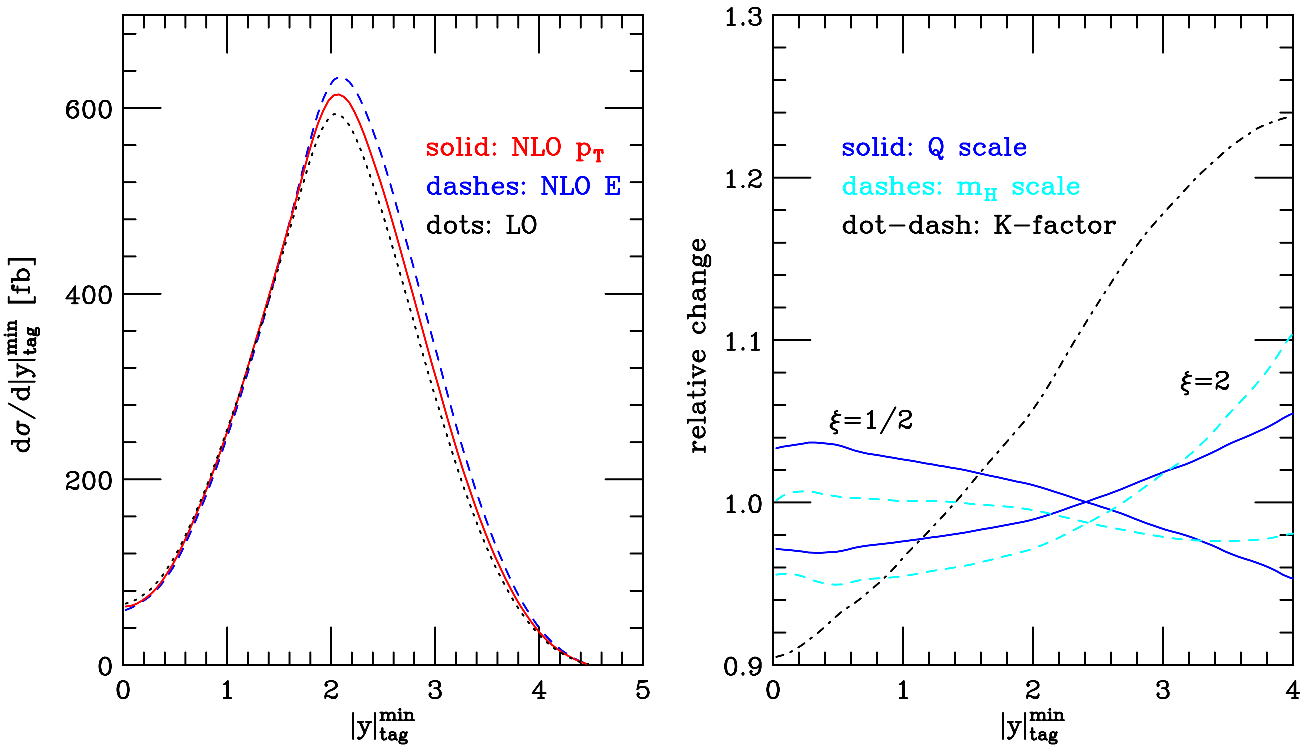

Figure 2.6 Higgs boson production cross section as a function of the smaller of the absolute value of the two tagging jet rapidities, $d\sigma/d|y|^{\rm min}_{\rm tag}$ (in fb, for $m_H = 120$ GeV). Results are shown at LO (dotted black) and at NLO for the p_T-method (solid red) and the E-method (dashed blue) of defining tagging jets. The right-hand panel gives the K-factor (black dash-dotted line) and the scale variation of the NLO result for the E-method. Colored curves for the scale dependence are labeled as in Fig. 2.5.

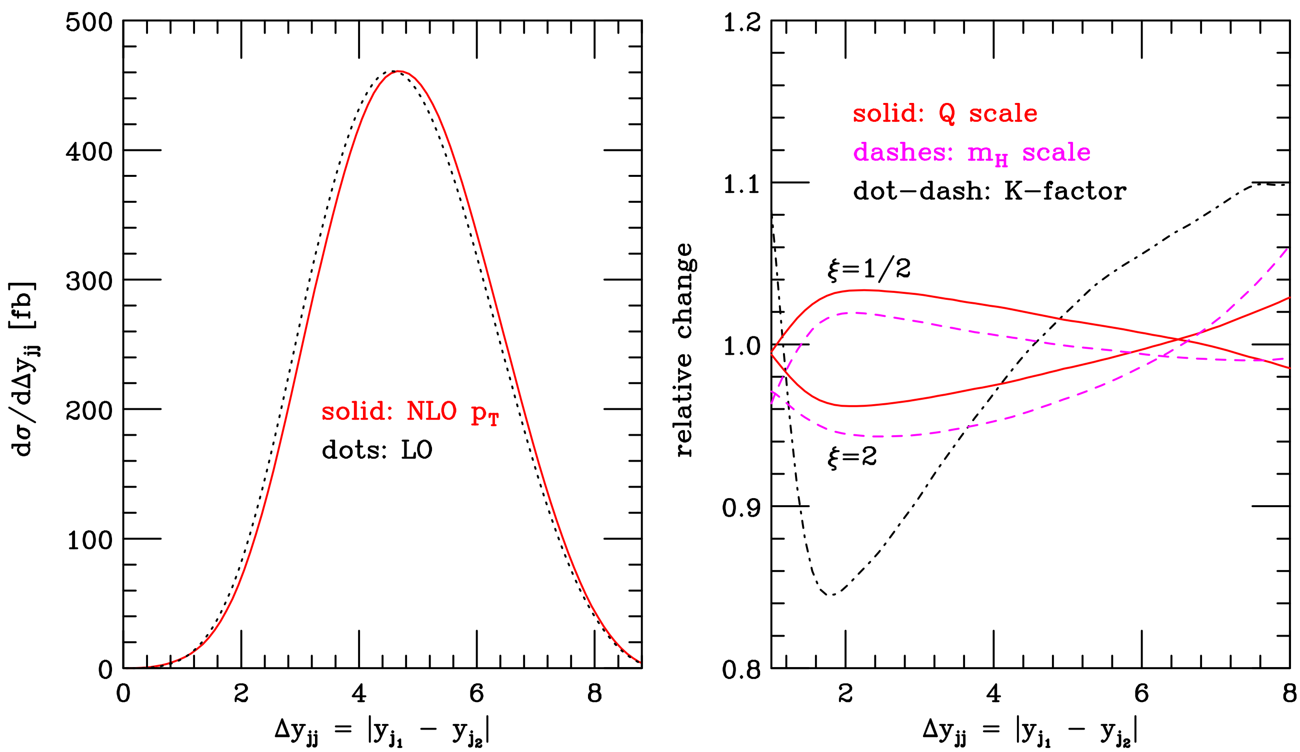

Figure 2.7 Rapidity separation of the two tagging jets for $m_H = 120$ GeV. In the left-hand panel, $d\sigma/d\Delta y_{jj}$ (in fb) is shown at LO (dotted black) and at NLO (solid red), for the p_T-method of defining tagging jets. The right-hand panel gives the corresponding K-factor (black dash-dotted line) and the scale variation of the NLO results. Colored curves for the scale dependence are labeled as in Fig. 2.5.

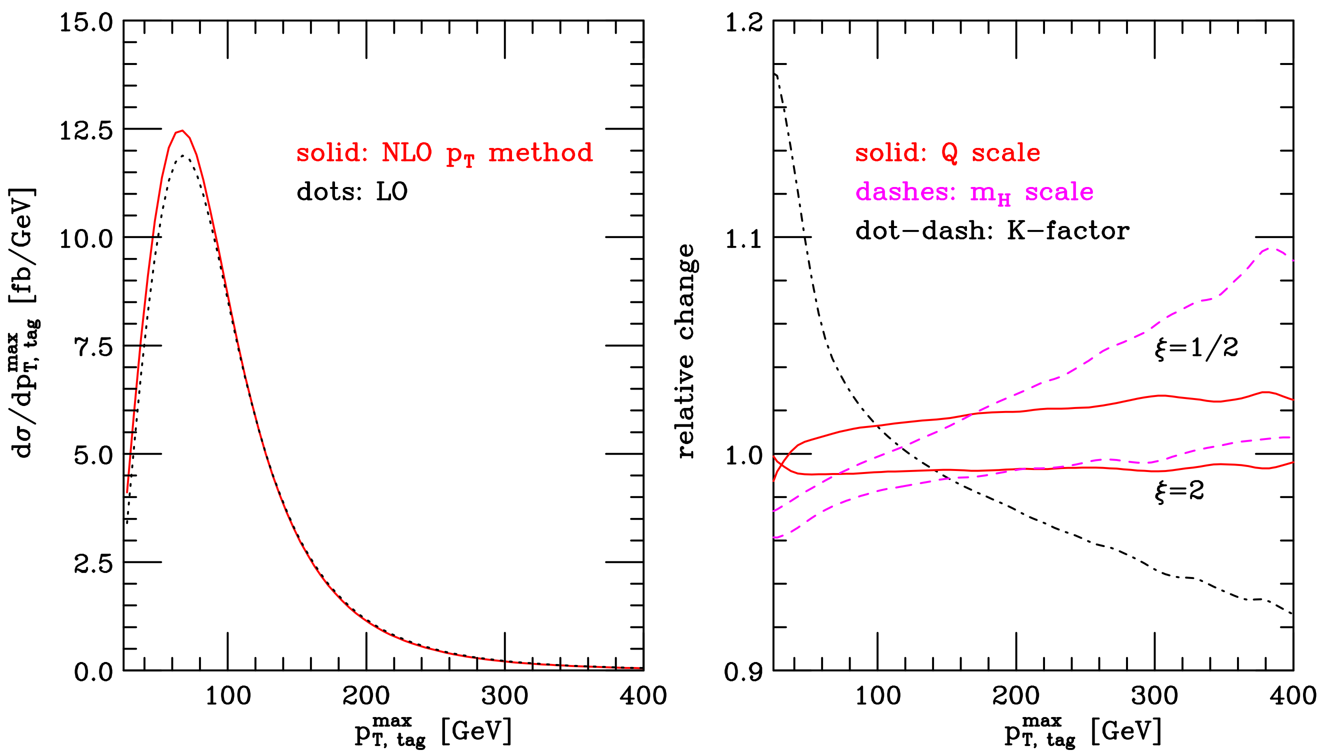

Figure 2.8 Transverse momentum distribution of the harder tagging jet, for $m_H = 120$ GeV. In the left-hand panel, $d\sigma/dp_{T,\text{tag}}^{\text{max}}$ (in fb/GeV) is shown at LO (dotted black) and at NLO (solid red), for the p_T-method of defining tagging jets. The right-hand panel gives the corresponding K-factor (black dash-dotted line) and the scale variation of the NLO results. Colored curves for the scale dependence are labeled as in Fig. 2.5.

The more forward selection of tagging jets in the E-method is most obvious in the rapidity distributions of Figs. 2.6 and 2.7. In Fig. 2.6 the rapidity of the more central of the tagging jets, $|y|_{\rm tag}^{\rm min}$, is shown. At NLO, the tagging jets are slightly more forward than at tree level, leading to a K-factor which varies appreciably over phase space. This $|y|_{\rm tag}^{\rm min}$-dependence is shown in the right-hand panel for the E-method, together with the residual scale dependence at NLO. Again, scale variations of less than $\pm4\%$ are found over virtually the entire phase space. For the p_T-method, similar scale variations arise, as shown in Fig. 2.7 for the rapidity separation between the two tagging jets, where the cuts of Eqs. (2.21)–(2.23) have been imposed. Figure 2.7 demonstrates that the wide separation of the tagging jets, which is important for rejection of QCD backgrounds, does survive at NLO. In fact, the tagging jet separation even increases slightly, making a separation cut like $\Delta y = |y_{j_1} - y_{j_2}| > 4$ even more effective than at LO.

In all distributions considered so far, no clear preference emerges on whether to choose the vector-boson virtuality, Q_i, or m_H as the hard scale. While both choices are acceptable, the transverse momentum distributions show somewhat smaller scale variations for $\mu = \xi Q_i$ than $\mu = \xi m_H$. The effect is most pronounced in the high p_T tail of the tagging jet distributions. When considering $d\sigma/dp_{T,\rm tag}^{\rm max}$, as shown in Fig. 2.8, the scale variation increases to $+10\%$ at large p_T when $\mu = \xi m_H$ is taken, while the same distribution for $\mu = \xi Q_i$ stays in a narrow $\pm2\%$ band. This observation provides another reason for our default scale choice, $\mu = Q_i$.

Unlike the tagging jets considered so far, distributions of the Higgs decay products show little change in shape at NLO.

2.5 Conclusions

Vector-boson fusion processes will play an important role at future hadron colliders, most notably as a probe for electroweak symmetry breaking. For the particular case of Higgs boson production, we have presented a first analysis of the size and of the remaining uncertainties of NLO QCD corrections to jet distributions in VBF.

As for the inclusive VBF cross section, QCD corrections to distributions are of modest size, of order 10%, but occasionally they reach larger values. These corrections are strongly phase-space dependent for jet observables and an overall K-factor multiplying the LO distributions is not an adequate approximation. Within the phase-space region relevant for Higgs boson searches, we find differential K-factors as small as 0.9 or as large as 1.3. These corrections need to be taken into account for Higgs coupling measurements, and our NLO Monte Carlo program, or the recently released analogous program in the MCFM package [11, 37], provide the necessary tools.

After inclusion of the one-loop QCD corrections, remaining uncertainties due to as yet uncalculated higher order terms, can be estimated by considering scale variations of the NLO cross section. Using the Higgs boson mass, m_H, and the vector-boson virtuality, Q_i, as potential hard scales, we find that these remaining scale dependencies are quite small. Varying renormalization or factorization scales by a factor of two away from these two central values results in typical changes of the NLO differential cross sections by ±2% or less. The uncertainty bands for $\mu = \xi m_H$ and $\mu = \xi Q_i$ typically overlap, yielding combined scale uncertainties of less than ±3% in most cases, occasionally rising up to order 5% at the edges of phase space. Moreover, the variation in different regions typically cancels in the integrated Higgs cross section, within cuts, leading to uncertainties due to higher order effects of ±2% (see Fig. 2.3), even when considering different hard scales. The remaining theoretical uncertainty on the measurable Higgs cross section, thus, is well below expected statistical errors, except for the $H \to WW$ search for Higgs masses around 170 GeV, where the high LHC rate allows statistical errors as low as 3%. In addition, pdf uncertainties for the total cross section are of order $\pm 3.5\%$ over the range 100 GeV $\leq m_H \leq$ 200 GeV. This means that the SM Higgs boson production cross section via VBF can be predicted, at present, with a theoretical error of about $\pm 4\%$.

The expected size of the LHC Higgs signal is enhanced slightly by the NLO QCD corrections. In addition to a K-factor slightly above unity due to a small shift of the tagging jets to higher rapidities, still well inside the detector coverage, tagging jets are moved slightly farther apart. This allows for better differentiation of the Higgs signal from QCD backgrounds.

The techniques described here work in a very similar fashion for other vector-boson fusion processes such as W^+W^-jj production [38], $ZZjj$ production [39], and production Vjj ($V = Z, W$) [40].

Chapter 3

QCD Corrections to Jet Correlations in Vector Boson Fusion

3.1 Introduction

The production of Higgs bosons in the vector boson fusion (VBF) process will provide a direct and highly sensitive probe of HWW and HZZ couplings at the CERN Large Hadron Collider (LHC) [17, 24, 25, 26, 27, 28, 41]. The determination both of the strength and of the tensor structure of these couplings is crucial for the identification of the produced boson as a remnant of the spontaneous symmetry breaking process which is responsible for W and Z mass generation.

Within spontaneously broken, renormalizable gauge theories like the standard model (SM), this coupling originates from the kinetic energy term, $(D_\mu\Phi)^\dagger(D^\mu\Phi)$, of a scalar Higgs field, Φ, whose neutral component obtains a vacuum expectation value (vev), $\Phi^0 \to (v+H)/\sqrt{2}$. This replacement then leads to a characteristic coupling in the interaction Lagrangian, of the form $HV_\mu V^\mu$ ($V = W, Z$). The existence of the vev is necessary to produce a trilinear HVV coupling at tree level: with $v = 0$ all couplings to the gauge fields V contain two scalar fields, i.e., only HHV and $HHVV$ couplings would be generated. A trilinear HVV coupling may also be loop-induced, however. The SM $H\gamma\gamma$ and Hgg effective couplings are an example: they are induced by W-boson and/or top quark loops. Gauge invariance dictates a different tensor structure of these loop-induced couplings: the corresponding effective Lagrangian contains the square of the field strength, i.e. the lowest order loop-induced terms are of the form $HV_{\mu\nu}V^{\mu\nu}$ or $HV_{\mu\nu}\tilde{V}^{\mu\nu}$, where $\tilde{V}^{\mu\nu} = \frac{1}{2}\epsilon^{\mu\nu\rho\sigma}V_{\rho\sigma}$ denotes the dual field strength of the gauge field.

The task of future Higgs experiments is, then, twofold: (i) to measure the overall strength of the HVV coupling, and (ii) to identify its tensor structure. One would expect a loop-induced coupling to be much smaller than the expected SM HVV coupling strength. However, the measurement of VBF rates alone will not be sufficient to establish H as being related to spontaneous symmetry breaking: to give just two examples, the loop-induced couplings might be substantially enhanced by additional non-SM particles in the loop or by the existence of multiplets of large weak isospin which couple strongly to H. Or a particular LHC signature may be strongly enhanced by a much larger H decay branching ratio than in the SM. A confirmation that the HVV coupling has tree level strength is, thus, ambiguous: a clear identification of the Higgs boson also requires the identification of the tensor structure of the HVV vertex.

It was pointed out some time ago that the azimuthal angle correlations of the two quark jets in the weak boson fusion process $qQ \to qQH$ provide tell-tale signatures for the tensor structure of the HVV couplings [42]: the SM expectation is for a flat distribution, while the loop-induced couplings lead to a pronounced dip at azimuthal separations ϕ_{jj} of the two tagging jets of 90 degrees for a $HV_{\mu\nu}V^{\mu\nu}$ coupling and at 0 and 180 degrees for the CP violating $HV_{\mu\nu}\tilde{V}^{\mu\nu}$ vertex. Observation of the tagging jets is crucial for isolating the VBF process from backgrounds and, therefore, their distributions will be available for all VBF samples. Also, signal to background ratios for VBF processes are expected to be very good within the SM, exceeding the 1:1 level for wide ranges of the Higgs boson mass [24, 25, 26, 28, 41].

The analysis of Ref. [42] was performed at leading order (LO) in QCD. This means that additional gluon emission, which might lead to a de-correlation of the tagging jets, was ignored in the analysis. Subsequently it was argued [43] that such de-correlation effects play an important role in a related process, $gg \to Hgg$, when the two tagging jets are widely separated in rapidity, which is a typical requirement for VBF studies. In this Chapter we analyze this question, by calculating the tagging jet distributions in next-to-leading order (NLO) QCD, for the production of a scalar H via VBF with an arbitrary tensor structure of the HVV vertex. If de-correlation is important, it should show up in the form of large radiative corrections at NLO. We use the term "Higgs boson" as a generic name for the produced scalar in the following.

3.2 The NLO calculation

The current calculation is an extension of the NLO QCD corrections for the SM VBF processes $qQ \to qQH$ (and crossing related ones) [10, 11, 12]. For the total cross section these corrections have been known for over a decade [12]. Recently, the QCD corrected cross section has been recalculated by developing a NLO parton level Monte Carlo program [10] which provides the flexibility to calculate arbitrary distributions at NLO, such as the azimuthal angle correlations that are of interest here (See Chapter 2).

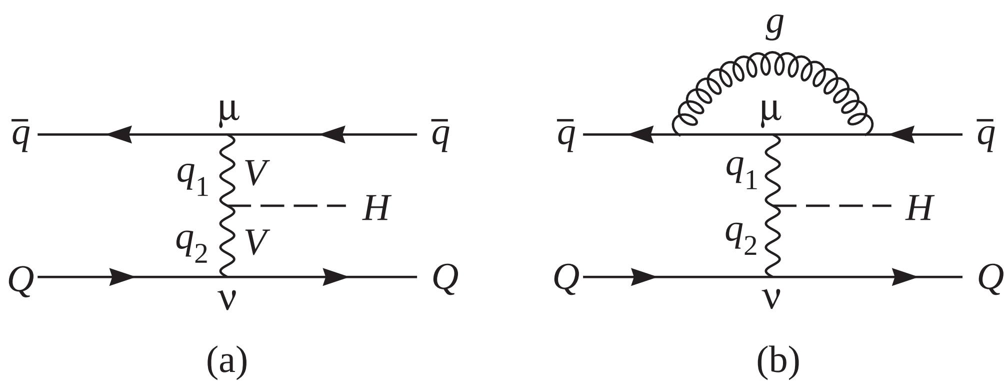

Figure 3.1 Feynman graphs contributing to $\bar{q}Q\to\bar{q}QH$ at (a) tree level and (b) including virtual corrections to the upper quark line. The momentum labels and Lorentz indices for the internal weak bosons correspond to the vertex function of Eq. (3.1).

The calculation of Ref. [10] uses a SM vertex function, $T^{\mu\nu}(q_1,q_2)=\frac{2m_V^2}{v}g^{\mu\nu}$ for the HVV vertex in Fig. 3.1. Here the vertex is generalized to the most general structure compatible with Lorentz invariance. Taking into account that the quark currents in Fig. 3.1 and for the corresponding gluon emission processes are conserved, all terms proportional to q_1^μ or q_2^ν may be dropped, and the most general HVV vertex may be written as

$$T^{\mu\nu}(q_1,q_2)=a_1(q_1,q_2)\;g^{\mu\nu}+a_2(q_1,q_2)\;[q_1\cdot q_2 g^{\mu\nu}-q_2^\mu q_1^\nu]+a_3(q_1,q_2)\;\varepsilon^{\mu\nu\rho\sigma}q_{1\rho}q_{2\sigma}\;. \qquad [3.1]$$

Here q_1 and q_2 are the four-momenta of the two weak bosons, and the $a_i(q_1,q_2)$ are Lorentz-invariant form factors, which might, for example, represent scalar loop integrals in a perturbative calculation. It is straightforward to implement the general vertex of Eq. (3.1) into the NLO QCD Monte Carlo: the virtual amplitude of Fig. 3.1 is proportional to the Born amplitude, $\mathcal{M}_{\rm Born}$, irrespective of the structure of the HVV vertex. Thus, all amplitudes reduce to a simple contraction of quark (or quark-gluon) currents with the vertex function of Eq. (3.1). These currents, and their contractions, are evaluated numerically, using the amplitude formalism of Ref. [30]. All other aspects of the present NLO calculation are handled as in Ref. [10], except that Higgs boson decays are not simulated in the following. Factorization and renormalization scales are fixed to $\mu_F=\mu_R=Q_i$ for QCD corrections to the first or second quark line in Fig. 3.1. Here Q_1 and Q_2 are the virtualities of the exchanged weak bosons. We use CTEQ6M parton distributions [33] with

$\alpha_s(M_Z) = 0.118$ for all NLO results and CTEQ6L1 parton distributions for all leading order cross sections.

3.3 Anomalous couplings and form factors

While the $g^{\mu\nu}$-term in the vertex function (3.1) corresponds to a SM Higgs coupling, the anomalous coupling terms a_2 and a_3 can be related to higher dimensional operators in an effective Lagrangian. They first appear at the dimension-5 level [1] and may be written as

$$\begin{aligned} \mathcal{L}_5 &= \frac{g_{5e}^{HWW}}{\Lambda_{5e}} H W^+_{\mu\nu} W^{-\mu\nu} + \frac{g_{5o}^{HWW}}{\Lambda_{5o}} H \tilde{W}^+_{\mu\nu} W^{-\mu\nu} + \\ & \frac{g_{5e}^{HZZ}}{2\Lambda_{5e}} H Z_{\mu\nu} Z^{\mu\nu} + \frac{g_{5o}^{HZZ}}{2\Lambda_{5o}} H \tilde{Z}_{\mu\nu} Z^{\mu\nu} \;, \end{aligned} \qquad [3.2]$$

where the subscript e or o refers to the CP even or odd nature of the individual operators. In the discussion possible contributions from $H\gamma\gamma$ and $H\gamma Z$ couplings which can appear in $SU(2) \times U(1)$ invariant formulations [44, 45] will be neglected. The precise mix of HWW, HZZ, $HZ\gamma$ and $H\gamma\gamma$ contributions is quite irrelevant for the observable azimuthal angle distributions, as long as we do not consider interference effects between SM and anomalous vertices, and it will not affect our conclusions about the size of NLO corrections. For simplicity we therefore set $a_1 = 0$ for the anomalous coupling case and choose relative contributions from WW and ZZ fusion as in the SM, by taking $g_{5o}^{HWW} = g_{5e}^{HWW} = 1$, $g_{5e}^{HZZ} = g_{5o}^{HZZ} = 1/\cos^2\theta_W$, and by using either $\Lambda_{5e} \simeq$480 GeV, $\Lambda_{5o} = \infty$ for the CP even case or $\Lambda_{5o} \simeq$480 GeV, $\Lambda_{5e} = \infty$ for the CP odd case, which roughly reproduces SM rates for a scalar mass of $m_H = 120$ GeV.

The effective Lagrangian of Eq. (3.2) produces couplings

$$a_2(q_1, q_2) = -\frac{2}{\Lambda_{5e}} g_{5e}^{HWW} \;, \qquad a_3(q_1, q_2) = \frac{2}{\Lambda_{5o}} g_{5o}^{HWW} \qquad [3.3]$$

for the HWW vertex, and

$$a_2(q_1, q_2) = -\frac{2}{\Lambda_{5e}} g_{5e}^{HZZ} \;, \qquad a_3(q_1, q_2) = \frac{2}{\Lambda_{5o}} g_{5o}^{HZZ} \qquad [3.4]$$

[1] The dimension 5 language is appropriate for, e.g., an isosinglet scalar resonance H. For a Higgs doublet Φ with a vev, the leading operators appear at dimension 6 level [44, 45] and the couplings in Eq. (3.2) are suppressed by an additional factor $g_5^{HVV} \sim v/\Lambda$.

for the HZZ vertex. In general, the a_i are form factors which are expected to be suppressed once the momentum transfer, $\sqrt{-q_i^2}$, carried by the virtual gauge boson reaches the typical mass scale, M, of the new physics which is responsible for these anomalous couplings. Below we use the simple ansatz

$$a_i(q_1, q_2) = a_i(0,0)\,\frac{M^2}{q_1^2 - M^2}\,\frac{M^2}{q_2^2 - M^2} \qquad [3.5]$$

for discussing the consequences of such form factor effects.

3.4 Results

The typical signature of a weak boson fusion event at the LHC consists of the two quark jets (tagging jets) and the Higgs decay products. The tagging jets tend to be widely separated in rapidity, with one quite forward (typical pseudorapidity of 3 to 4) and the second one backward, but frequently still located in the central detector (pseudorapidity below 2.5). Various Higgs decay modes have been considered in the literature for VBF, $H\to WW$ [26], $H\to\tau\tau$ [25], and $H\to\gamma\gamma$ [28] being the most promising ones. While optimized event selection varies, in particular for the decay products, the cuts on the tagging jets are fairly similar in all analyses. Since the QCD features are of main interest here, the NLO anlaysis is performed without simulating Higgs decays, and typical VBF cuts on the tagging jets are imposed.

In order to reconstruct jets from the final-state partons, the k_T-algorithm [34] as described in Ref. [35] is used, with resolution parameter $D = 0.8$. In a given event, the tagging jets are then defined as the two jets with the highest transverse momentum, p_{Tj}, with

$$p_{Tj} \geq 20 \text{ GeV}\,, \qquad\qquad |y_j| \leq 4.5\,. \qquad [3.6]$$

Here y_j denotes the rapidity of the (massive) jet momentum which is reconstructed as the four-vector sum of massless partons of pseudorapidity $|\eta| < 5$. Backgrounds to weak-boson fusion are significantly suppressed by requiring a large rapidity separation of the two tagging jets. This motivates the final cut

$$\Delta y_{jj} = |y_{j_1} - y_{j_2}| > 4\,, \qquad y_{j_1}\cdot y_{j_2} < 0\,, \qquad [3.7]$$

which includes the requirement that the two tagging jets reside in opposite detector hemispheres.

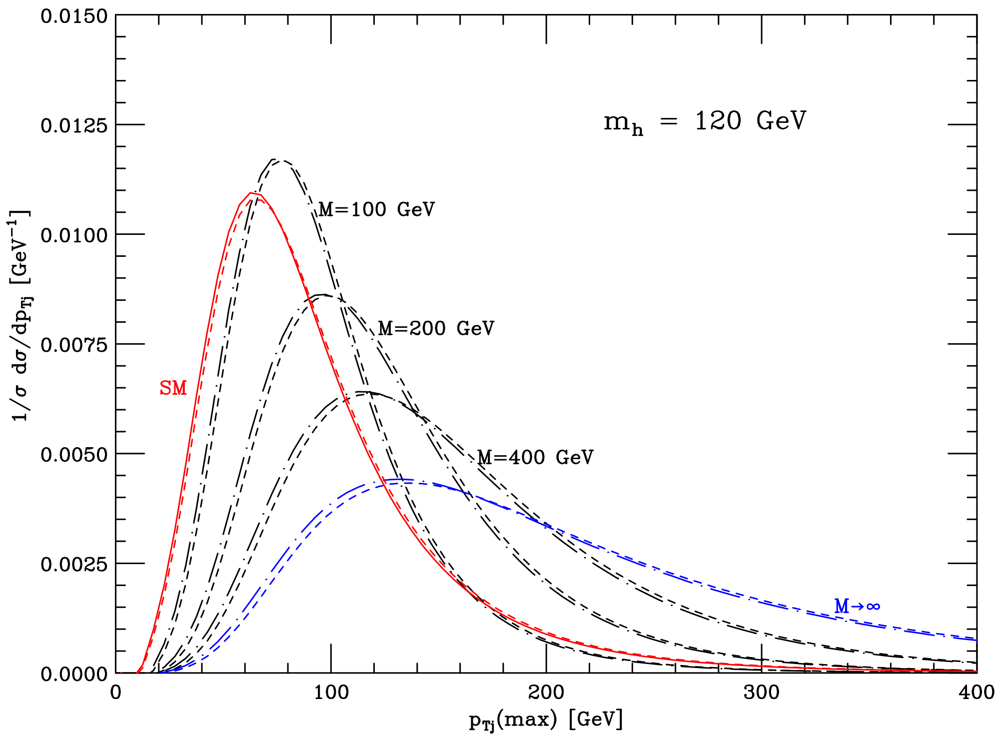

Figure 3.2 Normalized transverse momentum distribution of the hardest jet for the SM Higgs boson (solid red line) and a scalar H of mass $m_H = 120$ GeV with CP even anomalous coupling $a_2(q_1, q_2)$. The dash-dotted curves correspond to different form factor scales $M = 100$, 200, 400 GeV in Eq. (3.5) and $a_2 = const.$ (blue curves) at NLO. LO curves are shown by the dashed lines and differ very little from the NLO results.

The structure of the HVV coupling affects the production dynamics of H and we can expect significant deviations in jet observables if, instead of the SM, anomalous couplings describe the vertex of Eq. (3.1). One example is shown in Fig. 3.2, where transverse momentum distributions, $d\sigma/dp_{Tj}(\max)$, are compared between the SM (solid line) and the CP even coupling $a_2(q_1, q_2)$, with different form factor scales M in Eq. (3.5). Here, $p_{Tj}(\max)$ is the maximum p_T of the two tagging jets. Only the shape of the distribution is considered, since the rate can always be adjusted by multiplying the anomalous couplings by a constant factor. Also, one should note that a CP odd coupling leads to very similar curves for a given form factor scale. In all of the cases shown the LO expectations (dashed lines) together with the NLO results: QCD corrections are of order 10%, typically, and well under control.

One finds that anomalous HVV couplings generally lead to harder p_T spectra of the two tagging jets. Since the anomalous Lagrangian in Eq. (3.2) couples the Higgs boson to weak boson field strengths, transverse polarizations of the incident VV pairs dominate the anomalous case, while longitudinal VV fusion is responsible for SM Higgs production. A telltale sign of transverse vector boson fusion is the more central and, hence, higher p_T production of the tagging jets. This effect is enhanced by the momentum factors in the HVV anomalous vertices.

While the changed transverse momentum distributions in Fig. 3.2 could be used to rule out the SM, the reverse is not readily possible: a jet transverse momentum distribution compatible with SM expectations might be faked by anomalous couplings and a judiciously chosen form factor behavior of the coefficient functions a_2 or a_3 in Eq. (3.5). The different scale choices in Fig. 3.2 demonstrate this effect: a low form factor scale of $M = 100$ GeV or slightly lower would be difficult to distinguish from the SM expectation and one can certainly find a functional form of the form factors which reproduces the SM within experimental errors.

A much better observable for distinguishing the different tensor structures of the HVV vertex is the azimuthal angle correlation of the two tagging jets, $d\sigma/d\phi_{jj}$ [42]. Here ϕ_{jj} is the azimuthal angle between the two tagging jets. The corresponding distributions are shown in Fig. 3.3 for the SM (solid line) and for the same choices of form factors as before. The dip at $\phi_{jj} = 90$ degrees for the CP even coupling and the suppression at 0 and 180 degrees for the CP odd coupling are

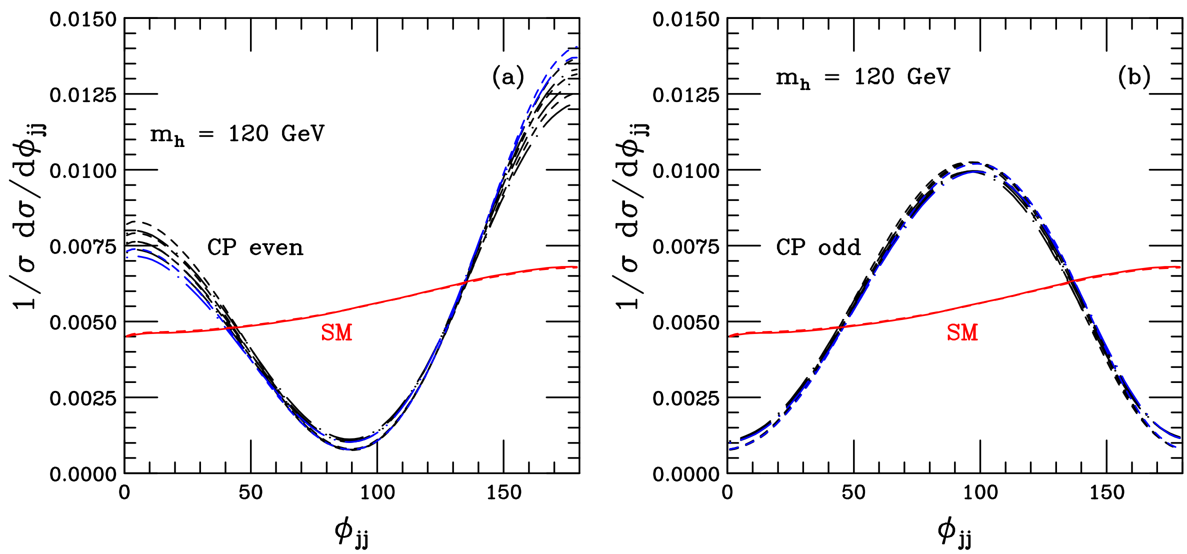

Figure 3.3 Normalized azimuthal angle distribution, $1/\sigma\ d\sigma/d\phi_{jj}$ where ϕ_{jj} is the azimuthal angle separation of the two tagging jets. NLO (solid and dot-dashed) and LO results (dashed lines) are shown for $m_H = 120$ GeV in the SM (red curves) and (a) for a CP even anomalous coupling $a_2(q_1, q_2)$, (b) for a CP odd anomalous coupling $a_3(q_1, q_2)$ with form factor scales $M = 100$, 200, 400 GeV and (blue curves) $M = \infty$.

clean signatures which only depend on the tensor structure of the couplings and not on the precise dynamics which is responsible for the form factors. The remaining form factor dependence is very small and can be explained by kinematic effects related to the higher average jet transverse momentum for big form factor scales, M: at small ϕ_{jj} two high p_T jets recoil against the H scalar, resulting in an increased invariant mass of the event compared to the situation with two back-to-back jets. This leads to a more asymmetric ϕ_{jj} distribution for high form factor scales.

The pronounced dip at 90 degrees, which is characteristic of the CP even coupling, is also found in Hjj production via gluon fusion [46], at LO. This is not surprising because, in the large top mass limit, the Hgg vertex can be described by an effective Lagrangian proportional to $HG^a_{\mu\nu}G^{a\mu\nu}$, which exhibits the same field strength squared behavior and hence the same tensor structure as the CP even HVV coupling in Eqs. (3.1,3.2). Since the two tagging jets are far apart from each other, separated by a large rapidity gap of 4 units of rapidity or more, this LO behavior may be significantly reduced by gluon radiation when higher order QCD corrections are taken into account. Such de-correlation effects have been studied for dijet events at the Tevatron [47]. For Hjj production via gluon fusion, Odagiri [43] has argued that the dip structure is largely washed out by additional gluon emission between the two tagging jets.

NLO calculations show that such de-correlation effects are irrelevant for weak boson fusion, where t-channel color singlet exchange severely suppresses gluon radiation in the central region. The LO and the NLO curves in Fig. 3.3 are virtually indistinguishable. In order to better exhibit the size of the NLO QCD effects for the VBF case the azimuthal angle correlations for a pure CP even anomalous coupling for three different Higgs masses, $m_H = 120$, 200 and 500 GeV is shown in Fig. 3.4(a). Only small changes are visible when going from LO (dashed lines) to NLO (solid lines). The differences between LO and NLO are smaller than kinematical effects that can be induced by cuts on the Higgs decay products or by variations of the Higgs boson mass.

The small to modest size of the QCD corrections is quantified in Fig. 3.4(b) where the K factor for the distribution is shown, which is defined as

$$K(\phi_{jj}) = \frac{d\sigma^{NLO}/d\phi_{jj}}{d\sigma^{LO}/d\phi_{jj}} \; . \qquad [3.8]$$

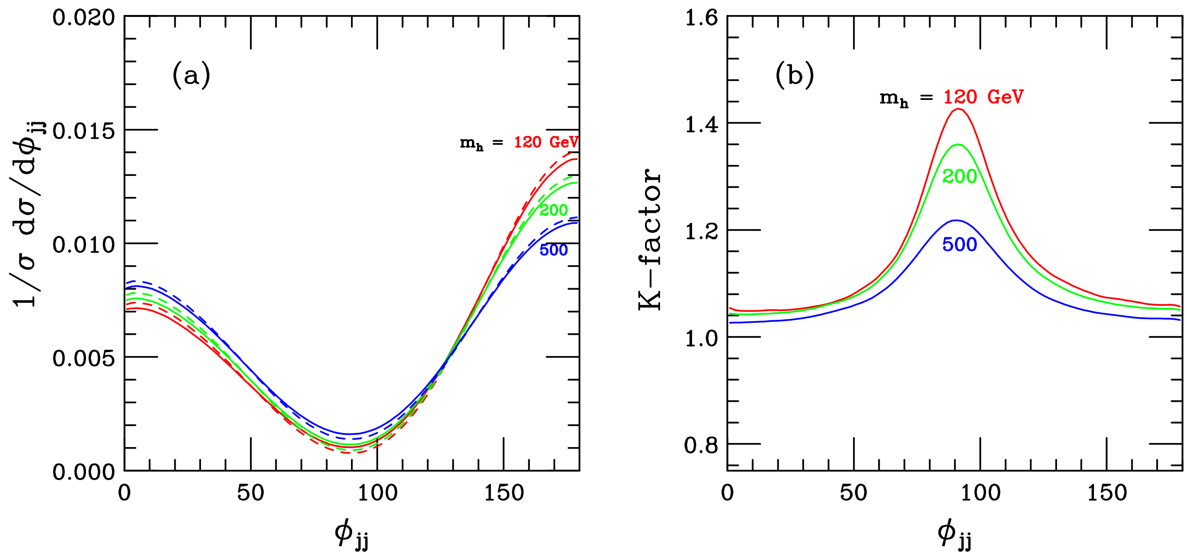

Figure 3.4 Higgs mass dependence of the azimuthal angle separation ϕ_{jj} of the two tagging jets. In (a) the normalized azimuthal angle distributions are shown at LO (dashed lines) and NLO (solid lines) for Higgs masses of $m_H = 120$, 200, 500 GeV and a constant CP even anomalous coupling a_2. Corresponding K-factors are shown in (b).

The K-factor is below ≈ 1.4 even in the dip region, where the cross section is severely suppressed. Virtually identical results hold for the CP-odd case. Clearly, the characteristic azimuthal angle distributions of the jets in VBF are not affected in any significant way by NLO QCD corrections.

3.5 Conclusions

The first calculation of the NLO QCD corrections to Higgs boson production via VBF in the presence of arbitrary anomalous HVV ($V = W, Z$) couplings has been performed. Anomalous couplings lead to characteristic changes in the azimuthal angle correlation of the two tagging jets in weak boson fusion events at the LHC, which provides for a very sensitive test of the tensor structure of the HVV couplings of the Higgs boson or of any other scalar with sufficiently large production cross section in VBF [42]. By explicit calculation, it has been shown that these azimuthal correlations are not washed out by gluon emission, at NLO QCD, even though the tagging jets are widely separated in rapidity. This behavior can be understood as a consequence of t-channel color singlet exchange in VBF which severely suppresses the central gluon radiation which might cause tagging jet de-correlation.

Chapter 4

Next-to-Leading Order QCD Corrections for Higgs Production via Vector-Boson Fusion in the Association of Three Jets

4.1 Introduction

In this chapter the next-to-leading order (NLO) QCD corrections for Higgs production via vector boson fusion in the association of three jets (VBF $Hjjj$) are computed. In Section 4.2 the leading order (LO) cross section is discussed. In Section 4.3 the *Catani-Seymour* dipole subtraction method [21] is used to regulate soft and collinear singularities of the real emission corrections. Formulae for the virtual corrections are given in Subsection 4.3.2. The cancellation of infrared divergences of the virtual corrections is presented in Subsection 4.3.3. Formulae for finite collinear contributions to the cross section that arise from renormalization of the parton distribution functions are given explicitly in Subsection 4.3.4.

4.2 The Leading Order Cross Section

The leading order (LO) cross section for the process $pp \to Hjjj$ can be computed from the real emission graphs of the NLO QCD corrections to Higgs production via vector boson fusion in the association of two jets which was presented in Chapter 2 [10]. More precisely, the calculation is exact for non-identical quark flavors on the upper and lower quark lines. For processes $q\bar{q} \to q\bar{q}gH$ annihilation graphs like $q\bar{q} \to Z^\star \to ZH$ with subsequent decay $Z \to q\bar{q}$ or WH production channels also contribute. For $qq \to qqgH$ or $\bar{q}\bar{q} \to \bar{q}\bar{q}gH$ the interchange of two particle in the initial or final state needs to be considered. However, in phase space regions in which VBF can be observed experimentally, with widely separated quark jets of very large invariant mass, the interference of these additional graphs is strongly suppressed by the large momentum transfer in the weak-boson propagators. Additionally, color suppression further makes these effect negligible. For these reasons, identical particle effects will be systematically neglected. The matrix elements for the Born-level graphs are computed numerically using the helicity-amplitude formalism of Ref.[30] and the computer code developed in Ref.[10] is readily available for use in the current calculation.

The Born Feynman graphs depicted in Figure 4.1 consist of two color structures. The index 21 refers to gluon emission off the 21 quark-line and the index 43 refers to gluon emission off the 43

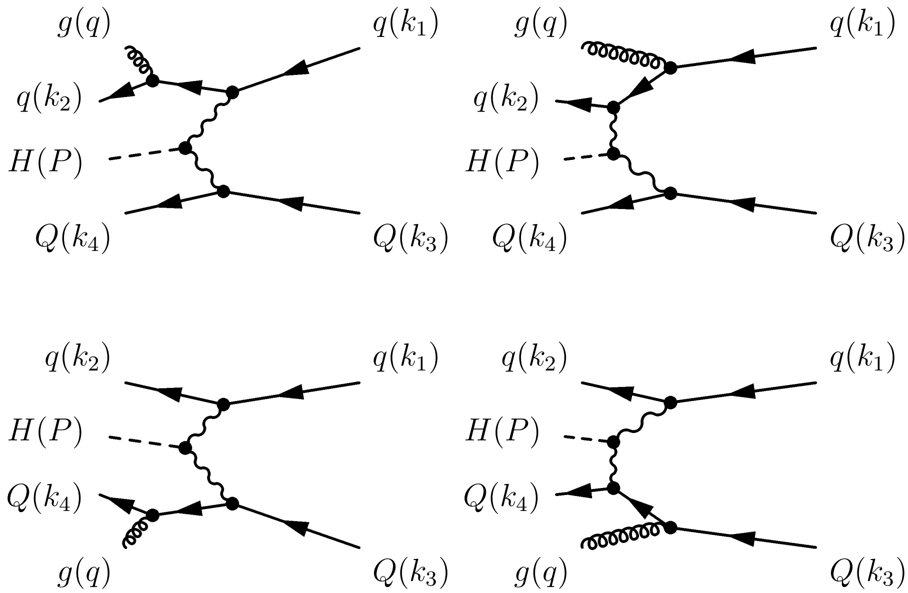

Figure 4.1 Feynman graphs for the LO process $q(k_1) + Q(k_3) \to q(k_2) + Q(k_4) + H(P)$.

quark-line. The Born amplitude can be decomposed into two color structures

$$\mathcal{M}_B(k_1 i_1, k_2 i_2, k_3 i_3, k_4 i_4, qa) = t^a_{i_2 i_1} \delta_{i_4 i_3} \mathcal{M}_{B,21} + t^a_{i_4 i_3} \delta_{i_2 i_1} \mathcal{M}_{B,43} \tag{4.1}$$

with

$$\mathcal{M}_{B,21} = \mathcal{M}_{B,21}(k_2, q, k_1; k_4, k_3) \tag{4.2}$$

and

$$\mathcal{M}_{B,43} = \mathcal{M}_{43}(k_4, q, k_3; k_2, k_1) \tag{4.3}$$

for the generic process

$$q(k_1) + Q(k_3) \to q(k_2) + Q(k_4) + g(q) + H(P). \tag{4.4}$$

The indices i_1, i_2, i_3, and i_4 are color indices for the external (anti-) quarks that carry four momenta k_1, k_2, k_3, and k_4, respectively. The index a is the color index for the gluon. The notation being used here will be referred to as diagrammatic notation. Below the color sub-amplitudes $\mathcal{M}_{B,21} = \mathcal{M}^{\mu}_{B,21}\epsilon_\mu$ and $\mathcal{M}_{B,43} = \mathcal{M}^{\mu}_{B,43}\epsilon_\mu$ are given explicitly. Here the space-time index μ is the spin-index of the external gluon. For gluon emission off the 21 quark line, the color sub-amplitude is

$$\begin{aligned}\mathcal{M}^{\mu}_{B,21} &= e^2 g^{Vf_2f_1}_{\tau_1} g^{Vf_4f_3}_{\tau_3} g_{HVV} g_s \bar{\psi}(k_2)[\gamma^\nu P_{\tau_1} \frac{(\not{k}_2 + \not{q}_1)}{(k_2+q_1)^2}\gamma^\mu \\ &+ \gamma^\mu \frac{(\not{k}_2 + \not{q})}{(k_2+q)^2}\gamma^\nu P_{\tau_1}]\psi(k_1)\bar{\psi}(k_4)\gamma_\nu P_{\tau_3}\psi(k_3) D_V(q_1^2) D_V(q_2^2)\end{aligned} \quad [4.5]$$

where $q_1 = k_1 - q - k_2$ and $q_2 = k_3 - k_4$. Here $D_V(q^2) = \frac{1}{q^2 - m_V^2 + i0_+}$ is the vector boson propagator and $P_\tau = \frac{1}{2}(1 + \tau\gamma_5)$ is the chirality projector. For gluon emission off the 43 quark line, the color sub-amplitude is

$$\begin{aligned}\mathcal{M}^{\mu}_{B,43} &= e^2 g^{Vf_2f_1}_{\tau_1} g^{Vf_4f_3}_{\tau_3} g_{HVV} g_s \bar{\psi}(k_4)[\gamma^\nu P_{\tau_3} \frac{(\not{k}_4 + \not{q}_2)}{(k_4+q_2)^2}\gamma^\mu \\ &+ \gamma^\mu \frac{(\not{k}_4 + \not{q})}{(k_4+q)^2}\gamma^\nu P_{\tau_3}]\psi(k_3)\bar{\psi}(k_2)\gamma_\nu P_{\tau_1}\psi(k_1) D_V(q_1^2) D_V(q_2^2)\end{aligned} \quad [4.6]$$

where $q_1 = k_1 - k_2$ and $q_2 = k_3 - q - k_4$. In both color sub-amplitudes, $\epsilon = \epsilon(q)$ is the gluon polarization. The square of the amplitude averaged over color is

$$|\mathcal{M}_B|^2 = C_F(|\mathcal{M}_{B,21}|^2 + |\mathcal{M}_{B,43}|^2) \quad [4.7]$$

for the case that there are two initial state quarks. For the case of an initial state gluon, one would either drop the first or second term in the above equation since only VBF processes are considered. Crossing can be used to compute the amplitudes for all other processes involving 4 quarks and one gluon. Physical momenta will be labeled by p_a and p_b for initial partons while $p_i, (i = 1, 2 \ldots n)$ label the momenta of the final state partons.

In terms of physical momenta, the Born amplitude for the process

$$q(p_a) + Q(p_b) \to q(p_1) + Q(p_2) + g(p_3) + H(P), \quad [4.8]$$

is denoted by $\mathcal{M}^{qQ}_B = \mathcal{M}_B(p_a i_a, p_1 i_1, p_b i_b, p_2 i_2, p_3 c_3)$. $\mathcal{M}_B$ is the amplitude given in Eq. 4.1. The momentum of the Higgs boson P is determined by momentum conservation, i.e., $P = p_a + p_b - p_1 - p_2 - p_3$. The Born amplitude can be decomposed into color sub-amplitudes $\mathcal{M}^{qQ}_{B,1a}$ and $\mathcal{M}^{qQ}_{B,2b}$. The decomposition into color sub-amplitudes is

$$\mathcal{M}^{qQ}_B = t^{c_3}_{i_1 i_a}\delta_{i_2,i_b}\mathcal{M}^{qQ}_{B,1a} + t^{c_3}_{i_2 i_b}\delta_{i_1 i_a}\mathcal{M}^{qQ}_{B,2b}. \quad [4.9]$$

and the color averaged matrix element squared is

$$|\mathcal{M}_B^{qQ}|^2 = C_F(|\mathcal{M}_{B,1a}^{qQ}|^2 + |\mathcal{M}_{B,2b}^{qQ}|^2). \tag{4.10}$$

$\mathcal{M}_{B,1a}^{qQ} = \mathcal{M}_{B,1a}(p_1, p_3, p_a; p_2, p_b)$ denotes the color sub-amplitude for graphs with gluon emission off the quark line that connects the final state quark $q(p_1)$ to the initial state quark $q(p_a)$. This will be referred as emission off the upper line. Likewise, $\mathcal{M}_{B,2b}^{qQ} = \mathcal{M}_{B,2b}(p_2, p_3, p_b; p_1, p_a)$ denotes the color sub-amplitude for graphs with gluon emission off the quark line that connects the final state quark $Q(p_2)$ to the initial state quark $Q(p_b)$. This will be referred to as gluon emission off the lower line. One should take note that due to the color structure no interference can occur between gluon emission off the upper and lower lines.

The contribution of $qQ \to qQgH$ processes to the $Hjjj$ LO cross section is then

$$\begin{aligned} \sigma_3^{LO}(qQ \to qQgH) &= \int_0^1 dx_a \int_0^1 dx_b f_{q/p}(x_a, \mu_F) f_{Q/p}(x_b, \mu_F) \\ &\cdot \frac{1}{2\hat{s}} d\Phi_4(p_1, p_2, p_3, P; p_a + p_b) |\mathcal{M}_B^{qQ}|^2 F_J^{(3)}(p_1, p_2, p_3, P; p_a, p_b) \end{aligned} \tag{4.11}$$

where $\hat{s} = (p_a + p_b)^2$ is the center-of-mass energy squared. $F_J^{(3)}$ defines the jet algorithm for the 3-parton final states.

The Born amplitude for the gluon initiated process

$$g(p_a) + Q(p_b) \to q(p_1) + \bar{q}(p_3) + Q(p_2) + H(P), \tag{4.12}$$

is denoted by $\mathcal{M}_B^{gQ} = \mathcal{M}_B(-p_3 i_3, p_1 i_1, p_b i_b, p_2 i_2, -p_a c_a)$. Since, only vector-boson fusion processes are included there is only one color structure. The s-channel graphs have been neglected. The decomposition is as follows

$$\mathcal{M}_B^{gQ} = t_{i_1 i_3}^{c_a} \delta_{i_2 i_b} \mathcal{M}_{B,13}(p_1, -p_a, -p_3; p_2, p_b) \tag{4.13}$$

and the matrix element square averaged over colors is

$$|\mathcal{M}_B^{gQ}|^2 = \frac{C_F d_F}{d_G} |\mathcal{M}_{B,13}(p_1, -p_a, -p_3; p_2, p_b)|^2 \tag{4.14}$$

where d_F and d_G are the number of colors for quarks and gluons respectively.

The contribution of $gQ \to q\bar{q}QH$ processes to $Hjjj$ LO cross section is then

$$\begin{aligned}\sigma_3^{LO}(gQ \to q\bar{q}QH) &= \int_0^1 dx_a \int_0^1 dx_b f_{g/p}(x_a,\mu_F) f_{Q/p}(x_b,\mu_F) \\ &\cdot \frac{1}{2\hat{s}} d\Phi_4(p_1,p_2,p_3,P;p_a+p_b)|\mathcal{M}_B^{gQ}|^2 F_J^{(3)}(p_1,p_2,p_3,P;p_a,p_b).\end{aligned} \quad [4.15]$$

There is also a contribution due to the interchange of the initial state quark and gluon, i.e. $Qg \to q\bar{q}QH$.

4.3 The Next-to-Leading Order Cross Section

In this Subsection analytic formulas for the NLO 4-parton and 3-parton cross sections for $pp \to Hjjj$ are presented. In Subsection 4.3.1 the real emission corrections and the dipole subtraction method is discussed. In Subsection 4.3.2 formulae for the virtual corrections are given.

4.3.1 Real Emission Corrections and Dipole Subtraction

The real emission corrections for Higgs production in the association of three jets via vector boson fusion ($Hjjj$) consist of four subprocess classes:

(a) subprocesses in which there are two gluons and two quarks in the final state, $qQ \to qQggH$,

(b) subprocesses with six external quarks, $qQ \to qQq'\bar{q}'H$,

(c) subprocesses which have one gluon in the initial state, $gQ \to q\bar{q}QgH$, and

(d) subprocesses which have two gluons in the initial state, $gg \to q\bar{q}Q\bar{Q}H$.

The matrix elements squares, $|\mathcal{M}|^2$, for the above subprocess classes contain both soft and collinear singularities. These singularities are regulated by use of the dipole subtraction method of Ref.[21].

The matrix element for the subprocess,

$$q(p_a) + Q(p_b) \to q(p_1) + Q(p_2) + g(p_3) + g(p_4) + H(P) \quad [4.16]$$

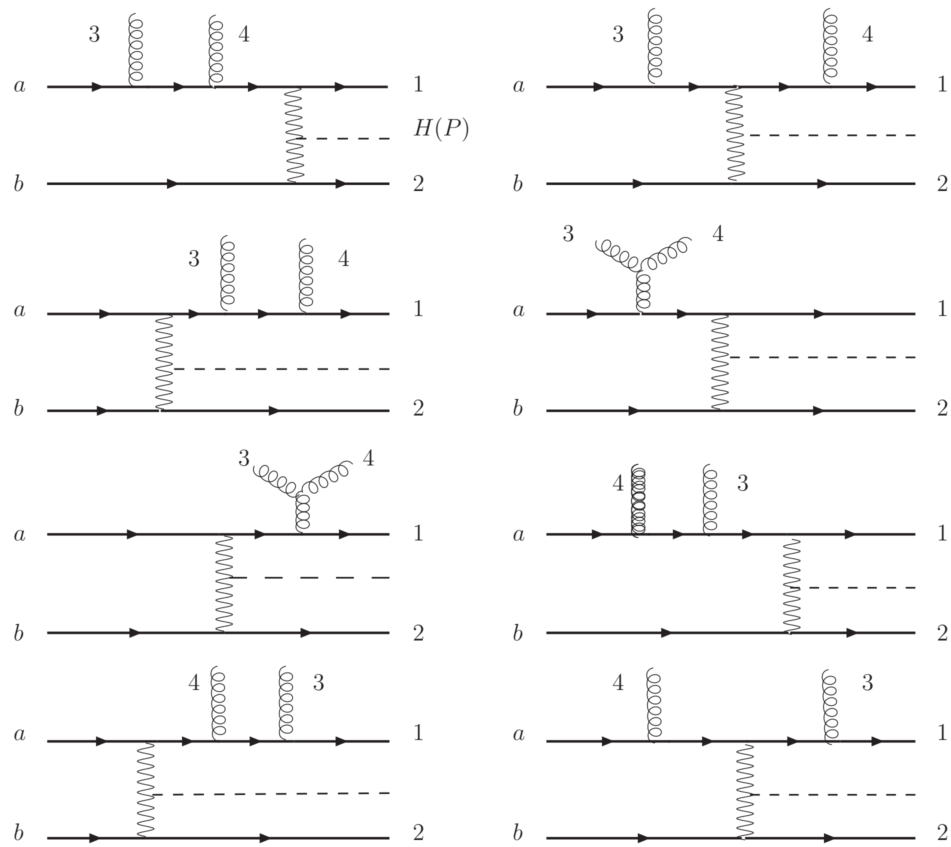

Figure 4.2 Feynman graphs for $\mathcal{M}_r^{qQ}$ for which two external gluons are attached to the $1a$ quark line.

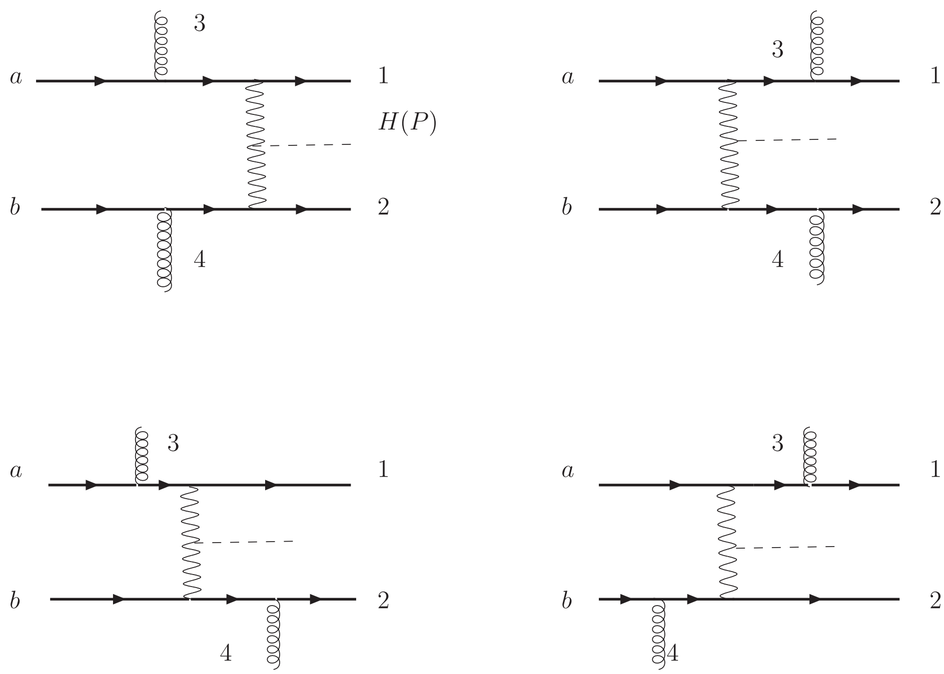

Figure 4.3 Feynman graphs for $\mathcal{M}_r^{qQ}$ for which an external gluon is attached to both the $1a$ and $2b$ quark lines.

depicted in Figures 4.2 and 4.3 is denoted by $\mathcal{M}_r^{qQ} = \mathcal{M}_r^{qQ}(p_1, p_2, p_3, p_4, P; p_a, p_b)$. $\mathcal{M}_r^{qQ}$ can be written in terms of color tensors, $T^{(k)}$, and color sub-amplitudes, $\mathcal{M}_r^{qQ,(k)}$.

$$\mathcal{M}_r^{qQ} = \sum_{k=1}^{6} T^{(k)} \mathcal{M}_r^{qQ,(k)}, \tag{4.17}$$

with

$$T^{(1)} = (t^{a_3} t^{a_4})_{i_1 i_a} \delta_{i_2 i_b}, \tag{4.18}$$

$$T^{(2)} = (t^{a_4} t^{a_3})_{i_1 i_a} \delta_{i_2 i_b}, \tag{4.19}$$

$$T^{(3)} = (t^{a_3} t^{a_4})_{i_2 i_b} \delta_{i_1 i_a}, \tag{4.20}$$

$$T^{(4)} = (t^{a_4} t^{a_3})_{i_2 i_b} \delta_{i_1 i_a}, \tag{4.21}$$

$$T^{(5)} = t^{a_3}_{i_1 i_a} t^{a_4}_{i_2 i_b}, \tag{4.22}$$

$$T^{(6)} = t^{a_4}_{i_1 i_a} t^{a_3}_{i_2 i_b}. \tag{4.23}$$

It is possible to write the color tensors $T^{(k)}$ in terms of orthogonal color tensors in order to compute the matrix element squared, $|\mathcal{M}_r^{qQ}|^2$. However, for what follows it is sufficient to simply square Eqs. (4.17). Color factors are defined as $C_{kl} = \mathrm{Tr}\left(T^{(k)\dagger} T^{(l)}\right)$. Hence, the matrix element squared takes the form,

$$|\mathcal{M}_r^{qQ}|^2 = \sum_{k=1}^{6} \sum_{l=1}^{6} C_{kl} \mathcal{M}_r^{qQ(k)\dagger} \mathcal{M}_r^{qQ(l)}. \tag{4.24}$$

The non-zero color factors, C_{kl}, are

$$C_{11} = C_{22} = C_{33} = C_{44} = C_{55} = C_{66} = d_F^2 C_F^2, \tag{4.25}$$

$$C_{12} = C_{34} = d_F^2 C_F (C_F - \frac{1}{2} C_A), \tag{4.26}$$

$$C_{13} = C_{14} = C_{23} = C_{24} = C_{56} = \frac{d_F^2 C_F^2}{d_G}. \tag{4.27}$$

Here $d_G = N^2 - 1$ and $d_F = N$ where N is number of colors in an $SU(N)$ gauge group.

The various color-sub-amplitudes can be grouped into double gluon emission off the $a1$ quark line, double gluon emission off the $b2$ quark line, and gluon emission off both quark lines. Graphs for which gluons are emitted off both quark lines do not interfere with graphs for which two gluons are emitted off a single quark line. Color sub-amplitudes, $\mathcal{M}^{(6)}$ and $\mathcal{M}^{(5)}$, are orthogonal to the sub-amplitudes, $\mathcal{M}^{(k)}$ for $k = 1$ to 4. Inserting the color factors, C_{kl} into Eq. 4.24, the matrix element squared takes the form

$$\begin{aligned}|\mathcal{M}_r^{qQ}|^2 &= d_F^2 C_F^2 (|\mathcal{M}^{(1)}|^2 + |\mathcal{M}^{(2)}|^2 + |\mathcal{M}^{(3)}|^2 + |\mathcal{M}^{(4)}|^2 + |\mathcal{M}^{(5)}|^2 + |\mathcal{M}^{(6)}|^2) \\ &+ 2\mathrm{Re}[\mathcal{M}^{(1)}\mathcal{M}^{(2)\dagger} + \mathcal{M}^{(3)}\mathcal{M}^{(4)\dagger}] d_F^2 C_F (C_F - \frac{1}{2} C_A) \\ &+ 2\mathrm{Re}[(\mathcal{M}^{(1)} + \mathcal{M}^{(2)})(\mathcal{M}^{(3)} + \mathcal{M}^{(4)})^\dagger] \frac{d_F^2 C_F^2}{d_G} \\ &+ \frac{d_F^2 C_F^2}{d_G} 2\mathrm{Re}[\mathcal{M}^{(5)}\mathcal{M}^{(6)\dagger}]. \end{aligned} \tag{4.28}$$

The terms $2\ \mathrm{Re}[\mathcal{M}^{(5)\dagger}\mathcal{M}^{(6)}]$ and $2\ \mathrm{Re}[(\mathcal{M}^{(1)} + \mathcal{M}^{(2)})(\mathcal{M}^{(3)} + \mathcal{M}^{(4)})^\dagger]$ are interference terms that are color suppressed by $1/d_G = 1/(N^2 - 1)$. Besides being color suppressed there are kinematic suppressions that arise. For the VBF process $qQ \to qQggH$ the two forward tagging jets are typically final state quarks. Gluon radiation typically occurs in the direction of the tagging jets. Consider the case in which gluon $g(p_3)$ is along the direction of $q(p_1)$. The fermion propagators in $\mathcal{M}^{(1)}$, $\mathcal{M}^{(2)}$, and $\mathcal{M}^{(5)}$ are enhanced while the fermion propagators in $\mathcal{M}^{(3)}$, $\mathcal{M}^{(4)}$, and $\mathcal{M}^{(6)}$ become suppressed due to the large invariant mass of the two tagging quarks jets. These interference effects are collinear finite but do give rise to soft singularities. In the soft limit the interference terms are proportional to the interference of the Born sub-amplitudes $\mathcal{M}_{B,1a}^{qQ}$ and $\mathcal{M}_{B,2b}^{qQ}$. Using a LO parton-level Monte Carlo program for Higgs production in the association with three jets via VBF, the contribution from the above mentioned interference term to the cross section is computed using

$$\frac{C_F^2}{d_G}\frac{\alpha_s}{2\pi} 2|\mathrm{Re}[\mathcal{M}_{B,1a}^{qQ}(\mathcal{M}_{B,2b}^{qQ})^\dagger]| \tag{4.29}$$

in place of the matrix element squared given by Eq.(4.10). The sum over helicities τ_a and τ_b is performed on the absolute value of $\mathrm{Re}[\mathcal{M}_{B,1a}^{qQ}(\mathcal{M}_{B,2b}^{qQ})^\dagger]$ to ensure that there are no cancellations that result when the sum over subprocesses occurs. The normalized distribution in the rapidity of the veto jet measured with respect to the rapidity average of the tagging jets, $y_{rel} = y_j^{\mathrm{veto}} - (y_j^{\mathrm{tag}\ 1} + y_j^{\mathrm{tag}\ 2})/2$, is shown for both interference given by Eq.(4.29) and the Born matrix element squared

$|\mathcal{M}_B^{qQ}|^2$ stated in Eq.(4.10) in the left panel of Figure 4.4.[1] Both distributions are normalized to total cross section due to either the Born matrix element squared or the interference. In the left panel Figure 4.4 depicts the ratio R defined as

$$R(y_{rel}) = \frac{d\sigma_3^{\text{int}}/dy_{\text{rel}}}{d\sigma_3^{LO}/dy_{\text{rel}}}. \qquad [4.30]$$

Here σ_3^{int} denotes the cross section due to the interference term given by Eq.(4.29) while σ_3^{LO} denotes the cross section resulting from the Born amplitude squared given by Eq.(4.10). The interference term (Eq.(4.29)) is maximal for $y_{rel} = 0$ when the veto jet is in the center of the two tagging jets while the Born matrix element squared (Eq.(4.10)) is maximal for $y_{rel} = \pm 2$. The ratio R has a maximum value of 10^{-4} which is quite small. The terms $2\ \text{Re}[\mathcal{M}^{(5)\dagger}\mathcal{M}^{(6)}]$ and $2\ \text{Re}[(\mathcal{M}^{(1)} + \mathcal{M}^{(2)})(\mathcal{M}^{(3)} + \mathcal{M}^{(4)})^\dagger]$ are then suppressed both by kinematics and color factors. For these reasons these terms will be neglected.

The approximate matrix element square is then

$$\begin{aligned} |\mathcal{M}_r^{qQ}|^2_{\text{approx}} &= d_F^2 C_F^2 \sum_{k=1}^{6} |\mathcal{M}^{(k)}|^2 \\ &+ 2\ \text{Re}[\mathcal{M}^{(1)}\mathcal{M}^{(2)\dagger} + \mathcal{M}^{(3)}\mathcal{M}^{(4)\dagger}] d_F^2 C_F (C_F - \frac{1}{2} C_A)). \end{aligned} \qquad [4.31]$$

The computer code for the real emission matrix elements squared $|\mathcal{M}_r^{qQ}|^2$ for the subprocess $qQ \to qQggH$ has been generated by MADGRAPH [48]. There are 24 Feynman graphs. In order to compute Eq.(4.31) numerically from the MADGRAPH generated code, the color factors are chosen to be

$$C_{11} = C_{22} = C_{33} = C_{44} = C_{55} = C_{66} = d_F^2 C_F^2, \qquad [4.32]$$

$$C_{12} = C_{34} = d_F^2 C_F (C_F - \frac{1}{2} C_A), \qquad [4.33]$$

$$C_{13} = C_{14} = C_{23} = C_{24} = C_{56} = 0. \qquad [4.34]$$

From this point forward, it will be understood that $|\mathcal{M}_r^{qQ}|^2$ is actually $|\mathcal{M}_r^{qQ}|^2_{\text{approx}}$ given by Eq.(4.31).

[1] The veto cuts used here are given by Eq.(5.13).

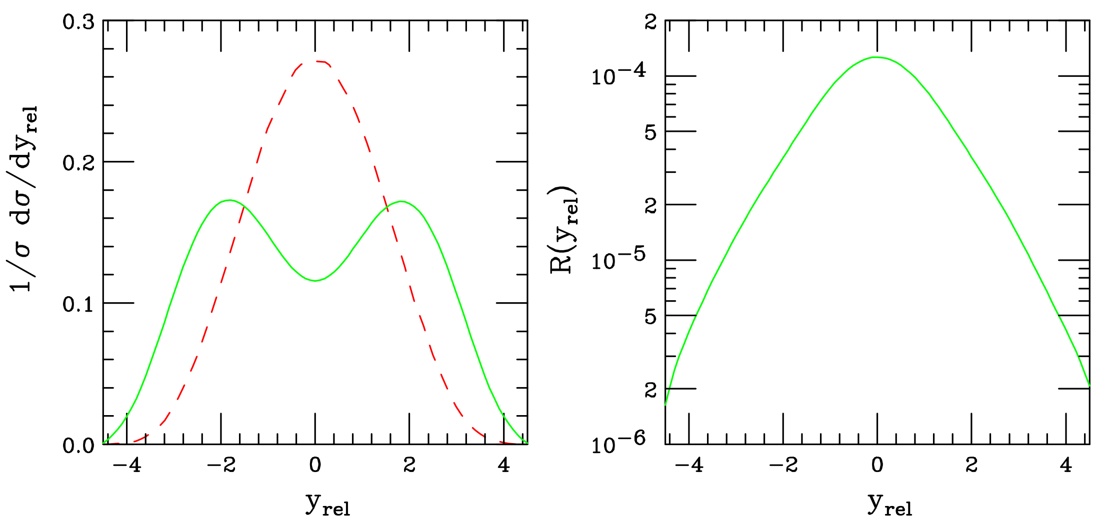

Figure 4.4 The normalized distribution in the rapidity of the veto jet with respect to the center of rapidity for the two tagging jets, $y_{rel} = y_j^{\text{veto}} - (y_j^{\text{tag 1}} + y_j^{\text{tag 2}})/2$, for $Hjjj$ production at LO. In the left panel $\frac{1}{\sigma}\frac{d\sigma}{dy_{rel}}$ is plotted against y_{rel} for the interference term given by Eq.(4.29) (dashed curve) and the Born matrix element squared given by Eq.(4.10) (solid curve). In the right panel the ratio $R(y_{rel})$ is plotted against y_{rel}.

The soft and collinear singularities are regulated by use of Catani-Seymour dipole subtraction method [21]. In the approximation that is being made, one neglects color correlations between upper and lower quark lines. Table 4.1 lists dipoles for the process $qQ \to qQggH$ for the approximation being made here. In Table 4.1 the translation from the notation of Ref.[21], CS notation, to the notation of Ref.[50], CE notation, is given. The dipoles $D^{ij,k}_{ff,qq}$ are given in Appendix A for conventional dimensional regularization (CDR) as opposed to the dimensional reduction (DR) form given in Ref.[50]. As a check, calculations have been performed in both DR and CDR schemes. Although there are differences that arise during intermediate stages of the NLO calculation, the final results are independent of regularization scheme. Here CDR is used throughout. The dipoles which are proportional to the interference between upper and lower line Born amplitudes are listed in Table 4.2. The 4-parton contribution to the NLO cross section from $qQ \to qQggH$ processes is

$$\begin{aligned} \sigma_4^{NLO}(qQ \to qQggH) &= \int_0^1 dx_a \int_0^1 dx_b f_{q/p}(x_a,\mu_F) f_{Q/p}(x_b,\mu_F) \frac{1}{2\hat{s}} d\Phi_5(p_1,p_2,p_3,p_4,P;p_a+p_b) \\ &\cdot \frac{1}{2!}\{|\mathcal{M}_r^{qQ}|^2 F_J^{(4)}(p_1,p_2,p_3,p_4;p_a,p_b) - \sum_{i=1}^{20} \mathcal{D}(i)\cdot F_J^{(3)}(i)\} \end{aligned} \qquad [4.35]$$

where the dipoles $\mathcal{D}(i)$ are listed in Table 4.1. The index i specifies the momentum configuration. For $\mathcal{D}(i)$ the label i refers to the real emission kinematics and for $F_J^{(3)}(i)$ the label i refers to the transformed Born-level kinematics. For example, using Table 4.1 one would have $\mathcal{D}(1) = \mathcal{D}_{14,3}(1^q,2^Q,3^g,4^g;a^q,b^Q)$ for the real emission process and $F_J^{(3)}(1) = F_J^{(3)}(\tilde{14}^q,2^Q,\tilde{3}^g;a^q,b^Q)$. Here the momentum and flavor of the parton is labeled by a and b for initial state partons and by a whole number for final state partons. The superscripts g and q label the flavor of the parton. For example, $(1^q,2^Q,3^g,4^g;a^q,b^Q)$ represents the real emission process

$$q(p_a)+Q(p_b) = q(p_1)+Q(p_2)+g(p_3)+g(p_4)+H(P) \qquad [4.36]$$

and $(\tilde{14}^q,2^Q,\tilde{3}^g;a^q,b^Q)$ represents the Born-level process

$$q(p_a)+Q(p_b) \to q(\tilde{p}_{14})+Q(p_2)+g(\tilde{p}_3)+H(P) \qquad [4.37]$$

with transformed momenta, $(\tilde{p}_{14},p_2,\tilde{p}_3;p_a,p_b)$. General formulae for the transformed (Born-level) momenta can be found in Appendix A.

The amplitude for the subprocess

$$g(p_a) + g(p_b) \rightarrow q(p_1) + Q(p_2) + \bar{q}(p_3) + \bar{Q}(p_4) + H(P) \qquad [4.38]$$

is denoted by $\mathcal{M}_r(1^q, 2^Q, 3^{\bar{q}}, 4^{\bar{Q}}; a^g, b^g)$. Collinear singularities occur when the initial state gluon becomes collinear with one of the final state (anti-) quarks. Dipoles for this process are listed in Table 4.5. All of the dipoles listed subtract initial state singularities with final state spectators. In terms of color sub-amplitudes,

$$\mathcal{M}_r(1^q, 2^Q, 3^{\bar{q}}, 4^{\bar{Q}}; a^g, b^g) = t^a_{i_1 i_3} t^b_{i_2 i_4} \mathcal{M}(31, 42) + t^b_{i_1 i_3} t^a_{i_2 i_4} \mathcal{M}(42, 31). \qquad [4.39]$$

$\mathcal{M}(31, 42)$ represents the the graph with the quark current J_{31} attached to gluon a and quark current J_{42} attached to gluon b. The matrix element squared is then

$$\begin{aligned} |\mathcal{M}_r(1^q, 2^Q, 3^{\bar{q}}, 4^{\bar{Q}}; a^g, b^g)|^2 &= \frac{N^2 C_F^2}{d_G^2}(|\mathcal{M}(31, 42)|^2 + |\mathcal{M}(43, 31)|^2) \\ &+ \frac{N^2 C_F^2}{d_G^3} 2\,\mathrm{Re}[\mathcal{M}(31, 42)^* \mathcal{M}(42, 31)]. \end{aligned} \qquad [4.40]$$

To be consistent the second term in Eq. (4.40) is neglected since it is suppressed by color and kinematics. $|\mathcal{M}(31, 42)|^2$ and $|\mathcal{M}(43, 31)|^2$ integrate to the same cross section contribution. This being the case, only four dipoles need to be considered. The 4-parton contribution to the NLO cross section is then

$$\begin{aligned} \sigma_4^{NLO}(gg \rightarrow q\bar{q}Q\bar{Q}H) &= \int_0^1 dx_a \int_0^1 dx_b f_{g/p}(x_a, \mu_F) f_{g/p}(x_b, \mu_F) \frac{1}{2\hat{s}} d\Phi_5(p_1, p_2, p_3, p_4, P; p_a + p_b) \\ &\cdot \quad \{|\mathcal{M}_r^{gg}|^2 F_J^{(4)}(p_1, p_2, p_3, p_4; p_a, p_b) - \sum_{i=1}^{4} \mathcal{D}(i) \cdot F_J^{(3)}(i)\} \end{aligned} \qquad [4.41]$$

where $\mathcal{M}_r^{gg} = t^a_{i_1 i_3} t^b_{i_2 i_4} \mathcal{M}(31, 42)$. The dipoles $\mathcal{D}(i)$ are listed in Table 4.5. Dipoles for subprocesses $qQ \rightarrow qQq'\bar{q}'H$ and $gQ \rightarrow q\bar{q}QgH$ are given in Tables 4.3 and 4.4, respectively. The tensor $T_{\mu\nu}$ in Tables 4.3 and 4.4 is the uncontracted matrix element squared,

$$T_{\mu\nu} = \mathcal{M}_\mu (\mathcal{M}_\nu)^* \qquad [4.42]$$

where the μ and ν are gluon spin-indices. The matrix element squared is then

$$|\mathcal{M}|^2 = \sum_\lambda T_{\mu\nu} \epsilon^\mu(q, \lambda) \epsilon^{\nu *}(q, \lambda) = -g^{\mu\nu} T_{\mu\nu} \qquad [4.43]$$

where the sum over gluon polarizations, λ, has been performed.

Table 4.1 Dipole factors for $qQ \to qQggH$ processes. The color sub-amplitudes are $A = \mathcal{M}^{qQ}_{B,2b}(i)$ and $B = \mathcal{M}^{qQ}_{B,1a}(i)$ with Born-level momentum i. The color coefficients C_l are $C_1 = C_F^2$, $C_2 = C_F(C_F - \frac{1}{2}C_A)$, and $C_3 = \frac{1}{2}C_F C_A$.

	Real kinematics	$(1^q, 2^Q, 3^g, 4^g; a^q, b^Q)$
i	Dipole factor	Born kinematics
1	$\mathcal{D}_{14,3} = C_3 \lvert B\rvert^2 \mathcal{D}^{14,3}_{ff,qq}$	$(\widetilde{14}^q, 2^Q, \tilde{3}^g; a^q, b^Q)$
2	$\mathcal{D}_{13,4} = C_3 \lvert B\rvert^2 \mathcal{D}^{13,4}_{ff,qq}$	$(\widetilde{13}^q, 2^Q, \tilde{4}^g; a^q, b^Q)$
3	$\mathcal{D}_{34,1} = C_3(-g^{\mu\nu}\mathcal{D}^{34,1}_{ff,gg} + q^\mu q^\nu \tilde{\mathcal{D}}^{34,1}_{ff,gg}) B_\mu B^*_\nu$	$(\tilde{1}^q, 2^Q, \widetilde{34}^g; a^q, b^Q)$
4	$\mathcal{D}^a_{14} = \{C_1 \lvert A\rvert^2 + C_2 \lvert B\rvert^2\} \mathcal{D}^{14,a}_{fi,qq}$	$(\widetilde{14}^q, 2^Q, 3^g; \tilde{a}^q, b^Q)$
5	$\mathcal{D}^a_{13} = \{C_1 \lvert A\rvert^2 + C_2 \lvert B\rvert^2\} \mathcal{D}^{13,a}_{fi,qq}$	$(\widetilde{13}^q, 2^Q, 4^g; \tilde{a}^q, b^Q)$
6	$\mathcal{D}^a_{34} = C_3(-g^{\mu\nu}\mathcal{D}^{34,a}_{fi,gg} + q^\mu q^\nu \tilde{\mathcal{D}}^{34,a}_{fi,gg}) B_\mu B^*_\nu$	$(1^q, 2^Q, \widetilde{34}^g; \tilde{a}^q, b^Q)$
7	$\mathcal{D}^{a4}_1 = \{C_1 \lvert A\rvert^2 + C_2 \lvert B\rvert^2\} \mathcal{D}^{a4,1}_{if,qq}$	$(\tilde{1}^q, 2^Q, 3^g; \widetilde{a4}^q, b^Q)$
8	$\mathcal{D}^{a3}_1 = \{C_1 \lvert A\rvert^2 + C_2 \lvert B\rvert^2\} \mathcal{D}^{a3,1}_{if,qq}$	$(\tilde{1}^q, 2^Q, 4^g; \widetilde{a3}^q, b^Q)$
9	$\mathcal{D}^{a4}_3 = C_3 \lvert B\rvert^2 \mathcal{D}^{a4,3}_{if,qq}$	$(1^q, 2^Q, \tilde{3}^g; \widetilde{a4}^q, b^Q)$
10	$\mathcal{D}^{a3}_4 = C_3 \lvert B\rvert^2 \mathcal{D}^{a3,4}_{if,qq}$	$(1^q, 2^Q, \tilde{4}^g; \widetilde{a3}^q, b^Q)$
11	$\mathcal{D}_{24,3} = C_3 \lvert A\rvert^2 \mathcal{D}^{24,3}_{ff,qq}$	$(1^q, \widetilde{24}^Q, \tilde{3}^g; a^q, b^Q)$
12	$\mathcal{D}_{23,4} = C_3 \lvert A\rvert^2 \mathcal{D}^{23,4}_{ff,qq}$	$(1^q, \widetilde{23}^Q, \tilde{4}^g; a^q, b^Q)$
13	$\mathcal{D}_{34,2} = C_3(-g^{\mu\nu}\mathcal{D}^{34,2}_{ff,gg} + q^\mu q^\nu \tilde{\mathcal{D}}^{34,2}_{ff,gg}) A_\mu A^*_\nu$	$(1^q, \tilde{2}^Q, \widetilde{34}^g; a^q, b^Q)$
14	$\mathcal{D}^b_{24} = \{C_1 \lvert B\rvert^2 + C_2 \lvert A\rvert^2\} \mathcal{D}^{24,b}_{fi,qq}$	$(1^q, \widetilde{24}^Q, 3^g; a^q, \tilde{b}^Q)$
15	$\mathcal{D}^b_{23} = \{C_1 \lvert B\rvert^2 + C_2 \lvert A\rvert^2\} \mathcal{D}^{23,b}_{fi,qq}$	$(1^q, \widetilde{23}^Q, 4^g; a^q, \tilde{b}^Q)$
16	$\mathcal{D}^b_{34} = C_3(-g^{\mu\nu}\mathcal{D}^{34,b}_{fi,gg} + q^\mu q^\nu \tilde{\mathcal{D}}^{34,b}_{fi,gg}) A_\mu A^*_\nu$	$(1^q, 2^Q, \widetilde{34}^g; a^q, \tilde{b}^Q)$
17	$\mathcal{D}^{b4}_2 = \{C_1 \lvert B\rvert^2 + C_2 \lvert A\rvert^2\} \mathcal{D}^{b4,2}_{if,qq}$	$(1^q, \tilde{2}^Q, 3^g; a^q, \widetilde{b4}^Q)$
18	$\mathcal{D}^{b3}_2 = \{C_1 \lvert B\rvert^2 + C_2 \lvert A\rvert^2\} \mathcal{D}^{b3,2}_{if,qq}$	$(1^q, \tilde{2}^Q, 4^g; a^q, \widetilde{b3}^Q)$
19	$\mathcal{D}^{b4}_3 = C_3 \lvert A\rvert^2 \mathcal{D}^{b4,3}_{if,qq}$	$(1^q, 2^Q, \tilde{3}^g; a^q, \widetilde{b4}^Q)$
20	$\mathcal{D}^{b3}_4 = C_3 \lvert A\rvert^2 \mathcal{D}^{b3,4}_{if,qq}$	$(1^q, 2^Q, \tilde{4}^g; a3^q, \widetilde{b3}^Q)$

Table 4.2 Dipoles for $qQ \to qQggH$ processes that are color suppressed.

	Real kinematics	$(1^q, 2^Q, 3^g, 4^g; a^q, b^Q)$
i	Dipole factor	Born kinematics
21	$\mathcal{D}^{a4,b}$	$(1^q, 2^Q, 3^g; \widetilde{a4}^q, \tilde{b}^Q)$
22	$\mathcal{D}^{b4,a}$	$(1^q, 2^Q, 3^g; \tilde{a}^q, \widetilde{b4}^Q)$
23	$\mathcal{D}_{24}^{a}$	$(1^q, \widetilde{24}^Q, 3^g; \tilde{a}^q, b^Q)$
24	$\mathcal{D}_{14}^{b}$	$(\widetilde{14}^q, 2^Q, 3^g; a^q, \tilde{b}^Q)$
25	$\mathcal{D}_{2}^{a4}$	$(1^q, \tilde{2}^Q, 3^g; \widetilde{a4}^q, b^Q)$
26	$\mathcal{D}_{1}^{b4}$	$(\tilde{1}^q, 2^Q, 3^g; a^q, \widetilde{b4}^Q)$
27	$\mathcal{D}_{24,1}$	$(\tilde{1}^q, \widetilde{24}^Q, 3^g; a^q, b^Q)$
28	$\mathcal{D}_{14,2}$	$(\widetilde{14}^q, \tilde{2}^Q, 3^g; a^q, b^Q)$
29	$\mathcal{D}_{23}^{a}$	$(1^q, \widetilde{23}^Q, 4^g; \tilde{a}^q, b^Q)$
30	$\mathcal{D}_{13}^{b}$	$(\widetilde{13}^q, 2^Q, 4^g; a^q, \tilde{b}^Q)$
31	$\mathcal{D}_{2}^{a3}$	$(1^q, \tilde{2}^Q, 4^g; \widetilde{a3}^q, b^Q)$
32	$\mathcal{D}_{1}^{b3}$	$(\tilde{1}^q, 2^Q, 4^g; a^q, \widetilde{b3}^Q)$
33	$\mathcal{D}^{23,1}$	$(\tilde{1}^q, \widetilde{23}^Q, 4^g; a^q, b^Q)$
34	$\mathcal{D}^{13,2}$	$(\widetilde{13}^q, \tilde{2}^Q, 4^g; a^q . b^Q)$

Table 4.3 Dipole factors for $qQ \to qQq'\bar{q}'H$ processes. Here $T^{gQ}_{\mu\nu} = \mathcal{M}^{gQ}_{\mu}\mathcal{M}^{gQ*}_{\nu}$ and $T^{qg}_{\mu\nu} = \mathcal{M}^{qg}_{\mu}\mathcal{M}^{qg*}_{\nu}$. $A = \mathcal{M}^{qQ}_{B,2b}(i)$ and $B = \mathcal{M}^{qQ}_{B,1a}(i)$ for Born-level momentum i.

	Real kinematics	$(1^q, 2^Q, 3^{q'}, 4^{\bar{q}'}; a^q, b^Q)$
i	Dipole	Born kinematics
1	$\mathcal{D}_{34,1} = \frac{1}{2}C_F T_F(-g^{\mu\nu}\mathcal{D}^{34,1}_{ff,gq} + q^\mu q^\nu \tilde{\mathcal{D}}^{34,1}_{ff,gq})B_\mu B^*_\nu$	$(\tilde{1}^q, 2^Q, \tilde{34}^g; a^q, b^Q)$
2	$\mathcal{D}_{34,2} = \frac{1}{2}C_F T_F(-g^{\mu\nu}\mathcal{D}^{34,2}_{ff,gq} + q^\mu q^\nu \tilde{\mathcal{D}}^{34,2}_{ff,gq})A_\mu A^*_\nu$	$(1^q, \tilde{2}^Q, \tilde{34}^g; a^q, b^Q)$
3	$\mathcal{D}^a_{34} = \frac{1}{2}C_F T_F(-g^{\mu\nu}\mathcal{D}^{34,a}_{fi,gq} + q^\mu q^\nu \tilde{\mathcal{D}}^{34,a}_{fi,gq})B_\mu B^*_\nu$	$(1^q, 2^Q, \tilde{34}^g; \tilde{a}^q, b^Q)$
4	$\mathcal{D}^b_{34} = \frac{1}{2}C_F T_F(-g^{\mu\nu}\mathcal{D}^{34,b}_{fi,gq} + q^\mu q^\nu \tilde{\mathcal{D}}^{34,b}_{fi,gq})A_\mu A^*_\nu$	$(1^q, 2^Q, \tilde{34}^g; a^q, \tilde{b}^Q)$
5	$\mathcal{D}^{a1}_3 = \frac{1}{2}C_F(-g^{\mu\nu}\mathcal{D}^{a1,3}_{if,gq} + q^\mu q^\nu \tilde{\mathcal{D}}^{a1,3}_{if,gq})T^{gQ}_{\mu\nu}$	$(2^Q, \tilde{3}^{q'}, 4^{\bar{q}'}; \tilde{a1}^g, b^Q)$
6	$\mathcal{D}^{a1}_4 = \frac{1}{2}C_F(-g^{\mu\nu}\mathcal{D}^{a1,4}_{if,gq} + q^\mu q^\nu \tilde{\mathcal{D}}^{a1,4}_{if,gq})T^{gQ}_{\mu\nu}$	$(2^Q, 3^{q'}, \tilde{4}^{\bar{q}'}; \tilde{a1}^g, b^Q)$
7	$\mathcal{D}^{b2}_3 = \frac{1}{2}C_F(-g^{\mu\nu}\mathcal{D}^{b2,3}_{if,gq} + q^\mu q^\nu \tilde{\mathcal{D}}^{b2,3}_{if,gq})T^{qg}_{\mu\nu}$	$(1^q, \tilde{3}^{q'}, 4^{\bar{q}'}; a^q, \tilde{b2}^g)$
8	$\mathcal{D}^{b2}_4 = \frac{1}{2}C_F(-g^{\mu\nu}\mathcal{D}^{b2,4}_{if,gq} + q^\mu q^\nu \tilde{\mathcal{D}}^{b2,4}_{if,gq})T^{qg}_{\mu\nu}$	$(1^q, 3^{q'}, \tilde{4}^{\bar{q}'}; a^q, \tilde{b2}^g)$

Table 4.4 Dipole factors for $gQ \to q\bar{q}QgH$ processes. Here the color factors: $C_1 = C_F$, $C_2 = C_F - \frac{1}{2}C_A$, and $C_3 = \frac{1}{2}C_A$. $T^{gQ}_{\mu\nu} = \mathcal{M}^{gQ}_{\mu}\mathcal{M}^{gQ*}_{\nu}$ for Born-level momentum i.

	Real kinematics	$(1^q, 2^Q, 3^{\bar{q}}, 4^g; a^g, b^Q)$
i	Dipole factor	Born kinematics
1	$\mathcal{D}_1^{a3} = \{C_1\vert A^{qQ}\vert^2 + C_2\vert B^{qQ}\vert^2\}T_F\mathcal{D}^{a3,1}_{if,qg}$	$(\tilde{1}^q, 2^Q, 4^g; \widetilde{a3}^q, b^Q)$
2	$\mathcal{D}_3^{a1} = \{C_1\vert A^{\bar{q}Q}\vert^2 + C_2\vert B^{\bar{q}Q}\vert^2\}T_F\mathcal{D}^{a1,3}_{if,qg}$	$(2^Q, 3^{\bar{q}}, 4^g; \widetilde{a1}^{\bar{q}}, b^Q)$
3	$\mathcal{D}_4^{a3} = C_3\vert B^{qQ}\vert^2 T_F\mathcal{D}^{a3,4}_{if,qg}$	$(1^q, 2^Q, \tilde{4}^g; \widetilde{a3}^q, b^Q)$
4	$\mathcal{D}_4^{a1} = C_3\vert B^{\bar{q}Q}\vert^2 T_F\mathcal{D}^{a1,4}_{if,qg}$	$(2^Q, 3^{\bar{q}}, \tilde{4}^g; \widetilde{a1}^q, b^Q)$
5	$\mathcal{D}_1^{a4} = C_3(-g^{\mu\nu}\mathcal{D}^{a4,1}_{if,gg} + q^\mu q^\nu \tilde{\mathcal{D}}^{a4,1}_{if,gg})T^{gQ}_{\mu\nu}$	$(\tilde{1}^q, 2^Q, 3^{\bar{q}}; \widetilde{a4}^g, b^Q)$
6	$\mathcal{D}_3^{a4} = C_3(-g^{\mu\nu}\mathcal{D}^{a4,3}_{if,gg} + q^\mu q^\nu \tilde{\mathcal{D}}^{a4,3}_{if,gg})T^{gQ}_{\mu\nu}$	$(1^q, 2^Q, \tilde{3}^{\bar{q}}; \widetilde{a4}^g, b^Q)$
7	$\mathcal{D}_2^{b4} = C_1\vert\mathcal{M}^{gQ}\vert^2\mathcal{D}^{b4,2}_{if,qq}$	$(1^q, \tilde{2}^Q, 3^{\bar{q}}; a^g, \widetilde{b4}^Q)$
8	$\mathcal{D}^b_{24} = C_1\vert\mathcal{M}^{gQ}\vert^2\mathcal{D}^{24,b}_{fi,qq}$	$(1^q, \widetilde{24}^Q, 3^{\bar{q}}; a^g, \tilde{b}^Q)$
9	$\mathcal{D}^a_{14} = C_3\vert\mathcal{M}^{gQ}\vert^2\mathcal{D}^{14,a}_{fi,qq}$	$(\widetilde{14}^q, 2^Q, 3^{\bar{q}}; \tilde{a}^g, b^Q)$
10	$\mathcal{D}^a_{34} = C_3\vert\mathcal{M}^{gQ}\vert^2\mathcal{D}^{34,a}_{fi,qq}$	$(1^q, 2^Q, \widetilde{34}^{\bar{q}}; \tilde{a}^g, b^Q)$
11	$\mathcal{D}_{14,3} = C_2\mathcal{M}^{gQ}\vert^2\mathcal{D}^{14,3}_{ff,qq}$	$(\widetilde{14}^q, 2^Q, \tilde{3}^{\bar{q}}; a^g, b^Q)$
12	$\mathcal{D}_{34,1} = C_2\mathcal{M}^{gQ}\vert^2\mathcal{D}^{34,1}_{ff,qq}$	$(\tilde{1}^q, 2^Q, \widetilde{34}^{\bar{q}}; a^g, b^Q)$

Table 4.5 Dipole factors for $gg \to q\bar{q}Q\bar{Q}H$ processes.

	Real kinematics	$(1^q, 2^Q, 3^{\bar{q}}, 4^{\bar{Q}}; a^g, b^g)$
i	Dipole factor	Born kinematics
1	$\mathcal{D}_2^{b4} = T_F\vert\mathcal{M}_B^{gQ}\vert^2\mathcal{D}^{b4,2}_{if,qg}$	$(1^q, \tilde{2}^Q, 3^{\bar{q}}; a^g, \widetilde{b4}^Q)$
2	$\mathcal{D}_4^{b2} = T_F\vert\mathcal{M}_B^{g\bar{Q}}\vert^2\mathcal{D}^{b2,4}_{if,qg}$	$(1^q, 3^{\bar{q}}, \tilde{4}^{\bar{Q}}; a^g, \widetilde{b2}^{\bar{Q}})$
3	$\mathcal{D}_1^{a3} = T_F\vert\mathcal{M}_B^{qg}\vert^2\mathcal{D}^{a3,1}_{if,qg}$	$(\tilde{1}^q, 2^Q, 4^{\bar{Q}}; \widetilde{a3}^q, b^g)$
4	$\mathcal{D}_3^{a1} = T_F\vert\mathcal{M}_B^{\bar{q}g}\vert^2\mathcal{D}^{a1,3}_{if,qg}$	$(2^Q, \tilde{3}^{\bar{q}}, 4^{\bar{Q}}; \widetilde{a1}^{\bar{q}}, b^g)$

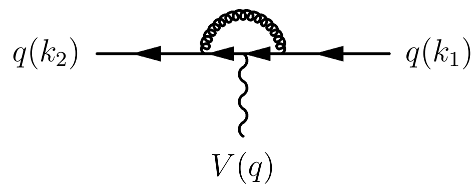

Figure 4.5 QCD correction to the qqV vertex

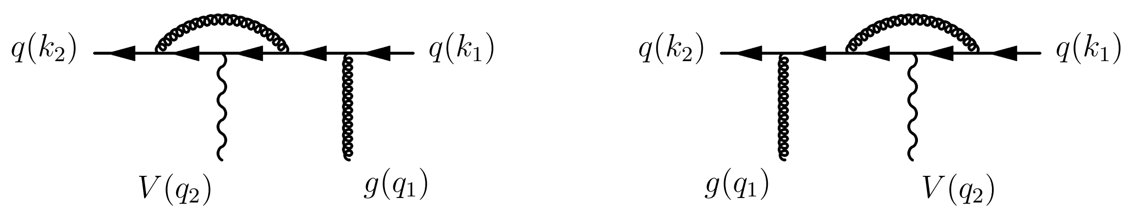

Figure 4.6 qqV vertex corrections for $q\bar{q} \to Vg$.

4.3.2 One-loop virtual corrections

Conventional dimensional regularization is used for computing the virtual corrections. The Passarino-Veltman reduction is performed in $d = 4 - 2\epsilon$ space-time dimensions [49]. The virtual corrections are split into two classes: the virtual corrections along the quark line with one weak boson attached and the virtual corrections with a weak boson and a gluon attached. Out of these two classes, the virtual corrections to $Hjjj$ production via vector boson fusion can be computed.

4.3.2.1 Boxline and Triangle Corrections

The first class of virtual corrections are QCD corrections to qqV vertices which were computed in Ref.[10]. The amplitude for Born-level process, $q(k_1) \to q(k_2) + V(q)$, is denoted by $\mathcal{M}_B(k_1, k_2; q)$. $q = k_1 - k_2$ is the four-momentum of the virtual weak boson V of virtuality $Q^2 = -q^2$. The virtual amplitude in conventional dimensional regularization $\mathcal{M}_V(k_1, k_2; q)$, depicted in Figure 4.5, is given by

$$\mathcal{M}_V(k_1, k_2; q) = \mathcal{M}_B(k_1, k_2; q) C_F \frac{\alpha_s(\mu_R)}{4\pi} \left(\frac{4\pi\mu_R^2}{-q^2}\right)^\epsilon \Gamma[1+\epsilon] \left(-\frac{2}{\epsilon^2} - \frac{3}{\epsilon} + c_{\text{virt}}\right) \quad [4.44]$$

with $c_{\text{virt}} = \pi^2/3 - 8$.

Figure 4.7 Propagator corrections for $q\bar{q} \to Vg$.

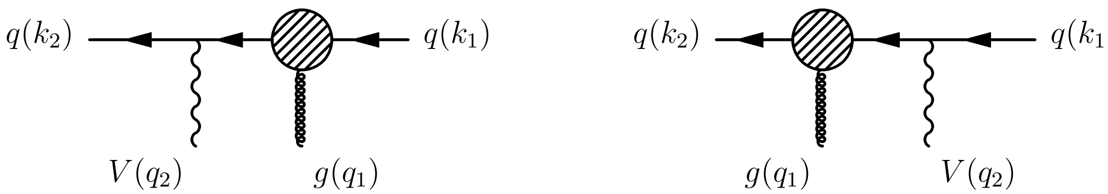

Figure 4.8 qqg vertex corrections for $q\bar{q} \to Vg$.

The second class of diagrams are the virtual QCD corrections to the Feynman graphs where a gluon g and an electroweak boson V (outgoing momenta q_1 and q_2) are attached to the same fermion line. Feynman graphs are shown by Figures 4.7, 4.8, and 4.10. The kinematics used here is for the process

$$q(k_1) \to q(k_2) + g(q_1) + V(q_2), \qquad [4.45]$$

where $k_1^2 = k_2^2 = 0$ and momentum conservation reads $k_1 = k_2 + q_2 + q_1$. As in [40], it is convenient to use the Mandelstam variables for a $2 \to 2$ process which is taken to be $\bar{q}q \to gV$. The Mandelstam variables are defined to be

$$\begin{aligned} s &= (k_1 - k_2)^2 = (q_1 + q_2)^2, \\ t &= (k_1 - q_1)^2 = (k_2 + q_2)^2, \\ u &= (k_1 - q_2)^2 = (k_2 + q_1)^2. \end{aligned} \qquad [4.46]$$

The gluon polarization denoted by $\epsilon_1(q_1)$ is transverse, i.e., $\epsilon_1 \cdot q_1 = 0$. The electroweak boson V is always virtual in the calculation. The effective polarization vector for the vector boson $\epsilon_2(q_2)$ corresponds to a fermion current. Due to the emission of the Higgs boson off the t-channel vector boson propagator, the fermion current is not conserved. Hence, terms with $\epsilon_2 \cdot q_2$ must be

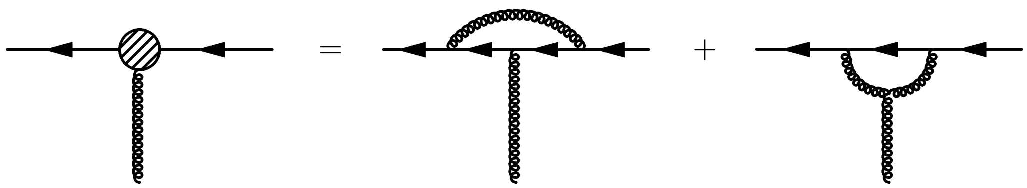

Figure 4.9 1-loop QCD corrections to the qqg vertex.

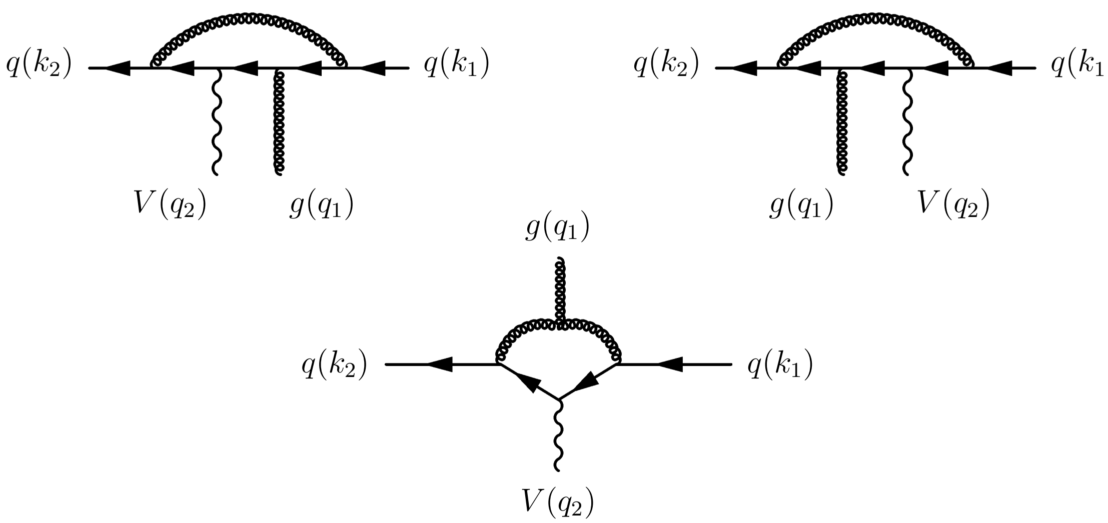

Figure 4.10 Box diagrams for $q\bar{q} \to Vg$.

kept throughout the calculation. Electroweak gauge invariance of the amplitude is preserved, i.e., $\mathcal{M}_\mu q_2^\mu = 0$.

The Born amplitude for $q\bar{q} \to gV$ is

$$\begin{aligned} \mathcal{M}_B(k_1 i_1 \tau_1, k_2 i_2 \tau_2, q_1 a, q_2; \epsilon_1, \epsilon_2) &= \delta_{\tau_2,\tau}\delta_{\tau_1,\tau} t^a_{i_2 i_1}(-e) g_\tau^{V f_2 f_1} g_s \bar{u}(k_2)[\gamma^\nu P_\tau \frac{(\not{k}_2 + \not{q}_2)}{t}\gamma^\mu \\ &+ \gamma^\mu \frac{(\not{k}_2 + \not{q}_1)}{u}\gamma^\nu P_\tau] u(k_1)\epsilon_{1\mu}\epsilon_{2\nu}. \end{aligned} \quad [4.47]$$

i_2 and i_1 are color indices for the quarks and a is the color index for the gluon. τ is the chirality index for the quark. $P_\tau = \frac{1}{2}(1 + \tau\gamma^5)$ is the chirality projector. $\epsilon_1 = \epsilon_1(q_1)$ and $\epsilon_2 = \epsilon_2(q_2)$ are polarization vectors for the gluon and vector boson, respectively.

The virtual amplitude is computed in $d = 4 - 2\epsilon$ space-time dimensions. The finite part

$$\tilde{\mathcal{M}}_V = \tilde{\mathcal{M}}_V(k_1 i_1 \tau_1, k_2 i_2 \tau_2, q_1 a, q_2; \epsilon_1, \epsilon_2)$$

can be written as

$$\begin{aligned} \tilde{\mathcal{M}}_V &= \delta_{\tau_2,\tau}\delta_{\tau_1,\tau} t^a_{i_2 i_1}\frac{\alpha_s}{4\pi}(-e) g_\tau^{V f_2 f_1} g_s \\ &\cdot \Big\{(C_F - \frac{1}{2}C_A)\{\tilde{\mathcal{M}}_\tau^{(1)}(k_2, q_1, q_2; \epsilon_1, \epsilon_2) + \tilde{\mathcal{M}}_\tau^{(2)}(k_2, q_1, q_2; \epsilon_1, \epsilon_2)\} \\ &\quad - \frac{1}{2}C_A \tilde{\mathcal{M}}_\tau^{(3)}(k_2, q_1, q_2; \epsilon_1, \epsilon_2)\Big\}, \end{aligned} \quad [4.48]$$

with

$$\begin{aligned} \tilde{\mathcal{M}}_\tau^{(1)}(k_2, q_1, q_2; \epsilon_1, \epsilon_2) &= \bar{\psi}(k_2)\{c_q^{(1)}(\not{q}_1 - \not{q}_2) + c_1^{(1)}\not{\epsilon}_1 \\ &+ c_2^{(1)}\not{\epsilon}_2 + c_b^{(1)}\not{\epsilon}_2(\not{k}_2 + \not{q}_2)\not{\epsilon}_1\} P_\tau \psi(k_1), \end{aligned} \quad [4.49]$$

$$\begin{aligned} \tilde{\mathcal{M}}_\tau^{(2)}(k_2, q_1, q_2; \epsilon_1, \epsilon_2) &= \bar{\psi}(k_2)\{c_q^{(2)}(\not{q}_1 - \not{q}_2) + c_1^{(2)}\not{\epsilon}_1 \\ &+ c_2^{(2)}\not{\epsilon}_2 + c_b^{(2)}\not{\epsilon}_1(\not{k}_2 + \not{q}_1)\not{\epsilon}_2\} P_\tau \psi(k_1), \end{aligned} \quad [4.50]$$

and

$$\begin{aligned} \tilde{\mathcal{M}}_\tau^{(3)}(k_2, q_1, q_2; \epsilon_1, \epsilon_2) &= \bar{\psi}(k_2)\{c_q^{(3)}(\not{q}_1 - \not{q}_2) + c_1^{(3)}\not{\epsilon}_1 + c_2^{(3)}\not{\epsilon}_2 \\ &+ c_b^{(3)}(\not{\epsilon}_1(\not{k}_2 + \not{q}_1)\not{\epsilon}_2 + \not{\epsilon}_2(\not{k}_2 + \not{q}_2)\not{\epsilon}_1\} P_\tau \psi(k_1). \end{aligned} \quad [4.51]$$

$\psi(\bar{k}_2)$ and $\psi(k_1)$ are quark spinors. The slashed symbols, $\not{q} = \gamma^\mu q_\mu$, are four-vectors contracted with gamma matrices. The coefficients $c_q^{(i)}$, $c_1^{(i)}$, $c_2^{(i)}$, and $c_b^{(i)}$ for $i = 1, 2, 3$ are given in terms of Passarino-Veltman D_{ij} functions in Appendix B.

The virtual amplitude $\mathcal{M}_V = \mathcal{M}_V(k_1 i_1 \tau_1, k_2 i_2 \tau_2, q_1 a, q_2; \epsilon_1, \epsilon_2)$ for $q(k_1) \to q(k_2) + g(q_1) + V(q_2)$ is

$$\begin{aligned}\mathcal{M}_V = \mathcal{M}_B \frac{\alpha_s}{4\pi}\Gamma[1+\epsilon]\Bigg\{&\frac{1}{2}\left(\left(\frac{4\pi\mu^2}{-u}\right)^\epsilon + \left(\frac{4\pi\mu^2}{-t}\right)^\epsilon\right)(-\frac{C_A}{\epsilon^2} - \gamma_g\frac{1}{\epsilon}) \\ &+\frac{1}{2}\frac{C_A}{C_F}\left(\left(\frac{4\pi\mu^2}{-u}\right)^\epsilon + \left(\frac{4\pi\mu^2}{-t}\right)^\epsilon - 2\left(\frac{4\pi\mu^2}{-s}\right)^\epsilon\right)(-\frac{C_F}{\epsilon^2} - \gamma_q\frac{1}{\epsilon}) \\ &+2\left(\frac{4\pi\mu^2}{-s}\right)^\epsilon(-\frac{C_F}{\epsilon^2} - \gamma_q\frac{1}{\epsilon}) + F(s,t,u) + C_F c_{\text{virt}}\Bigg\} + \tilde{\mathcal{M}}_V \end{aligned} \qquad [4.52]$$

where

$$\begin{aligned}F(s,t,u) = &\frac{C_A}{2}\left(\ln^2\left(\frac{-u}{\mu^2}\right) + \ln^2\left(\frac{-t}{\mu^2}\right)\right) - \frac{1}{2}(C_A - 2C_F)\ln^2\left(\frac{-s}{\mu^2}\right) \\ &+\frac{3}{2}(C_A - 2C_F)\ln\left(\frac{-s}{\mu^2}\right) + (\frac{1}{3}T_R N_f - \frac{5}{3}C_A)\left(\ln\left(\frac{-u}{\mu^2}\right) + \ln\left(\frac{-t}{\mu^2}\right)\right).\end{aligned} \qquad [4.53]$$

The constants γ_q, γ_g, and c_{virt} are

$$\gamma_q = \frac{3}{2}C_F, \quad \gamma_g = \frac{11}{6}C_A - \frac{2}{3}T_R N_f, \qquad [4.54]$$

$$c_{\text{virt}} = \frac{\pi^2}{3} - 8. \qquad [4.55]$$

Results for physical kinematic regions can be obtained by analytically continuing Eq.(4.52). For example if the invariant u is time-like, then one would perform the following replacement in Eqs.(4.52,4.53)

$$u \to u + i0^+. \qquad [4.56]$$

The natural logarithm for $u > 0$ is then

$$\ln(-u) = \ln(u) - i\pi. \qquad [4.57]$$

The $i\pi$ factors which result from analytic continuation vanish upon squaring the sum of the Born amplitude and the virtual amplitude. The analytic continuation for any double logarithms is dealt with automatically by Fortran code for the finite part of the virtual amplitude $\tilde{\mathcal{M}}_V$ in Eq.(4.52). The above results can then be used for any momentum configuration.

4.3.2.2 Hexagons and Pentagons

The third class of Feynman graphs are one-loop topologies for which a gluon propagates between the upper and lower quark lines. The hexagon diagrams are shown in Figure 4.11. The pentagon graphs which are needed to preserve gauge invariance are not shown, but would be included in any calculations involving the hexagon graphs. The hexagon and pentagon graphs form two gauge invariant sets. Here the virtual amplitude will be denoted as $\mathcal{M}_{V,\mathrm{hex}}$. It will be understood that $\mathcal{M}_{V,\mathrm{hex}}$ includes the contributions of any pentagon graphs. The hexagon amplitude can be deposed into

$$\mathcal{M}^{qQ}_{\mathrm{hex}} = t^a_{i_2 j} t^b_{j i_1} t^b_{i_4 i_3} \mathcal{M}^{qQ}_{\mathrm{hex},21} + t^a_{i_4 j} t^b_{j i_3} t^b_{i_2 i_1} \mathcal{M}^{qQ}_{\mathrm{hex},43} \qquad [4.58]$$

where $\mathcal{M}_{\mathrm{hex},21}$ and $\mathcal{M}_{\mathrm{hex},43}$ denote hexagon graphs with gluon emission off the 21 quark line and 43 quark line, respectively. The interference of the hexagon amplitude with the Born amplitude $\mathcal{M}^{qQ}_B$ leads to the expression

$$2\,\mathrm{Re}[\mathcal{M}^{qQ}_B (\mathcal{M}^{qQ}_{\mathrm{hex}})^*] = \frac{C_F^2}{d_G} \left\{ 2\,\mathrm{Re}[\mathcal{M}^{qQ}_{B,21} (\mathcal{M}^{qQ}_{\mathrm{hex},43})^*] + 2\,\mathrm{Re}[\mathcal{M}^{qQ}_{B,43} (\mathcal{M}^{qQ}_{\mathrm{hex},21})^*] \right\}. \qquad [4.59]$$

From the expression above it is evident that the QCD corrections resulting from the hexagons are suppressed by a factor $1/d_G = 1/(N^2-1) = 1/8$ relative to QCD corrections to a single quark current. The interference of the hexagons with the Born sub-amplitudes leads to soft singularities, $1/\epsilon$ poles, which are canceled against the integrated dipoles listed in Table 4.2. The divergent piece to $2\,\mathrm{Re}[\mathcal{M}^{qQ}_B (\mathcal{M}^{qQ}_{\mathrm{hex}})^*]$ is proportional to $2\,\mathrm{Re}[\mathcal{M}_{B,21} \mathcal{M}^*_{B,43}]$. As discussed in Subsection 4.3.1, these contributions are suppressed kinematically. Hence, the hexagon and pentagon graphs will be neglected.

4.3.3 Regularization of Divergences

Here the subprocess $q(p_a) + Q(p_b) \to q(p_1) + Q(p_2) + g(p_3) + H(P)$ is considered. Only the virtual corrections to a single quark current is considered since the contribution of pentagon and hexagon graphs is to be neglected. The virtual corrections needed here are exactly those of Subsection 4.3.2. The virtual corrections can be written as $\mathcal{M}_V = t^{c_3}_{i_1 i_a} \delta_{i_2 i_b} \mathcal{M}_{V,1a} + t^{c_3}_{i_2 i_b} \delta_{i_1 i_a} \mathcal{M}_{V,2b}$.

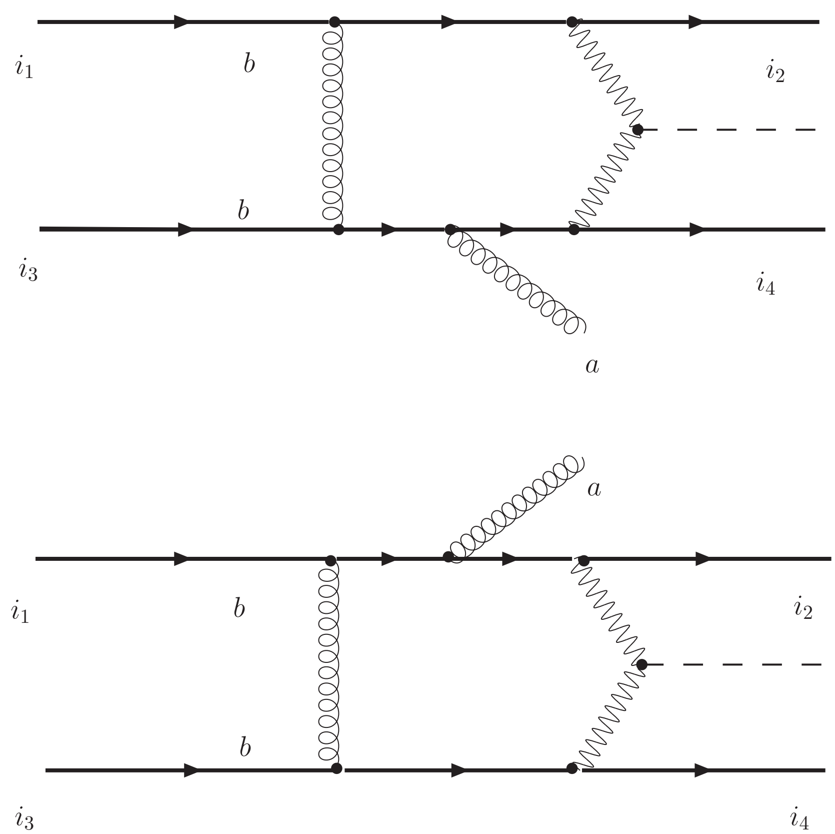

Figure 4.11 Hexagon diagrams

Recall, the Born amplitude takes the form, $\mathcal{M}_B = t^{c3}_{i_1 i_a}\delta_{i_2 i_b}\mathcal{M}_{B,1a} + t^{c3}_{i_2 i_b}\delta_{i_1 i_a}\mathcal{M}_{B,2b}$. The virtual corrections can be decomposed into a divergent part and a finite part, $\mathcal{M}_{V,1a} = \mathcal{M}_{V,1a}|_{div} + \tilde{\mathcal{M}}_{V,1a}$. $\mathcal{M}_{V,1a}|_{div}$ denotes the divergent part of the virtual amplitude and $\tilde{\mathcal{M}}_{V,1a}$ denotes the finite part of the virtual amplitude. Dot products of four-momentum vectors are written as $s_{ij} = 2p_i \cdot p_j$ for $j = a, b, 1, 2,$ or 3. Below the $\Gamma(1+\epsilon)$ in Eq. 4.52 is replaced by $\frac{1}{\Gamma(1-\epsilon)}$. The interference of the Born amplitude and the virtual amplitude is

$$\begin{aligned}
2\,\mathrm{Re}[\mathcal{M}_V^*\mathcal{M}_B] &= C_F|\mathcal{M}^{qQ}_{B,2b}(p_1,p_2,p_3;p_a,p_b)|^2\frac{\alpha_s(\mu^2)}{2\pi}\frac{1}{\Gamma(1-\epsilon)} \qquad [4.60]\\
&\cdot \Bigg\{\frac{1}{2}\left(\left(\frac{4\pi\mu^2}{s_{23}}\right)^\epsilon + \left(\frac{4\pi\mu^2}{s_{b3}}\right)^\epsilon\right)(-\frac{C_A}{\epsilon^2} - \gamma_g\frac{1}{\epsilon})\\
&+ \frac{1}{2}\frac{C_A}{C_F}\left(\left(\frac{4\pi\mu^2}{s_{23}}\right)^\epsilon + \left(\frac{4\pi\mu^2}{s_{b3}}\right)^\epsilon - 2\left(\frac{4\pi\mu^2}{s_{b2}}\right)^\epsilon\right)(-\frac{C_F}{\epsilon^2} - \gamma_q\frac{1}{\epsilon})\\
&+ 2\left(\left(\frac{4\pi\mu^2}{s_{b2}}\right)^\epsilon + \left(\frac{4\pi\mu^2}{s_{a1}}\right)^\epsilon\right)(-\frac{C_F}{\epsilon^2} - \gamma_q\frac{1}{\epsilon})\\
&- \frac{\pi^2}{6}(C_A + 4C_F) + 2C_F c_{\mathrm{virt}} + F(s_{b2}, s_{b3}, s_{23})\Bigg\}\\
&+ C_F|\mathcal{M}^{qQ}_{B,1a}(p_1,p_2,p_3;p_a,p_b)|^2\frac{\alpha_s(\mu^2)}{2\pi}\frac{1}{\Gamma(1-\epsilon)} \qquad [4.61]\\
&\cdot \Bigg\{\frac{1}{2}\left(\left(\frac{4\pi\mu^2}{s_{13}}\right)^\epsilon + \left(\frac{4\pi\mu^2}{s_{a3}}\right)^\epsilon\right)(-\frac{C_A}{\epsilon^2} - \gamma_g\frac{1}{\epsilon})\\
&+ \frac{1}{2}\frac{C_A}{C_F}\left(\left(\frac{4\pi\mu^2}{s_{13}}\right)^\epsilon + \left(\frac{4\pi\mu^2}{s_{a3}}\right)^\epsilon - 2\left(\frac{4\pi\mu^2}{s_{a1}}\right)^\epsilon\right)(-\frac{C_F}{\epsilon^2} - \gamma_q\frac{1}{\epsilon})\\
&+ 2\left(\left(\frac{4\pi\mu^2}{s_{a1}}\right)^\epsilon + \left(\frac{4\pi\mu^2}{s_{b2}}\right)^\epsilon\right)(-\frac{C_F}{\epsilon^2} - \gamma_q\frac{1}{\epsilon})\\
&- \frac{\pi^2}{6}(C_A + 4C_F) + 2C_F c_{\mathrm{virt}} + F(s_{a1}, s_{a3}, s_{13})\Bigg\}\\
&+ C_F(2\,\mathrm{Re}[\mathcal{M}^{qQ}_{B,1a}(\tilde{\mathcal{M}}^{qQ}_{V,1a})^*] + 2\,\mathrm{Re}[\mathcal{M}^{qQ}_{B,2b}(\tilde{\mathcal{M}}^{qQ}_{V,2b})^*]).
\end{aligned}$$

$\tilde{\mathcal{M}}_{V,1a}$ is the finite contribution due to virtual corrections on the $1a$ quark line. Likewise, $\tilde{\mathcal{M}}_{V,2b}$ is the finite contribution due to virtual corrections on the $2b$ quark line. The precise form of these finite contributions are given in Appendix B.

Using the Catani-Seymour dipole subtraction method [21], the resulting insertion operator $<\mathbf{I}(\epsilon)>$ is given by

$$
\begin{aligned}
<\mathbf{I}(\epsilon)> \;=\;& C_F|\mathcal{M}^{qQ}_{B,2b}(p_1,p_2,p_3;p_a,p_b)|^2\frac{\alpha_s(\mu^2)}{2\pi}\frac{1}{\Gamma(1-\epsilon)} && [4.62]\\
\cdot\;& \left\{\frac{1}{2}\left(\left(\frac{4\pi\mu^2}{s_{23}}\right)^{\epsilon}+\left(\frac{4\pi\mu^2}{s_{b3}}\right)^{\epsilon}\right)\mathcal{V}_g(\epsilon)\right.\\
+\;& \frac{1}{2}\frac{C_A}{C_F}\left(\left(\frac{4\pi\mu^2}{s_{23}}\right)^{\epsilon}+\left(\frac{4\pi\mu^2}{s_{b3}}\right)^{\epsilon}-2\left(\frac{4\pi\mu^2}{s_{b2}}\right)^{\epsilon}\right)\mathcal{V}_q(\epsilon)\\
+\;& \left.2\left(\left(\frac{4\pi\mu^2}{s_{b2}}\right)^{\epsilon}+\left(\frac{4\pi\mu^2}{s_{a1}}\right)^{\epsilon}\right)\mathcal{V}_q(\epsilon)\right\}\\
+\;& C_F|\mathcal{M}^{qQ}_{B,1a}(p_1,p_2,p_3;p_a,p_b)|^2\frac{\alpha_s(\mu^2)}{2\pi}\frac{1}{\Gamma(1-\epsilon)} && [4.63]\\
\cdot\;& \left\{\frac{1}{2}\left(\left(\frac{4\pi\mu^2}{s_{13}}\right)^{\epsilon}+\left(\frac{4\pi\mu^2}{s_{a3}}\right)^{\epsilon}\right)\mathcal{V}_g(\epsilon)\right.\\
+\;& \frac{1}{2}\frac{C_A}{C_F}\left(\left(\frac{4\pi\mu^2}{s_{13}}\right)^{\epsilon}+\left(\frac{4\pi\mu^2}{s_{a3}}\right)^{\epsilon}-2\left(\frac{4\pi\mu^2}{s_{a1}}\right)^{\epsilon}\right)\mathcal{V}_q(\epsilon)\\
+\;& \left.2\left(\left(\frac{4\pi\mu^2}{s_{a1}}\right)^{\epsilon}+\left(\frac{4\pi\mu^2}{s_{b2}}\right)^{\epsilon}\right)\mathcal{V}_q(\epsilon)\right\},
\end{aligned}
$$

where

$$\mathcal{V}_q(\epsilon)=C_F\left(\frac{1}{\epsilon^2}-\frac{\pi^2}{3}\right)+\gamma_q\frac{1}{\epsilon}+\gamma_q+K_q+\mathcal{O}(\epsilon), \qquad [4.64]$$

and

$$\mathcal{V}_g(\epsilon)=C_A\left(\frac{1}{\epsilon^2}-\frac{\pi^2}{3}\right)+\gamma_g\frac{1}{\epsilon}+\gamma_g+K_g+\mathcal{O}(\epsilon). \qquad [4.65]$$

The constants, γ_q and γ_g are

$$\gamma_q=\frac{3}{2}C_F, \quad \gamma_g=\frac{11}{6}C_A-\frac{2}{3}T_RN_f, \qquad [4.66]$$

and the constants, K_q and K_g, are

$$K_q=\left(\frac{7}{2}-\frac{\pi^2}{6}\right)C_F, \quad K_g=\left(\frac{67}{18}-\frac{\pi^2}{6}\right)C_A-\frac{10}{9}T_RN_f. \qquad [4.67]$$

Combining Eq.(4.60) and Eq.(4.62) yields

$$\begin{aligned} 2\,\mathrm{Re}[\mathcal{M}_V^*\mathcal{M}_B] + <\mathbf{I}(\epsilon)> &= |\mathcal{M}_B^{qQ}(p_1,p_2,p_3;p_a,p_b)|^2\frac{\alpha_s(\mu^2)}{2\pi}K_{\rm born} \\ &+ |\mathcal{M}_{B,1a}^{qQ}(p_1,p_2,p_3;p_a,p_b)|^2\frac{\alpha_s(\mu^2)C_F}{2\pi}F(s_{a1},s_{a3},s_{13}) \\ &+ |\mathcal{M}_{B,2b}^{qQ}(p_1,p_2,p_3;p_a,p_b)|^2\frac{\alpha_s(\mu^2)C_F}{2\pi}F(s_{b2},s_{b3},s_{23}) \\ &+ C_F(2\,\mathrm{Re}[\mathcal{M}_{B,1a}^{qQ}(\tilde{\mathcal{M}}_{V,1a}^{qQ})^*] + 2\,\mathrm{Re}[\mathcal{M}_{B,2b}^{qQ}(\tilde{\mathcal{M}}_{V,2b}^{qQ})^*]) \end{aligned} \quad [4.68]$$

The constant, $K_{\rm born}$, is

$$K_{\rm born} = \left(-\frac{2\pi^2}{3}+\frac{50}{9}\right)C_A - \frac{16}{9}T_RN_f + 2C_F\left(-\frac{4\pi^2}{3}+10+c_{\rm virt}\right). \quad [4.69]$$

Given Eq.(4.68), one obtains the finite three-parton NLO cross section for $qQ \to qQH$ processes

$$\begin{aligned} \sigma_3^{NLO}(qQ\to qQgH) &= \int_0^1 dx_a \int_0^1 dx_b f_{q/p}(x_a,\mu_F) f_{Q/p}(x_b,\mu_F) \\ &\times \frac{1}{2\hat{s}} d\Phi(p_1,p_2,p_3,P;p_a,p_b) F_J^{(3)}(p_1,p_2,p_3,P;p_a,p_b) \\ &\cdot \left\{ |\mathcal{M}_B^{qQ}(p_1,p_2,p_3;p_a,p_b)|^2 \left(1+\frac{\alpha_s(\mu^2)}{2\pi}K_{\rm born}\right)\right. \\ &+ |\mathcal{M}_{B,1a}^{qQ}(p_1,p_2,p_3;p_a,p_b)|^2\frac{\alpha_s(\mu^2)C_F}{2\pi}F(s_{a1},s_{a3},s_{13}) \\ &+ |\mathcal{M}_{B,2b}^{qQ}(p_1,p_2,p_3;p_a,p_b)|^2\frac{\alpha_s(\mu^2)C_F}{2\pi}F(s_{b2},s_{b3},s_{23}) \\ &+ \left. C_F(2\,\mathrm{Re}[\mathcal{M}_{B,1a}^{qQ}(\tilde{\mathcal{M}}_{V,1a}^{qQ})^*] + 2\,\mathrm{Re}[\mathcal{M}_{B,2b}^{qQ}(\tilde{\mathcal{M}}_{V,2b}^{qQ})^*])\right\} \end{aligned} \quad [4.70]$$

The virtual amplitude for the gluon initiated process

$$g(p_a) + Q(p_b) \to q(p_1) + \bar{q}(p_3) + Q(p_2) + H(P), \quad [4.71]$$

is represented by $\mathcal{M}_V^{gQ} = \mathcal{M}_V^{gQ}(p_1,p_2,p_3,P;p_a,p_b)$. Since, only vector-boson fusion processes are considered here annihilation graphs are neglected. The sum of $2\,\mathrm{Re}[(\mathcal{M}_V^{gQ})^*\mathcal{M}_B^{gQ}]$ and $<\mathbf{I}>$ for the gluon-initiated process leads to the following three parton NLO cross section contribution

$$\sigma_3^{NLO}(gQ\to q\bar{q}QH) = \int_0^1 dx_a \int_0^1 dx_b f_{g/p}(x_a,\mu_F) f_{Q/p}(x_b,\mu_F) \quad [4.72]$$

$$
\begin{aligned}
&\times \quad \frac{1}{2\hat{s}} d\Phi(p_1,p_2,p_3,P;p_a,p_b) F_J^{(3)}(p_1,p_2,p_3,P;p_a,p_b) \\
&\cdot \quad \left\{ |\mathcal{M}_B^{gQ}(p_1,p_2,p_3;p_a,p_b)|^2 \left(1 + \frac{\alpha_s(\mu^2)}{2\pi} (K_{\text{born}} + F(s_{13},s_{a3},s_{a1}) \right) \right. \\
&+ \quad \left. \frac{C_F d_F}{d_G} 2\,\mathrm{Re}[(\tilde{\mathcal{M}}_V^{gQ})^* \mathcal{M}_B^{gQ}] \right\}.
\end{aligned}
$$

There is also a similar expression for the process $Qg \to q\bar{q}QH$.

4.3.4 Finite collinear terms

In this Subsection, formulae for the finite collinear cross section are given. The formulae below can be derived from Eq.(A.77) by first writing down the various contributions $\int_0^1 dx \hat{\sigma}_{ab}^{NLO\{4\}}$ where $ab = qQ, gg, gQ, qg$. Then, the terms in $\int_0^1 dx \hat{\sigma}_{ab}^{NLO}$ are convoluted with the parton distribution functions. The result can then be collected into pieces proportional to the Born matrix elements squares, $|\mathcal{M}_B^{qQ}|^2$ and $|\mathcal{M}_B^{gQ}|^2$.

For the gluon initiated Born-level process, $gQ \to q\bar{q}QH$, the finite collinear contribution is

$$
\begin{aligned}
\sigma_{3,\text{col}}^{NLO}(gQ \to q\bar{q}QH) &= \int_0^1 dx_a \int_0^1 dx_b \left\{ f_{g/p}(x_a;\mu_F) f_{Q/p}(x_b;\mu_F,\mu_R) \right. \\
&+ \left. \frac{1}{2} \left(f_{g/p}^{1,a}(x_a;\mu_F,\mu_R) + f_{g/p}^{3,a}(x_a;\mu_F,\mu_R) \right) f_{Q/p}(x_b;\mu_F) \right\} \\
&\cdot \frac{1}{2\hat{s}} d\Phi(p_1,p_2,p_3,P;p_a+p_b) |\mathcal{M}_B^{gQ}|^2 F_J^{(3)}(p_1,p_2,p_3;p_a,p_b)
\end{aligned} \tag{4.73}
$$

with

$$
f_{g/p}^{1,a}(x_a;\mu_F,\mu_R) = \sum_q (f_{qg;q/p}^{1,a}(x_a;\mu_F,\mu_R) + f_{qg;\bar{q}/p}^{1,a}(x_a;\mu_F,\mu_R)) + f_{gg;g/p}^{1,a}(x_a;\mu_F,\mu_R) \tag{4.74}
$$

and,

$$
f_{Q/p}^{2,b}(x_b;\mu_F,\mu_R) = f_{gq;g/p}^{2,b}(x_b;\mu_F,\mu_R) + f_{qq;Q/p}^{2,b}(x_b;\mu_F,\mu_R). \tag{4.75}
$$

For the Born-level process, $qQ \to qQgH$, the finite collinear contribution is:

$$
\begin{aligned}
\sigma_{3,\text{col}}^{NLO}(qQ \to qQgH) &= \int_0^1 dx_a \int_0^1 dx_b \frac{1}{2\hat{s}} d\Phi(p_1,p_2,p_3,P;p_a+p_b) F_J^{(3)}(p_1,p_2,p_3;p_a,p_b) \\
&\cdot \{ (f_{q/p}(x_a,\mu_F) f_{Q/p}^{2,b}(x_b,\mu_F,\mu_R) + f_{q/p}^{1,a}(x_a;\mu_F,\mu_R)) |\mathcal{M}_B^{qQ}|^2 \\
&+ \frac{1}{2} C_A f_{q/p}(x_a;\mu_F) (f_{Q/p}^{3,b}(x_b;\mu_F,\mu_R) - f_{Q/p}^{2,b}(x_b;\mu_F,\mu_R)) |\mathcal{M}_{B,2b}^{qQ}|^2 \\
&+ \frac{1}{2} C_A (f_{q/p}^{3,b}(x_a;\mu_F,\mu_R) - f_{q/p}^{1,a}(x_a;\mu_F,\mu_R)) f_{Q/p}(x_b,\mu_F) |\mathcal{M}_{B,1a}^{qQ}|^2 \},
\end{aligned} \tag{4.76}
$$

with

$$f^{1,a}_{q/p}(x_a;\mu_F,\mu_R) = f^{1,a}_{qq;q/p}(x_a;\mu_F,\mu_R) + f^{1,a}_{gq;g/p}(x_a;\mu_F,\mu_R). \qquad [4.77]$$

Using the above expressions the finite collinear terms can be computed as part of the 3-parton phase space integration. Listed below are the convoluted splitting functions, $f^{i,a}_{ab;a/p}(x_a;\mu_R,\mu_R)$. The kernels for the convoluted splitting functions are given by $A^{i,a}_{ab}(z)$, $B^{i,a}_{ab}(z)$, $C^{i,a}_{ab}(z)$, and $D^{i,a}_{ab}(x)$. The subscripts a and b represent the splitting of a parton a to parton b. The superscripts i and a are momentum labels for the momenta p_i and p_a. Using this notation allows one to write down general formulas for the convoluted splitting functions. The splitting functions P^{ab} and flavor kernels $\overline{K}^{ab}$ can be found in Appendix A.

The convoluted splitting function for the splitting $q \to q + g$ is

$$\begin{aligned} f^{i,a}_{qq;q/p}(x_a,\mu_F,\mu_R) &= \frac{\alpha_s(\mu_R)}{2\pi}\int_{x_a}^{1}\frac{dz}{z} f_{q/p}\left(\frac{x_a}{z},\mu_F\right) \\ &\cdot \left\{\overline{K}^{qq}(z) - \gamma_i\left[\left(\frac{1}{1-z}\right)_+ + \delta(1-z)\right] + P^{qq}(z)\ln\frac{2p_a p_i}{\mu_F^2}\right\} \\ &= \frac{\alpha_s(\mu_R)}{2\pi}\int_{x_a}^{1}\frac{dz}{z}\left\{\left[f_{q/p}\left(\frac{x_a}{z};\mu_F\right) - z f_{q/p}(x_a;\mu_F)\right]B^{i,a}_{qq}(z)\right. \qquad [4.78] \\ &+ \left. f_{q/p}\left(\frac{x_a}{z};\mu_F\right)C^{i,a}_{qq}(z)\right\} + \frac{\alpha_s(\mu_R)}{2\pi} f_{q/p}(x_a;\mu_F) D^{i,a}_{qq}(x_a), \end{aligned}$$

with kernels

$$B^{i,a}_{qq}(z) = C_F\left[\frac{2}{1-z}\ln\frac{2p_a p_i(1-z)}{\mu_F^2} - \frac{\gamma_i}{C_F}\frac{1}{1-z}\right], \qquad [4.79]$$

$$C^{i,a}_{qq}(z) = C_F\left[-(1+z)\ln\frac{2p_a p_i(1-z)}{\mu_F^2 z} - \frac{2}{1-z}\ln z + (1-z)\right], \qquad [4.80]$$

$$\begin{aligned} D^{i,a}_{qq}(x) &= C_F\left[\frac{2\pi^2}{3} - 5 - \frac{\gamma_i}{C_F} - \frac{\gamma_i}{C_F}\ln(1-x) + \ln^2(1-x)\right. \qquad [4.81] \\ &+ \left.\frac{3}{2}\ln\frac{2p_i p_a}{\mu_F^2} + 2\ln(1-x)\ln\frac{2p_i p_a}{\mu_F^2}\right]. \end{aligned}$$

For the splitting $q \to q + g$ the convoluted splitting function is

$$\begin{aligned} f^{i,a}_{qg;q/p}(x_a,\mu_F,\mu_R) &= \frac{\alpha_s(\mu_R)}{2\pi}\int_{x_a}^{1}\frac{dz}{z} f_{q/p}\left(\frac{x_a}{z},\mu_F\right)\left\{\overline{K}^{qg}(z) + P^{qg}(z)\ln\frac{2p_a p_i}{\mu_F^2}\right\} \qquad [4.82] \\ &= \frac{\alpha_s(\mu_R)}{2\pi}\int_{x_a}^{1}\frac{dz}{z} f_{q/p}\left(\frac{x_a}{z};\mu_F\right) A^{i,a}_{qg}(z), \end{aligned}$$

with kernel

$$A^{i,a}_{qg}(z) = C_F\left[\frac{1+(1-z)^2}{z}\ln\frac{2p_ap_i(1-z)}{\mu_F^2 z} + z\right]. \quad [4.83]$$

For $g \to q + \bar{q}$ splitting the convoluted splitting function is

$$\begin{aligned} f^{i,a}_{gq;g/p}(x_a,\mu_F,\mu_R) &= \frac{\alpha_s(\mu_R)}{2\pi}\int_{x_a}^1\frac{dz}{z}f_{g/p}\left(\frac{x_a}{z},\mu_F\right)\left\{\overline{K}^{gq}(z) + P^{gq}(z)\ln\frac{2p_ap_i}{\mu_F^2}\right\} \quad [4.84] \\ &= \frac{\alpha_s(\mu_R)}{2\pi}\int_{x_a}^1\frac{dz}{z}f_{g/p}\left(\frac{x_a}{z};\mu_F\right)A^{i,a}_{gq}(z), \end{aligned}$$

with kernel

$$A^{i,a}_{gq}(z) = T_F[z^2 + (1-z)^2]\ln\frac{2p_ap_i(1-z)}{\mu_F^2 z} + T_F 2z(1-z). \quad [4.85]$$

For the $g \to g + g$ splitting the convoluted splitting function is

$$\begin{aligned} f^{i,a}_{gg;g/p}(x_a,\mu_F,\mu_R) &= \frac{\alpha_s(\mu_R)}{2\pi}\int_{x_a}^1\frac{dz}{z}f_{g/p}\left(\frac{x_a}{z},\mu_F\right) \\ &\cdot \left\{\overline{K}^{gg}(z) - \frac{3}{2}C_A\left[\left(\frac{1}{1-z}\right)_+ + \delta(1-z)\right] + P^{gg}(z)\ln\frac{2p_ap_i}{\mu_F^2}\right\} \quad [4.86] \\ &= \frac{\alpha_s(\mu_R)}{2\pi}\int_{x_a}^1\frac{dz}{z}\left\{\left[f_{g/p}\left(\frac{x_a}{z};\mu_F\right) - zf_{g/p}(x_a;\mu_F)\right]B^{i,a}_{gg}(z)\right. \\ &+ \left. f_{g/p}\left(\frac{x_a}{z};\mu_F\right)C^{i,a}_{gg}(z)\right\} + \frac{\alpha_s(\mu_R)}{2\pi}f_{g/p}(x_a;\mu_F)D^{i,a}_{gg}(x_a), \end{aligned}$$

$$B^{i,a}_{gg}(z) = C_A\left[\frac{2}{1-z}\ln\frac{2p_ap_i(1-z)}{\mu_F^2} - \frac{3}{2}\frac{1}{1-z}\right], \quad [4.87]$$

$$C^{i,a}_{gg}(z) = C_A\left[\left(\frac{1-z}{z} - 1 + z(1-z)\right)\ln\frac{2p_ap_i(1-z)}{\mu_F^2 z} - \frac{2}{1-z}\ln z\right], \quad [4.88]$$

$$\begin{aligned} D^{i,a}_{gg}(x) &= 2C_A\ln(1-x)\ln\frac{2p_ap_i}{\mu_F^2} + \gamma_g\ln\frac{2p_ap_i}{\mu_F^2} \\ &+ C_A\left(\frac{2\pi^2}{3} - \frac{50}{9} + \ln^2(1-x)\right) \quad [4.89] \\ &+ \frac{16}{9}T_FN_f - \frac{3}{2}C_A - \frac{3}{2}C_A\ln(1-x). \end{aligned}$$

Here the initial state momenta p_a and p_b are

$$p_a = x_aP_a, \qquad p_b = x_bP_b \quad [4.90]$$

where x_a and x_b are the Feynman-x and P_a and P_b are the beam momentum. The constants γ_g and γ_q are given by Eq.(4.54).

4.4 Concluding Remarks

The cross section contributions discussed in the previous sections have been implemented in a parton-level Monte Carlo program. The Born amplitudes are calculated numerically using the helicity amplitude formalism of Ref.[30]. These amplitudes have been taken from Ref.[10]. While the Fortran code for the real emission amplitudes has been generated using MADGRAPH [48]. The Monte Carlo integration is performed with a modified version of VEGAS [31]. Gauge invariance has been checked numerically and analytically for the virtual amplitudes. The dipole subtraction method used here has been checked numerically in all regions of phase space for which there are collinear or soft singularities in the real emission graphs.

Chapter 5

Central Jet Veto Efficiency at NLO

5.1 Introduction

The observation of two forward tagging jets in Higgs production via VBF at the LHC is crucial for the suppression of backgrounds [17, 25, 26, 27, 28, 29]. In addition to forward jet tagging, the veto of any additional jet activity in the central region (*central jet veto*) also leads to suppression of QCD backgrounds such as W^+W^-jj , $t\bar{t}jj$, and gluon fusion Hjj production [27, 51]. This is caused by the t-channel exchange of quarks or gluons which tend to radiate more gluons. For VBF processes there is suppressed jet activity in the central region which is due to color singlet exchange in the t-channel. For the central jet veto (CJV) proposal, events are discarded if any additional jet with a transverse momentum above a cut $p_{T,veto}$ is found between the tagging jets [14, 15, 16, 17, 18, 19, 20]. Survival probabilities for the CJV have been calculated for the Higgs boson signal and background processes using LO matrix elements [15, 27]. However, for the VBF process $pp \to Hjjj$ the cross section suffers from scale variations on the order of 40%. Since survival probabilities depend on the 3-jet and 2-jet cross sections, any theoretical uncertainties of these cross sections will feed into the survival probabilities and in turn the uncertainty of coupling measurements at the LHC. The vector-boson fusion cuts used in simulations are described in Section 5.2. In Section 5.3 the scale dependence of the next-to-leading order (NLO) three jet cross section for Higgs production via VBF (VBF $Hjjj$) is discussed. In Section 5.4 3-jet ratios $R = d\sigma_3/d\sigma_2$ for Higgs production are computed to NLO accuracy using the VBF $Hjjj$ parton-level Monte Carlo program developed in Chapter 4 and the VBF Hjj parton-level Monte Carlo program developed in Chapter 2.

5.2 Vector-Boson Fusion Cuts

The Standard Model (SM) parameters used in all subsequent calculations are listed in Table 5.1. SM parameters are computed using LO electroweak relations. Cross sections are computed using CTEQ6M parton distributions [33] for all NLO results and CTEQ6L1 parton distributions for all leading order cross sections. The running of the strong coupling is evaluated at two-loop order, with $\alpha_s(M_Z) = 0.188$, for LO and NLO results. In order to reconstruct jets from the final-state partons, the k_T algorithm [34] as described in Ref.[35] is used, with resolution parameter $D = 0.8$.

Table 5.1 Standard Model input parameters

$\alpha_s^{NLO}(M_Z)$	$\alpha_s^{LO}(M_Z)$	M_Z	G_F	α_{QED}
0.118	0.130	91.188 GeV	1.16639×10^{-5}	$1/128.930$

The k_T algorithm is used to calculate the partonic cross sections for events with at least three hard jets, which are required to have

$$p_{Tj} \geq 20 \text{ GeV}\,, \qquad\qquad |y_j| \leq 4.5\,. \tag{5.1}$$

Here y_j denotes the rapidity of the (massive) jet momentum which is reconstructed as the four-vector sum of massless partons of pseudorapidity $|\eta| < 5$.

At LO, there are exactly three massless final state partons. The two hard jets are identified as tagging jets provided they pass the k_T algorithm and the cuts described above. At NLO these jets may be composed of two partons (recombination effect) or four well-separated partons may be encountered, which satisfy the cuts of Eq. 5.1 and would give rise to four-jet events. As with LHC data, a choice needs to be made for selecting the tagging jets in such a multijet situation. Here the "p_T-method" is chosen. For a given event, the tagging jets are defined as the two jets with the highest transverse momentum, p_{Tj}, with

$$p_{Tj}^{\text{tag}} \geq 30 \text{ GeV}, \qquad |y_j^{\text{tag}}| \leq 4.5. \tag{5.2}$$

The non-tagging jets by default here are jets of lowest transverse momenta but do not necessarily satisfy the cuts of Eq.(5.2) but satisfy the cuts of Eq.(5.1).

The Higgs boson decay products (generically called "leptons" in the following) are required to fall between the two tagging jets in rapidity and they should be well observable. While the exact definition of criteria for the Higgs decay products will depend on the channel considered, such specific requirements here are substituted by generating isotropic Higgs boson decay into two massless “leptons” (which represent $\tau^+\tau^-$ or $\gamma\gamma$ or $b\bar{b}$ final states) and require

$$p_{T\ell} \geq 20 \text{ GeV}\,, \qquad |\eta_\ell| \leq 2.5\,, \qquad \triangle R_{j\ell} \geq 0.6\,, \tag{5.3}$$

where $R_{j\ell}$ denotes the jet-lepton separation in the rapidity-azimuthal angle plane. In addition, the two ”leptons” are required to fall between the two tagging jets in rapidity:

$$y^{\text{tag}}_{j,min} < \eta_{\ell_{1,2}} < y^{\text{tag}}_{j,max}. \tag{5.4}$$

Note that no reduction due to branching ratios for specific final states is included in the calculation.

Backgrounds to vector-boson fusion are significantly suppressed by requiring a large rapidity separation for the two tagging jets. Tagging jets are required to reside in opposite detector hemispheres with

$$y_j^{\text{tag 1}} \cdot y_j^{\text{tag 2}} < 0. \tag{5.5}$$

with a ”rapidity gap cut” of

$$\Delta y_{jj} = |y_j^{\text{tag 1}} - y_j^{\text{tag 2}}| > 4. \tag{5.6}$$

QCD backgrounds for the Higgs signal typically occur at smaller invariant masses, due to the dominance of gluons at small Feynman x in the incoming protons [27]. The QCD backgrounds can be reduced by imposing a lower bound on the invariant mass of the tagging jets of

$$m_{jj} > 600 \text{ GeV}. \tag{5.7}$$

5.3 Scale dependence

The cross section for Higgs production via VBF in the association of three jets ($Hjjj$), within the cuts of Eqs.(5.1)-(5.7), is shown in Figure 5.1. The scale dependence of the NLO and LO cross section is shown for fixed factorization and renormalization scales, μ_F and μ_R, which are tied to the scale $\mu_0 = 40$ GeV,

$$\mu_R = \xi_R \mu_0, \qquad \mu_F = \xi_F \mu_0. \tag{5.8}$$

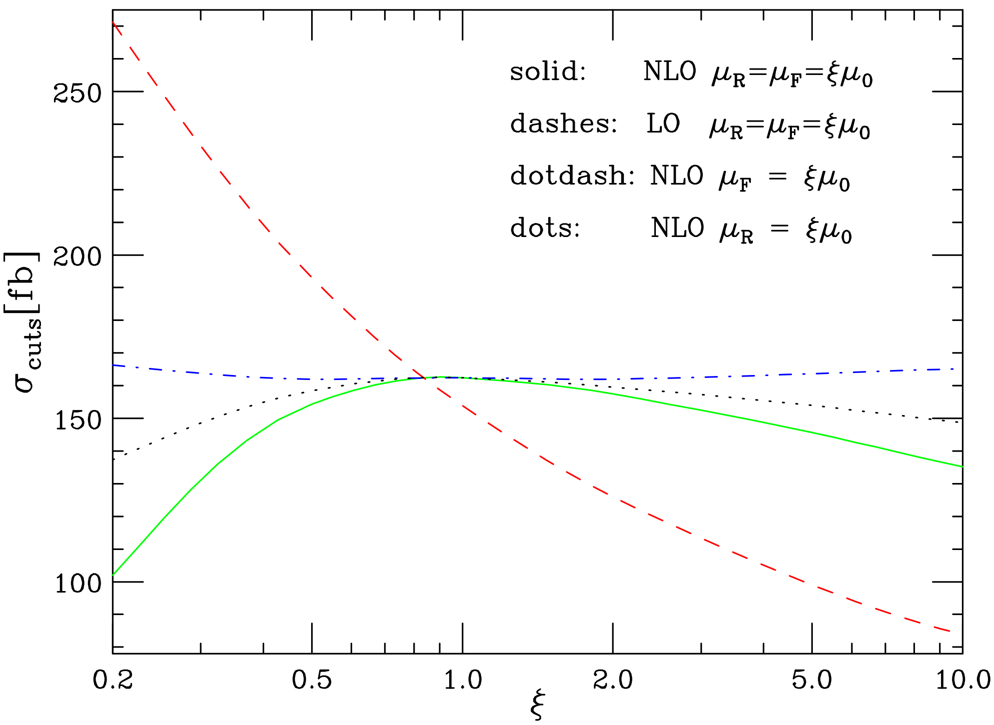

Figure 5.1 Scale dependence of the total cross section at LO and NLO within the cuts of Eqs. (5.1)- (5.7) for VBF $Hjjj$ at the LHC. The factorization scale μ_F and the renormalization scale μ_R have been taken as multiples, $\xi\mu_0$, of the scale $\mu_0 = 40$ GeV and ξ is varied in the range $0.2 < \xi < 10.0$. The NLO curves are for $\mu_R = \mu_F = \mu_0$ (solid line), $\mu_F = \mu_0$ and $\mu_R = \xi\mu_0$ (dotted line), and $\mu_F = \xi\mu_0$ and $\mu_R = \mu_0$ (dot-dashed line). The dashed curve shows the dependence of the LO cross section on the renormalization scale and factorization scale with $\mu_R = \mu_F = \xi\mu_0$.

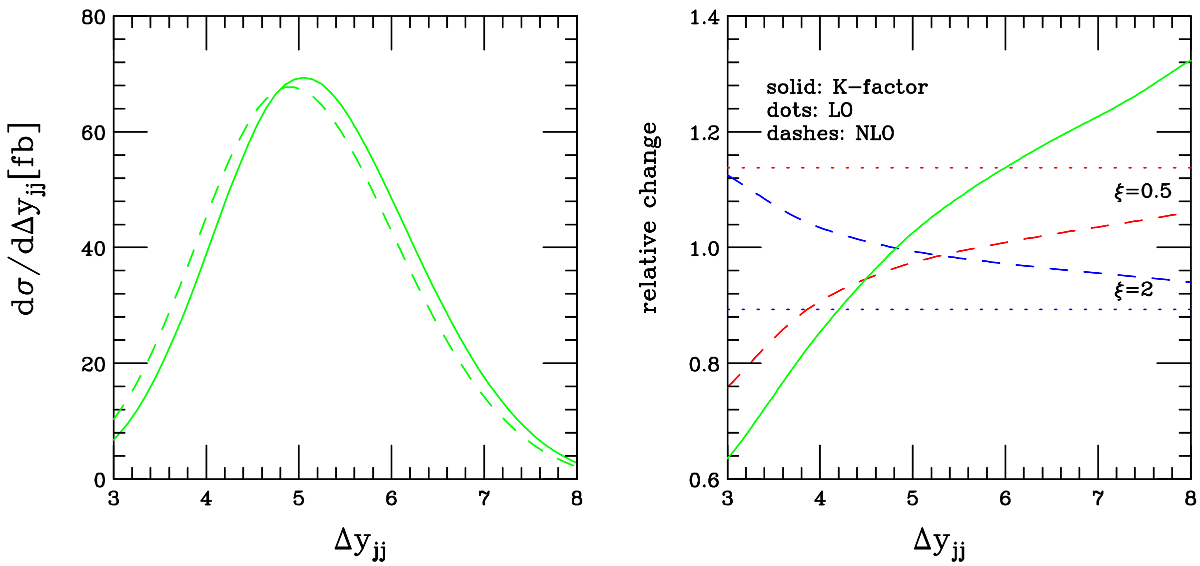

Figure 5.2 $Hjjj$ production with the cuts of Eqs.(5.1)-(5.5) and Eq.(5.7). In the left panel, $d\sigma/d\Delta y_{jj}$ (in fb) is shown at LO (dashed line) and NLO (solid line) for $\mu_F = \mu_R = 40$ GeV. In the right-hand panel the K factor (solid line) and scale variations of LO (dotted lines) and NLO (dashed lines) results are shown for $\mu_R = \xi\mu_0$ and $\mu_F = 40$ GeV with $\xi = 1/2$ and 2.

The LO cross section depends on both the factorization and renormalization scale. For $\mu_R = \mu_F = \xi\mu_0$ with $0.5 < \xi < 2$ the scale variation is $+25\%$ to -18% for the LO cross section. The LO $Hjjj$ production cross section is proportional to α_s. For Hjj production, recall, there was no such dependence at LO. At NLO three choices are shown: (a) $\xi_R = \xi_F = \xi$ (solid line); (b) $\xi_R = \xi$, $\xi_F = 1$ (dotted line); (c) $\xi_R = 1$, $\xi_F = \xi$ (dot-dashed line). Allowing for a factor 2 variation in either direction, i.e., considering the range $0.5 \le \xi \le 2$, the NLO cross section changes by less than 5% in all cases. K factors for $Hjjj$ production range from 1.03 to 1.06 for Higgs boson masses of $m_h = 120$ GeV to 200 GeV for $\xi_R = \xi_F = 1$.

The K factors shown in Figures 5.2 and 5.3 are defined by the formula,

$$K(x) = \frac{d\sigma_3^{NLO}(\mu_R = \mu_F = \mu_0)/dx}{d\sigma_3^{LO}(\mu_R = \mu_F = \mu_0)/dx}. \qquad [5.9]$$

In order to study scale variations, the relative change is computed according to the following formula,

$$\text{relative change} = \frac{d\sigma_3^{NLO}(\mu_R = \xi\mu_0, \mu_F = \mu_0)/dx}{d\sigma_3^{NLO}(\mu_R = \mu_F = \mu_0)/dx} \qquad [5.10]$$

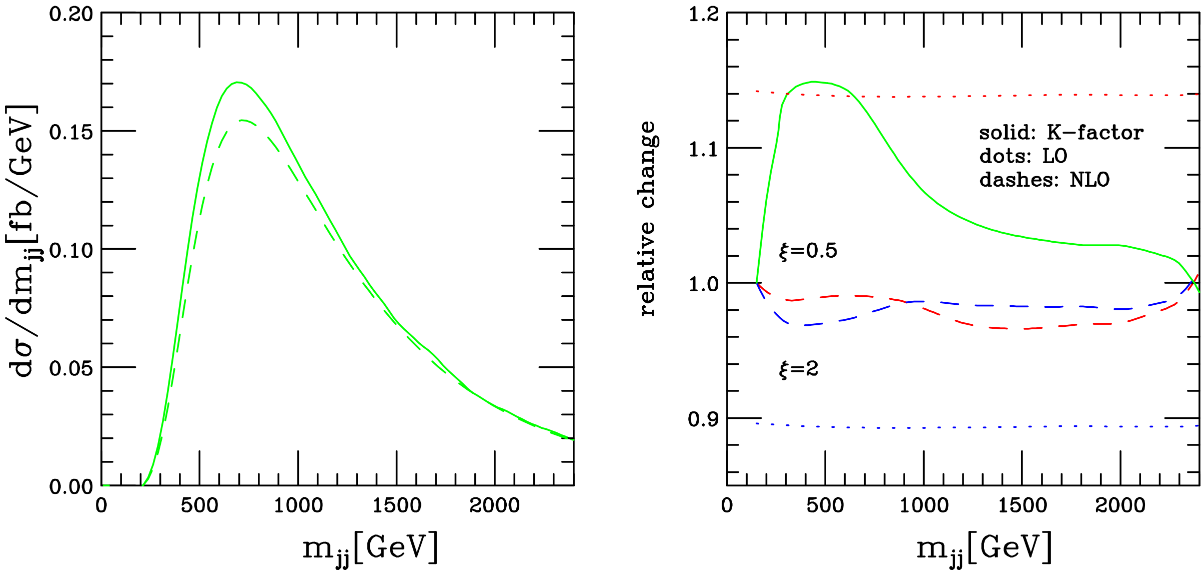

Figure 5.3 $Hjjj$ production with the cuts of Eqs.(5.1)-(5.5) and Eq.(5.6). In the left panel, $d\sigma/dm_{jj}$ (in fb/GeV) is shown at LO (dashed line) and NLO (solid line) for $\mu_F = \mu_R = 40$ GeV. In the right-hand panel the K factor (solid line) and scale variations of LO (dotted lines) and NLO (dashed lines) results are shown for $\mu_R = \xi\mu_0$ and $\mu_F = 40$ GeV with $\xi = 1/2$ and 2.

for $\xi = 1/2$ and 2 with $\mu_0 = 40$ GeV.

In the left-hand panel of Figure 5.2 the distribution $d\sigma/d\Delta y_{jj}$ is shown at LO (dashed line) and at NLO (solid line) for $Hjjj$ production. Just as in the NLO Hjj case, the peak in pushed towards higher values of rapidity separation Δy_{jj}. This strengthens the case for the rapidity gap cut of $\Delta y_{jj} > 4$. The K factor (solid line) in the right-hand-side of Figure 5.2 is highly phase space dependent. The scale variations $\xi = 2^{\pm 1}$ at NLO are -24% to $+12\%$ for $\Delta y_{jj} = 3$ while for tagging jet rapidity separations larger than 4.4 units the scale variations are less than $\pm 6\%$.

In Figure 5.3 for a fixed value of renormalization and factorization scale, $\mu_R = \mu_F = 40$ GeV, the distribution over the invariant mass of the tagging jets m_{jj} is shown. The K factor (solid line) peaks around $m_{jj} = 700$ GeV. The $\xi = 2^{\pm 1}$ scale variations are 0% to -3% over the entire range of invariant dijet mass for NLO (dashed lines) results while the variations at LO (dotted lines) are -10% to $+14\%$.

5.4 The Three Jet Cross Section

Here the dependence of the 3-jet ratio $R = \sigma_3/\sigma_2$ on the rapidity separation, Δy_{jj}, and the invariant mass, m_{jj}, of the tagging jets is investigated at NLO and LO. Here σ_3 and σ_2 denote cross sections for the Higgs plus two jet production via VBF (VBF Hjj) and Higgs plus three jet production via VBF (VBF $Hjjj$), respectively. In Figures (5.4, 5.5, 5.6,5.7) 3-jet ratios, $R(x)$, are plotted with respect to various kinematic variables, x. The NLO 3-jet ratio, $R^{NLO}(x)$, is defined as

$$R^{NLO}(x) = \frac{d\sigma_3^{NLO}(\mu_R, \mu_F)/dx}{d\sigma_2^{NLO}(\mu_R = \mu_F = m_h)/dx}, \qquad [5.11]$$

while the LO 3-jet ratio, $R^{LO}(x)$, is defined as

$$R^{LO}(x) = \frac{d\sigma_3^{LO}(\mu_R, \mu_F)/dx}{d\sigma_2^{NLO}(\mu_R = \mu_F = m_h)/dx}. \qquad [5.12]$$

Notice, that for R^{NLO} and R^{LO}, the Hjj distribution is computed to NLO accuracy. The Hjj cross section is computed at NLO because it provides the most accurate cross section. For the Hjj distributions, the NLO parton-level Monte Carlo program described in Chapter 2 is used with renormalization scale, μ_R, and factorization scale, μ_F, set to the mass of the Higgs boson, m_h. The $Hjjj$ cross section is computed using the NLO parton-level program described in Chapter 4. Calculations are performed for Higgs boson masses of $m_h = 120$ GeV and $m_h = 200$ GeV.

In Figures 5.4 and 5.6 the renormalization scale, μ_R, is varied while the factorization scale, μ_F, remains fixed at $\mu_0 = 40$ GeV. 3-jet ratios are plotted for $\mu_R = 20, 40, 80$, and 120 GeV. Applied cuts for both Figures 5.4 and 5.6 are Eqs.(5.1)-(5.5). For Figure 5.4, the dijet invariant mass cut of Eq.(5.7) is applied. For Figure 5.6, the rapidity gap cut of Eq.(5.6) is applied. The distribution in the rapidity separation of the tagging jets $\Delta y_{jj} = |y_j^{\text{tag 1}} - y_j^{\text{tag 2}}|$ is shown for both Hjj and $Hjjj$ production at LO and NLO in the left panel of Figure 5.4. In the right panel of Figure 5.4 the ratios R^{NLO} (solid) and R^{LO} (dashed) are shown. At LO the ratios R^{LO} (dashed curves) reach of value of 0.6 at $\Delta y_{jj} = 3$ whereas at NLO the ratios R^{NLO} (solid curves) reach a value of 0.4. The reason is that at NLO for Hjj production the peak for the $d\sigma/d\Delta y_{jj}$ distribution is pushed forward in rapidity separation. The effect is to enhance R^{LO} in the $\Delta y_{jj} = 3$ region. However, there is no such effect for R^{NLO} since for $Hjjj$ production the distribution in the rapidity separation of the tagging

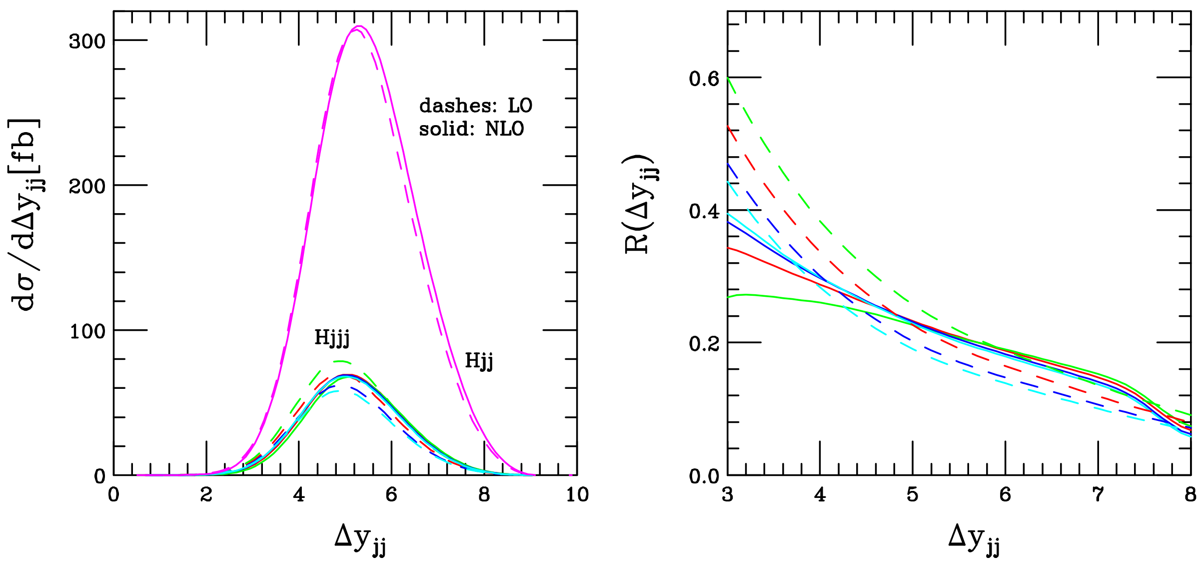

Figure 5.4 The rapidity separation of two tagging jets for $m_h = 120$ GeV within the cuts of Eqs.(5.1)-(5.5) and Eq.(5.7). In the left panel, $d\sigma/d\Delta y_{jj}$ (in fb) is shown at NLO (solid curves) and LO (dashed curves) for Hjj. For $Hjjj$ both LO (dashed curves) and NLO (solid curves) are shown for several choices of renormalization scale $\mu_R = 20, 40, 80$, and 120 GeV. In the right panel, LO 3-jet ratios, $R^{LO}(\Delta y_{jj})$ (dashed curves), and the NLO 3-jet ratios, $R^{NLO}(\Delta y_{jj})$ (solid curves) are shown for $\mu_R = 20, 40, 80$, and 120 GeV.

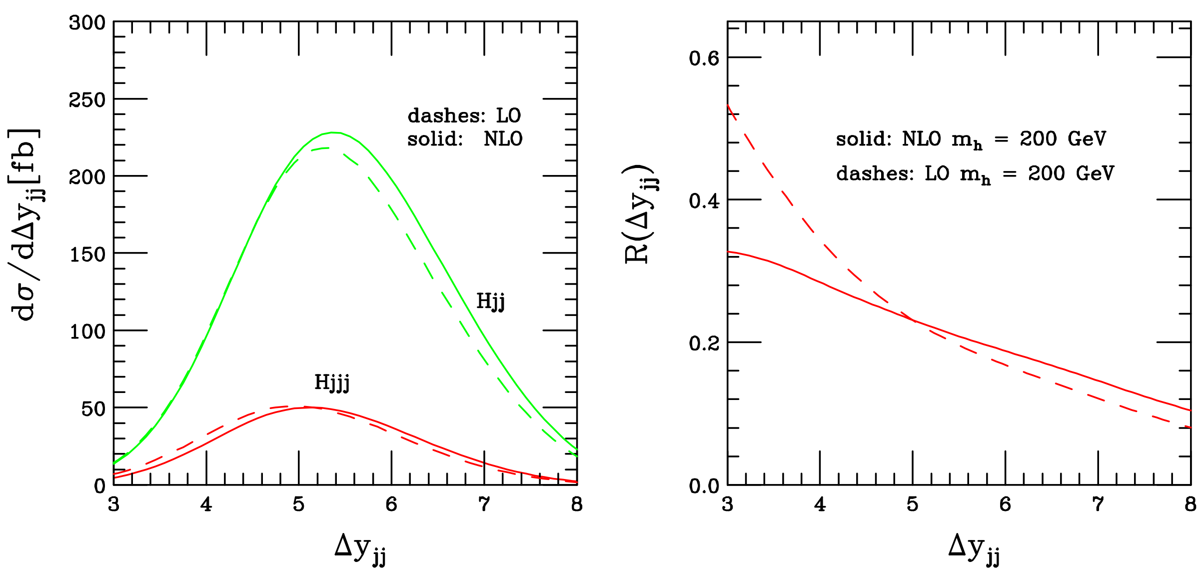

Figure 5.5 The $Hjjj$ rapidity separation of two tagging jets for $m_h = 200$ GeV within the cuts of Eqs. (5.1)-(5.5) and Eq.(5.7). In the left panel, $d\sigma/d\Delta y_{jj}$ (in fb) is shown at NLO (solid curves) and LO (dashed curves) for both Hjj and $Hjjj$. In the right panel, the LO 3-jet ratio $R^{LO}(\Delta y_{jj})$ (dashed curve) and the NLO 3-jet ratio $R^{NLO}(\Delta y_{jj})$ (solid curve) is shown for $\mu_R = 40$ GeV

jets is also pushed forward. Additionally, one notices that for higher values of Δy_{jj} renormalization scale dependences decrease. For both LO and NLO the ratios $R(\Delta y_{jj})$ monotonically decrease.

In the left panel of Figure 5.5 the rapidity separation of the tagging jets is shown for both Hjj and $Hjjj$ production at LO and NLO for a Higgs mass of $m_h = 200$ GeV for the cuts used in Figure 5.4. The corresponding ratios, R^{LO} and R^{NLO}, are shown for a fixed renormalization and factorization scale, $\mu_R = \mu_F = 40$ GeV in the right panel of Figure 5.5. Again, as in the case of a Higgs mass of $m_h = 120$ GeV, the ratio R^{NLO} has a steady downward slope. The ratio R^{LO} decreases more rapidly for a Δy_{jj} value below 5.

In Figure 5.6 the distribution in the invariant mass of the tagging jets is shown in the left panel for a Higgs boson mass of $m_h = 120$ GeV for Hjj and $Hjjj$ production at LO (dashed curves) and NLO (solid curves). Both the LO and NLO $Hjjj$ distributions are shown for several choices of renormalization scale in the range $20 \text{ GeV} \leq \mu_R \leq 120 \text{ GeV}$ in Figure 5.6. The corresponding ratios, R^{LO} and R^{NLO}, are shown in the left panel of Figure 5.6. The scale variations in the R^{LO} curves are large compared to the scale variations in the R^{NLO} curves. The distribution in the invariant mass of the tagging jets for a Higgs boson mass of $m_h = 200$ GeV is shown in the left panel of Figure 5.7 for Hjj and $Hjjj$ production at LO (dashed curves) and NLO (solid curves) for cuts used in Figure 5.6. For both $m_h = 120$ GeV and $m_h = 200$ GeV there is an enhancement in R^{NLO} in the vicinity of $m_{jj} = 700$ GeV. However, there are slight differences for $m_{jj} > 1500$ GeV. Qualitative features remain the same in both cases.

Another interesting observable is the distribution in the rapidity of a veto jet, measured with respect to the average rapidity of the tagging jets, $y_{\rm rel} = y_j^{\rm veto} - (y_j^{\rm tag\ 1} + y_j^{\rm tag\ 2})/2$. In addition to the cuts of Eqs.(5.1)-(5.7), the veto jet is required to have a transverse momentum $p_{Tj}^{\rm veto} \geq 20$ GeV and to reside in the gap region between the two tagging jets,

$$p_{Tj}^{\rm veto} \geq 20 \text{ GeV}, \qquad y_j^{\rm veto} \in (y_j^{\rm tag\ 1}, y_j^{\rm tag\ 2}). \qquad [5.13]$$

In Figures 5.8 and 5.9 the distribution of the cross section over y_{rel} is shown for the veto jet with the highest transverse momentum, $p_{Tj}^{\rm veto}$. [1]

[1]For 4-jet events there can be two veto jets. In this case, the veto jets are ordered by transverse momentum with $p_{Tj}^{\rm veto\ 1} > p_{Tj}^{\rm veto\ 2}$.

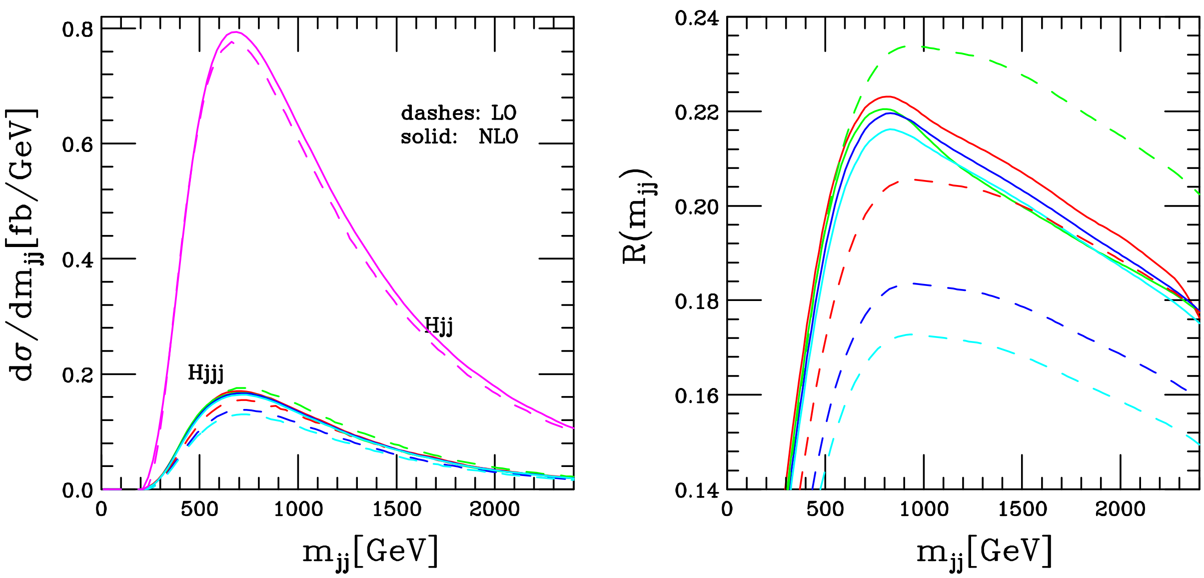

Figure 5.6 The invariant mass of two tagging jets for $m_h = 120$ GeV with the cuts of Eqs.(5.1)-(5.5) and Eq.(5.6). In the left panel, $d\sigma/dm_{jj}$ (in fb/GeV) is shown at NLO (solid curves) and LO (dashed curves) for Hjj. In addition, results for NLO (solid curves) and LO (dashed curves) for $Hjjj$ are shown for $\mu_R = 20, 40, 80$, and 120 GeV. In the right panel, LO 3-jet ratios, $R^{LO}(m_{jj})$ (dashed curves), and the NLO 3-jet ratios, $R^{NLO}(m_{jj})$ (solid curves) are shown for $\mu_R = 20, 40, 80$, and 120 GeV.

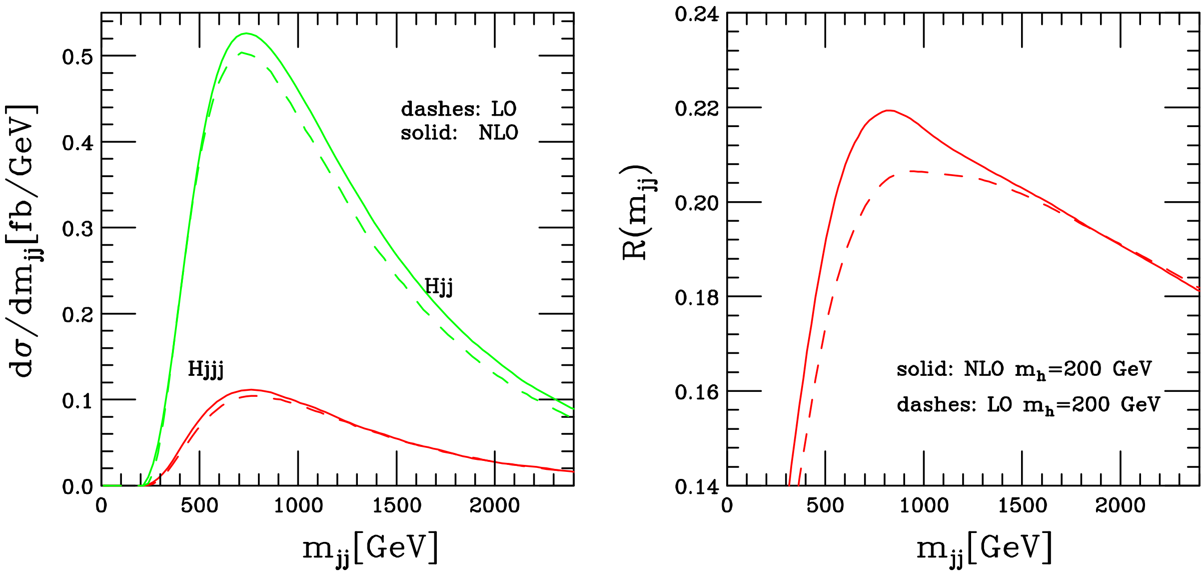

Figure 5.7 The invariant mass distribution of the two tagging jets for with the cuts of Eqs.(5.1)-(5.5) and Eq.(5.6) for a Higgs mass of $m_H = 200$ GeV. The chosen renormalization and factorization scales for Hjj production are $\mu_R = \mu_F = 200$ GeV and for $Hjjj$ production are $\mu_R = \mu_F = 40$ GeV. In the left panel, $d\sigma/dm_{jj}$ (in fb/GeV) is shown at NLO (solid curves) and LO (dashed curves) for Hjj and $Hjjj$ production. In the right panel, the LO 3-jet ratio $R^{LO}(m_{jj})$ (dashed curve), and the NLO 3-jet ratio, $R^{NLO}(m_{jj})$ (solid curve) are shown for $m_h = 200$ GeV.

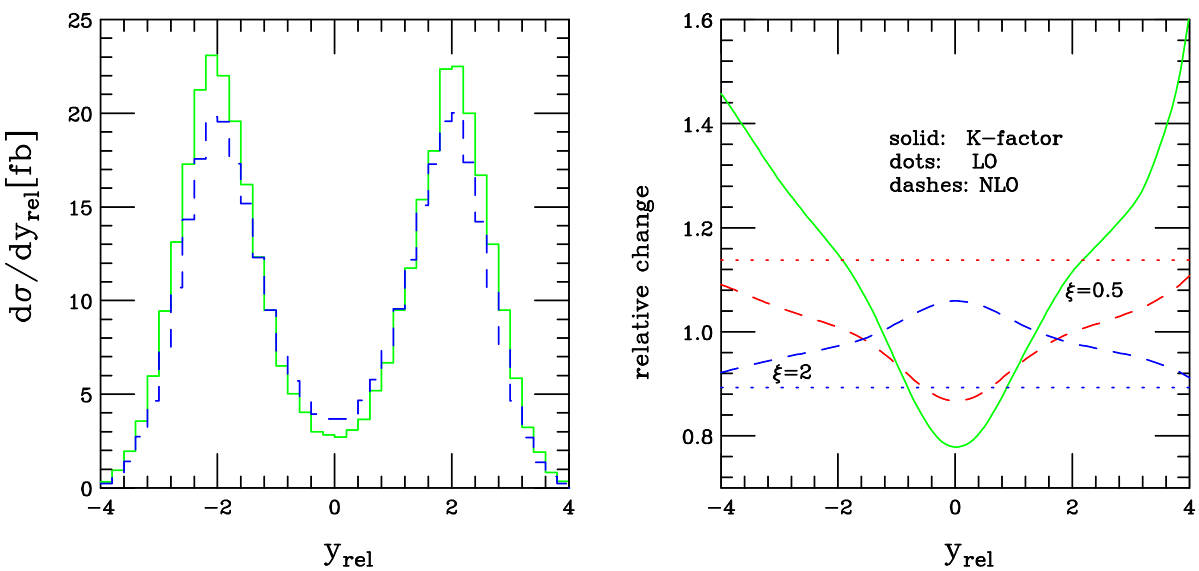

Figure 5.8 The distribution in rapidity of the highest p_T veto jet with the cuts of Eqs.(5.1)-(5.7) and Eq.(5.13), measured with respect to the rapidity average of the tagging jets, $y_{\rm rel} = y_j^{\rm veto} - (y_j^{\rm tag\ 1} + y_j^{\rm tag\ 2})/2$. In the left panel, $d\sigma/dy_{rel}$ (in fb) is shown at LO (dashed histogram) and NLO (solid histogram) for $\mu_F = \mu_R = 40$ GeV. In the right-hand panel the K factor (solid line) and scale variations of LO (dotted lines) and NLO (dashed lines) results are shown for $\mu_R = \xi\mu_0$ and $\mu_F = 40$ GeV with $\xi = 1/2$ and 2.

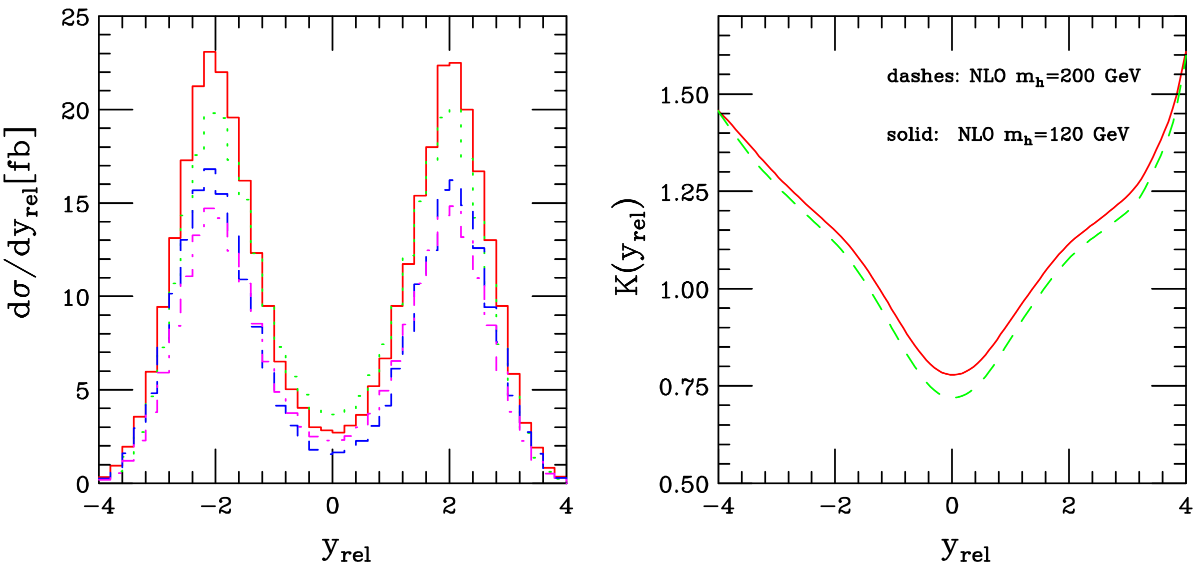

Figure 5.9 The distribution in rapidity of the highest p_T veto jet with the cuts of Eqs.(5.1)-(5.7) and Eq.(5.13), measured with respect to the rapidity average of the tagging jets, $y_{\rm rel} = y_j^{\rm veto} - (y_j^{\rm tag\ 1} + y_j^{\rm tag\ 2})/2$. In the left panel, $d\sigma/dy_{\rm rel}$ (in fb) is shown at NLO for $m_h = 120$ GeV (solid histogram) and $m_h = 200$ GeV (dashed histogram) and at LO for $m_h = 120$ GeV (dotted histogram) and $m_h = 200$ GeV (dash-dotted histogram). The factorization and renormalization scales are $\mu_R = \mu_F = 40$ GeV. In the right panel, the corresponding K factors are shown.

On the left-hand-side of Figure 5.8 the distribution in the rapidity of the highest p_T veto jet measured with respect to the average rapidity of the tagging jets is shown for $\mu_R = \mu_F = 40$ GeV at LO (dashed line) and NLO (solid line) for $m_h = 120$ GeV. The scale variations $\xi = 2^{\pm 1}$ for NLO results (dashed lines) are -15% to $+7\%$ in the vicinity of $y_{\rm rel} = 0$ and -11% to $+14\%$ throughout the range of $y_{\rm rel}$ for LO results (dotted lines). For $y_{\rm rel} \approx \pm 2$ scale variations at NLO are -2% to $+2\%$. In regions where the bulk of the cross section resides, the scale dependence is found to be reduced. The K factor (solid line) shown in Figure 5.8 is greater than one for $|y_{\rm rel}| > 2$ and is less than one in the central region between the tagging jets corresponding to $y_{\rm rel} = 0$.

In Figure 5.9 the distribution in the rapidity of the highest p_T veto jet measured with respect to the average rapidity of the tagging jets is shown in the left panel for Higgs masses of $m_h = 120$ GeV and $m_h = 200$ GeV. The right side of Figure 5.9 depicts the corresponding K factors as a function of $y_{\rm rel}$. For increased Higgs mass the K factor as a function of $y_{\rm rel}$ decreases. At the center of the tagging jets the decrease in K factor is on the order of 10%.

In Figure 5.10 the distribution in transverse momentum for the highest p_T veto jet is shown for $\mu_R = \mu_F = 40$ GeV at LO (dashed line) and NLO (solid line) for $m_h = 120$ GeV. The scale variations $\xi = 2^{\pm 1}$ for NLO results (dashed lines) are below $\pm 4\%$ for $p_{Tj}^{\rm veto}$ between 20 and 80 GeV. At LO (dotted lines) these scale variations are -11% to $+14\%$ for all values of veto jet transverse momentum. At NLO one sees a reduction in scale dependence. The K factor (solid line) monotonically decreases.

5.5 Concluding Remarks

Using both parton-level Monte Carlos for Hjj and $Hjjj$ production, the 3-jet ratios and scale dependences have been computed to NLO in QCD. At LO the scale dependence is $+25\%$ to -18% for total $Hjjj$ production cross sections while at NLO the scale uncertainty is less than $\pm 5\%$. At NLO one sees reduced scale variations in distributions compared to the LO distributions. In the central rapidity region between the tagging jets K factors are below one. Hence, there are fewer veto jets than predicted by a simple LO simulation.

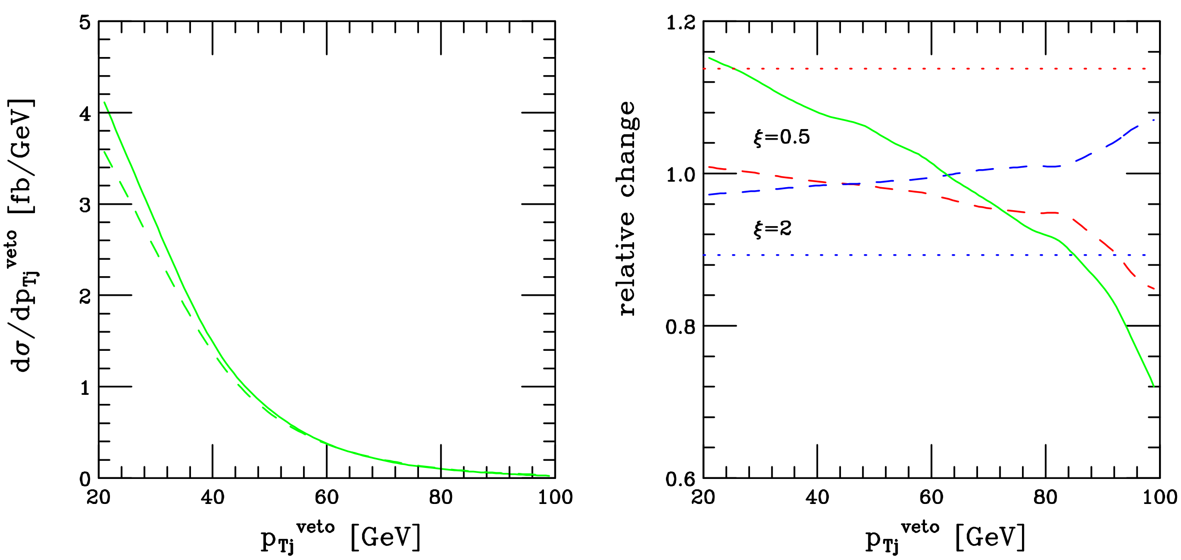

Figure 5.10 The distribution in the transverse momentum, $p_{Tj}^{\rm veto}$, for the highest p_T veto jet with the cuts of Eqs.(5.1)-(5.7) and Eq.(5.13). In the left panel, $d\sigma/dp_{Tj}^{\rm veto}$ (in fb/GeV) is shown at LO (dashed line) and NLO (solid line) for $\mu_F = \mu_R = 40$ GeV. In the right-hand panel the K factor (solid line) and scale variations of LO (dotted lines) and NLO (dashed lines) results are shown for $\mu_R = \xi\mu_0$ and $\mu_F = 40$ GeV with $\xi = 1/2$ and 2.

Chapter 6

Conclusions

This thesis has been devoted to the one-loop QCD corrections for vector-boson fusion processes involving the production of the Higgs boson at the Large Hadron Collider. In Chapter 2 the one-loop QCD corrections for Higgs production in association with two jets(Hjj) were presented in the form of a fully flexible parton-level Monte Carlo program. Scale uncertainties for distributions were shown to be on the order of less than 5% and for total cross sections to be below $\pm 2\%$ for the typical VBF cuts. K factors were shown to be modest, on the order of 5% to 10%. The modest size of the K factor is due to a small shift of the tagging jets toward higher rapidities. As a result the tagging jets are moved slightly further apart and hence allowing better differentiation of the Higgs boson signal against QCD backgrounds.

In Chapter 3 the NLO calculations of Chapter 2 were repeated for a Higgs boson with CP even and CP odd couplings to the vector bosons. It was shown that Higgs production via VBF is sensitive to the tensor structure of the HVV ($V = W, Z$) couplings which distinguishes loop induced vertices from SM vertices. The information shows up most clearly in the azimuthal angle correlations of the two tagging jets at the LHC. For the CP even coupling there is a dip at $\phi_{jj} = 90$ degrees in the azimuthal angle correlation while for the CP odd coupling there is suppression at 0 and 180 degrees in the azimuthal angle correlation. It was shown that gluon emission does not significantly change these correlations.

Analytic formulas for the construction of the NLO parton level Monte Carlo program were presented in Chapter 4 for Higgs production via vector-boson fusion in the association of three jets. Here the approximation of neglecting virtual graphs in which a gluon propagates from the upper quark line to the lower quark line was made since these contributions are suppressed by color and kinematics. Working in this approximation, the NLO QCD corrections were computed. In the subsequent chapter 3-jet ratios for Higgs production via VBF were computed to NLO accuracy using parton-level Monte Carlo programs for Hjj and $Hjjj$ production. In the same chapter the scale dependence of the $Hjjj$ cross section was also discussed. Here it was shown that for the NLO $Hjjj$ cross section the scale variations are on the order of less than 5%.

One cannot stress enough, how valuable having at our finger tips fully flexible NLO parton-level Monte Carlo programs is for future efforts to measure Higgs couplings at the LHC. NLO

Monte Carlo programs serve as powerful tools for studying Higgs physics at the LHC. In order for particle physics to move forward our researchers must be armed with these tools. This thesis has been part of that effort.

There are several areas in this thesis where further studies can be made. One area involves the computation of the hexagon and pentagon diagrams discussed in Chapter 4. These graphs were shown to be suppressed over much of the vector-boson search region. However, a solid proof of this would entail an exact calculation. Recently, new techniques for computing one-loop integrals have become available [52, 53, 54]. Using these techniques it may be possible to compute the exact NLO QCD corrections for $Hjjj$ production via vector-boson fusion in the near future.

Another area that is interesting is inclusion of anomalous Higgs couplings into the NLO calculation for $Hjjj$ production. With such a program, one could repeat calculations for the 3-jet ratios of Chapter 5 for the case in which the coupling of the Higgs boson to the vector boson is either CP even or CP odd as was done in Chapter 3 for Hjj production.

DISCARD THIS PAGE

Appendix A: Dipole Formulas

This appendix details the exact dipole functions used for the subtraction of soft and collinear divergences in the real emission integrals. The notation of Catani and Seymour (CS notation) [21] is interfaced with the notation of Campbell and Ellis (CE notation) [50]. The advantage of using CE notation is that dipole functions carry no color factors. This makes the final expressions more compact and transparent. The integrals of the dipole functions over the one-parton subspace are not given here. These can be found in Ref.[21]. In general there are four types of dipoles, corresponding to whether the emitter and spectator are in either the initial state or final state. The four cases are:

- final state singularities with final state spectator or final-final,
- final state singularities with initial state spectator or final-initial,
- initial state singularities with final state spectator or initial-final, and
- initial state singularities with initial state spectator or initial-initial.

In all cases $\tilde{ik}$ denotes the *emitter* parton emitting parton k with respect to *spectator* parton j. Initial partons are denoted by 1 and 2. While final state partons are labeled $3, \ldots, n$.

A.1 Final-final

Consider the case for which the emitter i and spectator j are both in the final state. The dipole factor in terms of CS notation is:

$$\mathcal{D}_{ik,j}(p_3, \ldots, p_{n+1}) = -\frac{1}{2p_i p_k} \qquad \text{[A.1]}$$
$$\cdot_n < 3, \ldots, (\tilde{ik}), .., \tilde{j}, .., n+1| \frac{\mathbf{T}_j \cdot \mathbf{T}_{ik}}{\mathbf{T}_{ik}^2} \mathbf{V}_{ik,j} |3, \ldots, (\tilde{ik}), .., \tilde{j}, .., n+1 >_n .$$

The splitting matrices $\mathbf{V}^{ik,j}$ in terms of CE notation are

$$\frac{1}{2p_i \cdot p_k} < s|V_{q_i g_k, j}(z; y)|s' > \;\; = \;\; C_F \delta_{ss'} \mathcal{D}^{ik,j}_{ff,qq}, \qquad \text{[A.2]}$$

$$\frac{1}{2p_i \cdot p_k} < \mu|V_{q_iq_k,j}(z)|\nu > \; = \; T_F(-g^{\mu\nu}\mathcal{D}^{ik,j}_{ff,gq} + q^\mu q^\nu \tilde{\mathcal{D}}^{ik,j}_{ff,gq}), \tag{A.3}$$

$$\frac{1}{2p_i \cdot p_k} < \mu|V_{g_ig_k,j}(z;y)|\nu > \; = \; C_A(-g^{\mu\nu}\mathcal{D}^{ik,j}_{ff,gg} + q^\mu q^\nu \tilde{\mathcal{D}}^{ik,j}_{ff,gg}). \tag{A.4}$$

The dimensionless variables y and z are defined to be

$$y = \frac{s_{ik}}{s_{ik} + s_{kj} + s_{ji}}, \quad z = \frac{s_{ij}}{s_{ij} + s_{kj}} \tag{A.5}$$

while the momenta of the emitter and spectator are defined to be

$$\tilde{p}^\mu_j = \frac{1}{1-y}p^\mu_j, \quad \tilde{p}^\mu_i = p^\mu_i + p^\mu_k - \frac{y}{1-y}p^\mu_j. \tag{A.6}$$

The dipoles of Ref.[50] in conventional dimensional regularization (CRD) are given by,

$$\mathcal{D}^{ik,j}_{ff,gg} = \frac{g^2\mu^{2\epsilon}}{p_i \cdot p_k}\left\{\frac{2}{1-z(1-y)} + \frac{2}{1-(1-z)(1-y)} - 4\right\} \tag{A.7}$$

$$\tilde{\mathcal{D}}^{ik,j}_{ff,gg} = \frac{g^2\mu^{2\epsilon}}{p_i \cdot p_k}(1-\epsilon)\frac{2}{p_i \cdot p_k} \tag{A.8}$$

$$\mathcal{D}^{ik,j}_{ff,gq} = \frac{g^2\mu^{2\epsilon}}{p_i \cdot p_k} \tag{A.9}$$

$$\tilde{\mathcal{D}}^{ik,j}_{ff,gq} = \frac{g^2\mu^{2\epsilon}}{p_i \cdot p_k}\frac{-2}{p_i \cdot p_k} \tag{A.10}$$

$$\mathcal{D}^{ik,j}_{ff,qq} = \frac{g^2\mu^{2\epsilon}}{p_i \cdot p_k}\left\{\frac{2}{1-z(1-y)} - (1+z) - \epsilon(1-z)\right\} \tag{A.11}$$

with,

$$q^\mu = zp^\mu_i - (1-z)p^\mu_k. \tag{A.12}$$

A.2 Final-initial

Consider the case of a final state emitter i with an initial state spectator j. In terms of CS notation the dipole factor is

$$\mathcal{D}^j_{ik}(p_1, \ldots, p_{n+1}) = -\frac{1}{2p_ip_k}\frac{1}{x} \tag{A.13}$$
$$\cdot_n < 3, \ldots, (\tilde{ik}).., n+1; \tilde{j}|\frac{\mathbf{T}_j \cdot \mathbf{T}_{ik}}{\mathbf{T}^2_{ik}}\mathbf{V}^j_{ik}|3, \ldots, (\tilde{ik}).., n+1; \tilde{j} >_n .$$

The splitting matrices $\mathbf{V}_{ik}^{j}$ in terms of CE notation are

$$\frac{1}{2p_i\cdot p_k}\frac{1}{x} < s|V^j_{q_i g_k}(z;x)|s' > \;=\; C_F\delta_{ss'}\mathcal{D}^{ik,j}_{fi,qq} \tag{A.14}$$

$$\frac{1}{2p_i\cdot p_k}\frac{1}{x} < \mu|V^j_{g_i g_k}(z;x)|\nu > \;=\; C_A(-g^{\mu\nu}\mathcal{D}^{ik,j}_{fi,gg} + q^\mu q^\nu \tilde{\mathcal{D}}^{ik,j}_{fi,gg}) \tag{A.15}$$

$$\frac{1}{2p_i\cdot p_k}\frac{1}{x} < \mu|V^j_{q_i \bar{q}_k}(z;x)|\nu > \;=\; T_F(-g^{\mu\nu}\mathcal{D}^{ik,j}_{fi,gq} + q^\mu q^\nu \tilde{\mathcal{D}}^{ik,j}_{fi,gq}). \tag{A.16}$$

Dimensionless variables x and z are defined as

$$x = 1 - \frac{s_{ik}}{s_{ij}+s_{kj}}, \quad z = \frac{s_{ij}}{s_{ij}+s_{kj}} \tag{A.17}$$

with transformed momenta being

$$\tilde{p}^\mu_j = xp^\mu_j, \quad \tilde{p}^\mu_i = p^\mu_i + p^\mu_k - (1-x)p^\mu_j. \tag{A.18}$$

The CE dipole functions are defined as

$$\mathcal{D}^{ik,j}_{fi,gg} = \frac{g^2\mu^{2\epsilon}}{xp_i\cdot p_k}\left\{\frac{2}{1-z+(1-x)} + \frac{2}{1-(1-z)+(1-x)} - 4\right\} \tag{A.19}$$

$$\tilde{\mathcal{D}}^{ik,j}_{fi,gg} = \frac{g^2\mu^{2\epsilon}}{xp_i\cdot p_k}(1-\epsilon)\frac{2}{p_i\cdot p_k} \tag{A.20}$$

$$\mathcal{D}^{ik,j}_{fi,gq} = \frac{g^2\mu^{2\epsilon}}{xp_i\cdot p_k} \tag{A.21}$$

$$\tilde{\mathcal{D}}^{ik,j}_{fi,gq} = \frac{g^2\mu^{2\epsilon}}{xp_i\cdot p_k}\frac{-2}{p_i\cdot p_k} \tag{A.22}$$

$$\mathcal{D}^{ik,j}_{fi,qq} = \frac{g^2\mu^{2\epsilon}}{xp_i\cdot p_k}\left\{\frac{2}{1-z+(1-x)} - (1+z) - \epsilon(1-z)\right\} \tag{A.23}$$

with,

$$q^\mu = zp^\mu_i - (1-z)p^\mu_k. \tag{A.24}$$

A.3 Initial-final

Consider the emitter parton i being in the initial state and the spectator parton j in the final state. The dipole factor in CS notation is

$$\mathcal{D}_j^{ik}(p_1,\ldots,p_{n+1}) = -\frac{1}{2p_ip_k}\frac{1}{x}$$
$$\cdot_n < 3,\ldots,\tilde{j}..,n+1;(\tilde{ik})|\frac{\mathbf{T}_j\cdot\mathbf{T}_{ik}}{\mathbf{T}_{ik}^2}\mathbf{V}_j^{ik}|3,\ldots,\tilde{j}..,n+1;(\tilde{ik}) >_n . \quad \text{[A.25]}$$

The splitting matrices $\mathbf{V}_j^{ik}$ in CE notation are

$$\frac{1}{2p_i\cdot p_k}\frac{1}{x} < s|V_j^{q_ig_k}(x;u)|s'> \;=\; C_F\delta_{ss'}\mathcal{D}_{if,qq}^{ik,j}, \quad \text{[A.26]}$$
$$\frac{1}{2p_i\cdot p_k}\frac{1}{x} < s|V_j^{g_i\bar{q}_k}(x;u)|s'> \;=\; T_F\delta_{ss'}\mathcal{D}_{if,qg}^{ik,j}, \quad \text{[A.27]}$$
$$\frac{1}{2p_i\cdot p_k}\frac{1}{x} < \mu|V_j^{q_iq_k}(x;u)|\nu> \;=\; C_F(-g^{\mu\nu}\mathcal{D}_{if,qg}^{ik,j}+q^\mu q^\nu\tilde{\mathcal{D}}_{if,qg}^{ik,j}), \quad \text{[A.28]}$$
$$\frac{1}{2p_i\cdot p_k}\frac{1}{x} < \mu|V_j^{g_ig_k}(x;u)|\nu> \;=\; C_F(-g^{\mu\nu}\mathcal{D}_{if,gg}^{ik,j}+q^\mu q^\nu\tilde{\mathcal{D}}_{if,gg}^{ik,j}). \quad \text{[A.29]}$$

The dimensionless variables x and u are defined as

$$x = 1-\frac{s_{jk}}{s_{ij}+s_{ik}}, \quad u = \frac{s_{ik}}{s_{ik}+s_{ij}}. \quad \text{[A.30]}$$

The momenta of the emitter and spectator are

$$\tilde{p}_i^\mu = xp_i^\mu, \quad \tilde{p}_j^\mu = p_j^\mu + p_k^\mu - (1-x)p_i^\mu. \quad \text{[A.31]}$$

The dipole functions of CE in CDR are

$$\mathcal{D}_{if,qq}^{ik,j} = \frac{g^2\mu^{2\epsilon}}{xp_i\cdot p_k}\left\{\frac{2}{1-x+u}-(1+x)-\epsilon(1-x)\right\}, \quad \text{[A.32]}$$

$$\mathcal{D}_{if,qg}^{ik,j} = \frac{g^2\mu^{2\epsilon}}{xp_i\cdot p_k}(1-\epsilon-2x(1-x)), \quad \text{[A.33]}$$

$$\mathcal{D}_{if,gq}^{ik,j} = \frac{g^2\mu^{2\epsilon}}{xp_i\cdot p_k}(x), \quad \text{[A.34]}$$

$$\mathcal{D}^{ik,j}_{if,gg} = \frac{g^2\mu^{2\epsilon}}{xp_i \cdot p_k}\left\{\frac{2}{1-x+u} - 2 + 2x(1-x)\right\}, \tag{A.35}$$

$$\tilde{\mathcal{D}}^{ik,j}_{if,gq} = \frac{g^2\mu^{2\epsilon}}{xp_i \cdot p_k}\frac{1-x}{x}\frac{2u(1-u)}{p_k \cdot p_j} \tag{A.36}$$

$$\tilde{\mathcal{D}}^{ik,j}_{if,gg} = (1-\epsilon)\tilde{\mathcal{D}}^{ik,j}_{if,gq} \tag{A.37}$$

$$\tilde{\mathcal{D}}^{ik,j}_{if,qq} = \tilde{\mathcal{D}}^{ik,j}_{if,qg} = 0 \tag{A.38}$$

With,

$$q^\mu = \frac{p_k^\mu}{u} - \frac{p_j^\mu}{1-u} \tag{A.39}$$

A.3.1 Initial-initial

Let i be the initial state emitter emitting k with spectator j.

$$\mathcal{D}^{ik,j}(p_1,\ldots,p_{n+1}) = -\frac{1}{2p_ip_k}\frac{1}{x} \tag{A.40}$$
$$\cdot_n < \tilde{3},\ldots,n\tilde{+}1;(\tilde{ik}),j|\frac{\mathbf{T}_j \cdot \mathbf{T}_{ik}}{\mathbf{T}^2_{ik}}\mathbf{V}^{ik,j}|\tilde{3},\ldots,n\tilde{+}1;(\tilde{ik}),j>_n$$

$$\frac{1}{2p_i \cdot p_k}\frac{1}{x} < s|V^{q_ig_k,j}(x)|s'>= \delta_{ss'}C_F\mathcal{D}^{ik,j}_{ii,qq} \tag{A.41}$$
$$\frac{1}{2p_i \cdot p_k}\frac{1}{x} < s|V^{g_i\bar{q}_k,j}(x)|s'>= \delta_{ss'}T_F\mathcal{D}^{ik,j}_{ii,qq} \tag{A.42}$$
$$\frac{1}{2p_i \cdot p_k}\frac{1}{x} < \mu|V^{q_iq_k,j}(x)|\nu>= C_F(-g^{\mu\nu}\mathcal{D}^{ik,j}_{ii,gq} + q^\mu q^\nu\tilde{D}^{ik,j}_{ii,gq}) \tag{A.43}$$
$$\frac{1}{2p_i \cdot p_k}\frac{1}{x} < \mu|V^{g_ig_k,j}(x)|\nu>= C_A(-g^{\mu\nu}\mathcal{D}^{ik,j}_{ii,gg} + q^\mu q^\nu\tilde{D}^{ik,j}_{ii,gg}) \tag{A.44}$$

The dimensionless variable x is defined as

$$x = 1 - \frac{s_{ki}+s_{kj}}{s_{ij}}. \tag{A.45}$$

The momenta of the emitter and spectator are

$$\tilde{p}_i^\mu = xp_i^\mu, \quad \tilde{p}_j^\mu = p_j^\mu. \tag{A.46}$$

All final state four momenta are Lorentz transformed as described in Ref.[21]. The dipole functions $\mathcal{D}^{ik,j}$ are

$$\mathcal{D}^{ik,j}_{ii,qq} = \frac{g^2\mu^{2\epsilon}}{xp_i \cdot p_k}\left\{\frac{2}{1-x} - (1+x) - \epsilon(1-x)\right\}, \tag{A.47}$$

$$\mathcal{D}^{ik,j}_{ii,qg} = \frac{g^2\mu^{2\epsilon}}{xp_i \cdot p_k}(1 - \epsilon - 2x(1-x)), \tag{A.48}$$

$$\mathcal{D}^{ik,j}_{ii,gq} = \frac{g^2\mu^{2\epsilon}}{xp_i \cdot p_k}(x), \tag{A.49}$$

$$\mathcal{D}^{ik,j}_{ii,gg} = \frac{g^2\mu^{2\epsilon}}{xp_i \cdot p_k}\left\{\frac{2x}{1-x} + 2x(1-x)\right\}. \tag{A.50}$$

The dipole functions $\tilde{\mathcal{D}}^{ik,j}$ are

$$\tilde{\mathcal{D}}^{ik,j}_{ii,gq} = \frac{g^2\mu^{2\epsilon}}{xp_i \cdot p_k}\frac{1-x}{x}\frac{p_i \cdot p_j}{p_k \cdot p_j p_k \cdot p_i}, \tag{A.51}$$

$$\tilde{\mathcal{D}}^{ik,j}_{ii,gg} = (1-\epsilon)\tilde{\mathcal{D}}^{ik,j}_{ii,gq}, \tag{A.52}$$

$$\tilde{\mathcal{D}}^{ik,j}_{ii,qq} = \tilde{\mathcal{D}}^{ik,j}_{ii,qg} = 0, \tag{A.53}$$

where

$$q^\mu = p_k^\mu - \frac{p_k \cdot p_j}{p_i \cdot p_j}p_j^\mu. \tag{A.54}$$

A.4 Flavor kernels

The Altarelli-Parisi splitting functions are

$$\begin{aligned} P^{qg}(x) &= P^{\bar{q}g}(x) = C_F\frac{1+(1-x)^2}{x}, && \text{[A.55]} \\ P^{gq}(x) &= P^{g\bar{q}}(x) = T_F\left[x^2 + (1-x)^2\right], && \text{[A.56]} \\ P^{qq}(x) &= P^{\bar{q}\bar{q}}(x) = C_F\left(\frac{1+x^2}{1-x}\right)_+, && \text{[A.57]} \end{aligned}$$

$$P^{gg}(x) = 2C_A\left[\left(\frac{1}{1-x}\right)_+ + \frac{1-x}{x} - 1 + x(1-x)\right] + \delta(1-x)\left(\frac{11}{6}C_A - \frac{2}{3}N_f T_F\right). \quad \text{[A.58]}$$

The constants obtained after integration of dipoles are

$$\gamma_q = \gamma_{\bar{q}} = \frac{3}{2}C_F, \qquad \gamma_g = \frac{11}{6}C_A - \frac{2}{3}T_F N_f, \quad \text{[A.59]}$$

and

$$K_q = K_{\bar{q}} = \left(\frac{7}{2} - \frac{\pi^2}{6}\right)C_F, \qquad K_g = \left(\frac{67}{18} - \frac{\pi^2}{6}\right)C_A - \frac{10}{9}T_F N_f, \quad \text{[A.60]}$$

related to the various integrals of the Altarelli-Parisi splitting functions.

$$\begin{aligned}
\overline{K}^{qg}(x) &= \overline{K}^{\bar{q}g}(x) = P^{qg}(x)\ln\frac{1-x}{x} + C_F x, && \text{[A.61]}\\
\overline{K}^{gq}(x) &= \overline{K}^{g\bar{q}}(x) = P^{gq}(x)\ln\frac{1-x}{x} + T_F 2x(1-x), && \text{[A.62]}\\
\overline{K}^{qq}(x) &= \overline{K}^{\bar{q}\bar{q}} = C_F\left[\left(\frac{2}{1-x}\ln\frac{1-x}{x}\right)_+ - (1+x)\ln\frac{1-x}{x} + (1-x)\right] && \text{[A.63]}\\
&- \delta(1-x)(5-\pi^2)C_F,\\
\overline{K}^{gg}(x) &= 2C_A\left[\left(\frac{1}{1-x}\ln\frac{1-x}{x}\right)_+ + \left(\frac{1-x}{x} - 1 + x(1-x)\right)\ln\frac{1-x}{x}\right]\\
&- \delta(1-x)\left[\left(\frac{50}{9} - \pi^2\right)C_A - \frac{16}{7}T_F N_f\right] && \text{[A.64]}
\end{aligned}$$

A.5 NLO cross sections at Hadron Colliders

For NLO QCD calculations involving two initial-state hadrons, it is required to introduce parton distribution functions. Let $f_{a/p}$ and $f_{b/p}$ denote parton densities for two incoming partons. The hadronic cross section is then given by

$$\begin{aligned}
\sigma(p_1, p_2) &= \sum_{a,b}\int_0^1 dx_1 f_{a/p}(x_1, \mu_F^2)\int_0^1 dx_2 f_{b/p}(x_2, \mu_F^2) && \text{[A.65]}\\
&\cdot \left[\sigma_{ab}^{LO}(x_1 p_1, x_2 p_2) + \sigma_{ab}^{NLO}(x_1 p_1, x_2 p_2; \mu_F^2)\right],
\end{aligned}$$

$$\begin{aligned}
\sigma_{ab}^{LO}(p_1, p_2) &= \int_n d\sigma_{ab}^B(p_1, p_2), && \text{[A.66]}\\
\sigma_{ab}^{NLO}(p_1, p_2, \mu_F^2) &= \int_{n+1} d\sigma_{ab}^R(p_1, p_2) + \int_n d\sigma_{ab}^V(p_1, p_2) + \int_n d\sigma_{ab}^C(p_1, p_2; \mu_F^2), && \text{[A.67]}
\end{aligned}$$

where the collinear counter-term is:

$$
\begin{aligned}
d\sigma^C_{ab}(p_1,p_2;\mu_F^2) &= -\frac{\alpha_s}{2\pi}\frac{1}{\Gamma(1-\epsilon)}\sum_{cd}\int_0^1 dz_1\int_0^1 dz_2 d\sigma^B_{cd}(z_1p_1,z_2p_2) \\
&\cdot \left\{\delta_{bd}\delta(1-z_2)\left[-\frac{1}{\epsilon}\left(\frac{4\pi\mu^2}{\mu_F^2}\right)^{\epsilon} P^{ac}(z_1)+K^{ac}_{\text{F.S.}}(z_1)\right]\right. \\
&+ \left.\delta_{ac}\delta(1-z_1)\left[-\frac{1}{\epsilon}\left(\frac{4\pi\mu^2}{\mu_F^2}\right)^{\epsilon} P^{bd}(z_2)+K^{bd}_{\text{F.S.}}(z_2)\right]\right\}.
\end{aligned}
\quad [A.68]
$$

The LO parton-level cross section is given by

$$
\begin{aligned}
\sigma^{LO}_{ab}(p_a,p_b) &= \int_n d\sigma^B_{ab}(p_a,p_b) \\
&= \int d\Phi^n(p_a,p_b)\frac{1}{n_c(a)n_c(b)}|\mathcal{M}_{n,ab}(p_1,\ldots,p_n;p_a,p_b)|^2 F_J^{(n)}(p_1,\ldots,p_n;p_a,p_b),
\end{aligned}
\quad [A.69]
$$

where a and b label the flavors of the incoming partons, p_a and p_b denote their four momenta, and $n_c(a)$ and $n_c(b)$ denote their number of colors. The matrix element, $|\mathcal{M}_{n,ab}|^2$ is the square of the tree-level amplitude to produce n partons in the final-state and $F_J^{(n)}$ is the jet defining function.

The full NLO partonic cross section consists of three different contributions:

$$
\begin{aligned}
\sigma^{NLO}_{ab}(p_a,p_b;\mu_F^2) &= \sigma^{NLO\{n+1\}}_{ab}(p_a,p_b)+\sigma^{NLO\{n\}}_{ab}(p_a,p_b) \\
&+ \int_0^1 dx\left[\hat{\sigma}^{NLO\{n\}}_{ab}(x;xp_a.p_b,\mu_F^2)+\hat{\sigma}^{NLO\{n\}}_{ab}(x;p_a,xp_b,\mu_F^2)\right].
\end{aligned}
\quad [A.70]
$$

The first contribution has $n+1$-parton kinematics and is given by the following expression

$$
\begin{aligned}
\sigma^{NLO\{n+1\}}_{ab}(p_a,p_b) &= \int d\Phi^{(n+1)}(p_a,p_b) \\
&\cdot \left\{\frac{1}{n_c(a)n_c(b)}|\mathcal{M}_{n+1,ab}(p_1,\ldots,p_{n+1};p_a,p_b)|^2 F_J^{(n+1)}(p_1,\ldots,p_{n+1};p_a,p_b)\right. \\
&- \left.\sum_{\text{dipoles}}\left(\mathcal{D}\cdot F^{(n)}\right)(p_1,\ldots,p_{n+1};p_a,p_b)\right\}
\end{aligned}
\quad [A.71]
$$

where $\mathcal{M}_{n+1,ab}$ is the tree-level matrix element with $n+1$ final-state partons and the sum of dipoles is given by the following expression

$$
\sum_{\text{dipoles}}\left(\mathcal{D}\cdot F^{(n)}\right) = \sum_{\substack{\text{pairs}\\ \text{i,j}}}\sum_{k\neq i,j}\mathcal{D}_{ij,k}(p_1,\ldots,p_{n+1};p_a,p_b)F_J^{(n)}(p_1,..\tilde{p}_{ij},\tilde{p}_k,\ldots,p_{n+1};p_a,p_b) \quad [A.72]
$$

$$
\begin{aligned}
&+\sum_{\substack{\text{pairs}\\ \text{i,j}}}\left[\mathcal{D}^{a}_{ij}(p_1,\ldots,p_{n+1};p_a,p_b)F_J^{(n)}(p_1,..\tilde{p}_{ij},\ldots,p_{n+1};\tilde{p}_a,p_b)+(a\leftrightarrow b)\right]\\
&+\sum_{i}\sum_{k\neq i}\left[\mathcal{D}^{ai}_{k}(p_1,\ldots,p_{n+1};p_a,p_b)F_J^{(n)}(p_1,..\tilde{p}_{k},\ldots,p_{n+1};\tilde{p}_{ai},p_b)+(a\leftrightarrow b)\right]\\
&+\sum_{i}\left[\mathcal{D}^{ai,b}(p_1,\ldots,p_{n+1};p_a,p_b)F_J^{(n)}(\tilde{p}_1,\ldots,\tilde{p}_{n+1};\tilde{p}_{ai},p_b)+(a\leftrightarrow b)\right].
\end{aligned}
$$

Integration of the above dipoles over the subspace of the unresolved parton and the subsequent cancellation of collinear singularities by the collinear counter-term, $d\sigma^C$ leads to the expression:

$$
\begin{aligned}
\int_{n+1} d\sigma^A_{ab}(p_a,p_b)+\int_n d\sigma^C_{ab} &= \int_n\left[d\sigma^B_{ab}(p_a,p_b)\cdot\mathbf{I}(\epsilon)\right]\\
&+\sum_{a'}\int_0^1 dx\int_n\left[(\mathbf{K}+\mathbf{P})^{a,a'}\cdot d\sigma^B_{a'b}(xp_a,p_b)\right]\\
&+\sum_{b'}\int_0^1 dx\int_n\left[(\mathbf{K}+\mathbf{P})^{b,b'}\cdot d\sigma^B_{ab'}(p_a,xp_b)\right],
\end{aligned}
\qquad [A.73]
$$

where $d\sigma^A \sim \sum_{\text{dipoles}}\left(\mathcal{D}\cdot F^{(n)}\right)$. Here $\mathbf{I}(\epsilon)$, $\mathbf{K}^{a,a'}$, and $\mathbf{P}^{a,a'}$ are insertion operators.

For a set of parton momenta $\{p\}$, the universal insertion operator $\mathbf{I}$ is defined as

$$
\mathbf{I}(\{p\};\epsilon)=-\frac{\alpha_s}{2\pi}\frac{1}{\Gamma(1-\epsilon)}\sum_I\frac{1}{\mathbf{T}_I^2}\mathcal{V}_I(\epsilon)\sum_{J\neq I}\mathbf{T}_I\cdot\mathbf{T}_J\left(\frac{4\pi\mu^2}{2p_I\cdot p_J}\right)^{\epsilon} \qquad [A.74]
$$

where I and J are indices over the parton momenta. The scalar product $p_I\cdot p_J$ is always positive. The universal singular function $\mathcal{V}_I$ depends only on the flavor of the parton and is given by

$$
\mathcal{V}_I=\mathbf{T}_I^2\left(\frac{1}{\epsilon^2}-\frac{\pi^2}{3}\right)+\gamma_I\frac{1}{\epsilon}+\gamma_I+K_I+\mathcal{O}(\epsilon), \qquad [A.75]
$$

where the constants γ_I and K_I are given in Eqs.(A.59,A.60).

The NLO contribution with n-parton kinematics is obtained by adding the virtual cross section and first term on the right-hand-side of Eq.(A.73). The explicit result is given here in terms of the square of the one-loop matrix element, $|\mathcal{M}_{n,ab}|^2_{1-loop}$, and the insertion operator, $\mathbf{I}(\epsilon)$:

$$
\begin{aligned}
\sigma^{NLO\{n\}}_{ab}(p_a,p_b) &= \int_n\left[d\sigma^V_{ab}(p_a,p_b)+d\sigma^B_{ab}(p_a,p_b)\otimes\mathbf{I}\right]_{\epsilon=0}\\
&= \int d\Phi^{(n)}(p_a,p_b)\left\{\frac{1}{n_c(a)n_c(b)}|\mathcal{M}_{n,ab}(p_1,\ldots,p_n;p_a,p_b)|^2_{1-loop}\right.\\
&+ \left.{}_{n,ab}<1,\ldots,n;a,b|\mathbf{I}(\epsilon)|1,\ldots,n;a,b>_{n,ab}\right\}_{\epsilon=0}F_J^{(n)}(p_1,\ldots,p_n;p_a,p_b).
\end{aligned}
\qquad [A.76]
$$

The second and third term of Eq.(A.73) give rise to the third term on the right-hand-side of Eq.(A.70). Each of these contributions is obtained by integrating a cross section with n-parton kinematics with respect to the fraction x of the longitudinal momentum carried by one of the incoming partons. For parton a, one has:

$$\int_0^1 dx \hat{\sigma}_{ab}^{NLO\{n\}}(x; xp_a, p_b, \mu_F^2) = \sum_{a'} \int_0^1 dx \int_n \left[d\sigma_{a'b}^B \otimes (\mathbf{K}+\mathbf{P})^{a.a'}(x)\right]_{\epsilon=0} \qquad [A.77]$$

$$= \sum_{a'} \int_0^1 dx \int d\Phi^{(n)}(xp_a, p_b) F_J^{(n)}(p_1, \ldots, p_n; p_a, p_b)$$

$$\cdot_{n,a'b} < 1, \ldots, n; xp_a, p_b| \left(\mathbf{K}^{a,a'}(x) + \mathbf{P}^{a,a'}(xp_a, x; \mu_F^2)\right) |1, \ldots, n; xp_a, p_b >_{n,a'b} .$$

The expression for $\hat{\sigma}_{ab}^{NLO\{n\}}(x; p_a, xp_b, \mu_F^2)$ is same as Eq.(A.77) apart from the replacements $xp_a \to p_a$, $p_b \to xp_b$, and $\sum_{a'} \to \sum_{b'}$.

$\mathbf{K}$ and $\mathbf{P}$ are universal insertion operators. In terms of $\{p\}$ and I notation, they are given by

$$\mathbf{P}^{a,b}(\{p\}; xp_a, x; \mu_F^2) = \frac{\alpha_s}{2\pi} P^{ab}(x) \frac{1}{\mathbf{T}_b^2} \sum_{I \neq b} \mathbf{T}_I \cdot \mathbf{T}_b \ln \frac{\mu_F^2}{2xp_a \cdot p_I}, \qquad [A.78]$$

and

$$\mathbf{K}^{a,b}(x) = \frac{\alpha_s}{2\pi} \left\{ \overline{K}^{ab}(x) - K_{\text{F.S.}}^{ab}(x) + \delta^{ab} \sum_i \mathbf{T}_i \cdot \mathbf{T}_b \frac{\gamma_i}{\mathbf{T}_i^2} \left[\left(\frac{1}{1-x} \right)_+ + \delta(1-x) \right] \right\}. \qquad [A.79]$$

For the $\overline{\text{MS}}$ factorization scheme $K_{\text{F.S.}} = 0$.

In order to evaluate the NLO cross sections with n-parton kinematics, the color-charge operators $\mathbf{I}$, $\mathbf{P}$, and $\mathbf{K}$ have to be inserted into the tree-level matrix elements. This leads to the computation of color-correlated tree-amplitudes. Let $\{p\}$ denote the generic set of N parton momenta. The square $|\mathcal{M}^{I,J}$ of the color-correlated amplitude in terms of the colored tree-level amplitude $\mathcal{M}^{a_1 \ldots a_N}(\{p\})$ is

$$\begin{aligned} |\mathcal{M}^{I.J}(\{p\})|^2 &\equiv < \{p\}|\mathbf{T}_I \cdot \mathbf{T}_J|\{p\} > \qquad [A.80] \\ &= \frac{1}{n_c(a) n_c(b)} \left[\mathcal{M}^{a_1..b_I..b_J..a_N}(\{p\})\right]^* T_{b_I a_I}^c T_{b_J a_J}^c \mathcal{M}^{a_1..a_I..a_J..a_N}(\{p\}). \end{aligned}$$

Here the $a_1 \ldots a_N$ are color indices. The color-charge operator of a final-state parton i is $T_{cb}^a \equiv if_{cab}$ (color-charge matrix in the adjoint representation) if the emitting particle i is a gluon and

$T^a_{\alpha\beta} \equiv t^a_{\alpha\beta}$ (color-charge matrix in the fundamental representation) if the emitting particle i is a quark (in the case of an emitting anti-quark $T^a_{\alpha\beta} \equiv \bar{t}^a_{\alpha\beta} = -t^a_{\beta\alpha}$). The color-charge operator of an initial-state parton a is defined by crossing symmetry. That is, $(\mathbf{T}_a)^c_{bd} = if_{bcd}$ if a is a gluon and $(\mathbf{T}_a)^c_{\alpha\beta} = \bar{t}^c_{\alpha\beta} = -t^c_{\beta\alpha}$ if a is a quark (if a is an anti-quark, $(\mathbf{T}_a)^c_{\alpha\beta} = t^c_{\alpha\beta}$).

Appendix B: Boxline virtual corrections

The finite contributions to the boxline virtual corrections of Chapter 4 are expressed in terms of $\tilde{C}_0$, $\tilde{B}_0$, and $\tilde{D}_{ij}$ functions. $\tilde{C}_0$, $\tilde{B}_0$, and $\tilde{D}_{ij}$ are finite parts of the Passarino-Veltman C_0, B_0, and D_{ij} functions. The B_0, C_0, and D_0 functions used here are defined in Appendix C.

$$\tilde{\mathcal{M}}_\tau^{(1)}(k_2,q_1,q_2;\epsilon_1,\epsilon_2) = \bar{\psi}(k_2)\{c_q^{(1)}(\not{q}_1-\not{q}_2)+c_1^{(1)}\not{\epsilon}_1+c_2^{(1)}\not{\epsilon}_2+c_b^{(1)}\not{\epsilon}_2(\not{k}_2+\not{q}_2)\not{\epsilon}_1\}P_\tau\psi(k_1) \quad \text{[B.1]}$$

$$\tilde{\mathcal{M}}_\tau^{(2)}(k_2,q_1,q_2;\epsilon_1,\epsilon_2) = \bar{\psi}(k_2)\{c_q^{(2)}(\not{q}_1-\not{q}_2)+c_1^{(2)}\not{\epsilon}_1+c_2^{(2)}\not{\epsilon}_2+c_b^{(2)}\not{\epsilon}_1(\not{k}_2+\not{q}_1)\not{\epsilon}_2\}P_\tau\psi(k_1) \quad \text{[B.2]}$$

$$\begin{aligned}\tilde{\mathcal{M}}_\tau^{(3)}(k_2,q_1,q_2;\epsilon_1,\epsilon_2) &= \bar{\psi}(k_2)\{c_q^{(3)}(\not{q}_1-\not{q}_2)+c_1^{(3)}\not{\epsilon}_1+c_2^{(3)}\not{\epsilon}_2\\ &+ c_b^{(3)}(\not{\epsilon}_1(\not{k}_2+\not{q}_1)\not{\epsilon}_2+\not{\epsilon}_2(\not{k}_2+\not{q}_2)\not{\epsilon}_1)\}P_\tau\psi(k_1) \qquad \text{[B.3]}\end{aligned}$$

$$c_b^{(1)} = \mathbf{Box}_b^{(1)} - \frac{2\,\tilde{B}_0(t)}{t} - \frac{T_b(q_2^2,t)}{t} \quad \text{[B.4]}$$

$$c_1^{(1)} = \mathbf{Box}_1^{(1)} + 2\,\epsilon_2 k_2 T_\epsilon(q_2^2,t) - 2\,\epsilon_2 q_2\frac{[\tilde{B}_0(t)-\tilde{B}_0(q_2^2)]}{t-q_2^2} \quad \text{[B.5]}$$

$$c_2^{(1)} = \mathbf{Box}_2^{(1)} + 2\,\epsilon_1 k_1 T_\epsilon(0,t) \quad \text{[B.6]}$$

$$c_b^{(2)} = \mathbf{Box}_b^{(2)} - \frac{2\,\tilde{B}_0(u)}{u} - \frac{T_b(q_2^2,u)}{u} \quad \text{[B.7]}$$

$$c_1^{(2)} = \mathbf{Box}_1^{(2)} + 2\,\epsilon_2 k_1 T_\epsilon(q_2^2,u) - 2\,\epsilon_2 q_2\frac{[\tilde{B}_0(u)-\tilde{B}_0(q_2^2)]}{u-q_2^2} \quad \text{[B.8]}$$

$$c_2^{(2)} = \mathbf{Box}_2^{(2)} + 2\,\epsilon_1 k_2 T_\epsilon(0,u) \quad \text{[B.9]}$$

$$tc_b^{(3)} = t\mathbf{Box}_b^{(3)} - 2(t\tilde{C}_0(t)+1) + \tilde{B}_0(t) + T_b(q_2^2,t) \quad \text{[B.10]}$$

$$uc_b^{(3)} = u\mathbf{Box}_b^{(3)} - 2(u\tilde{C}_0(u)+1) + \tilde{B}_0(u) + T_b(q_2^2,u) \quad \text{[B.11]}$$

$$\begin{aligned}c_1^{(3)} &= \mathbf{Box}_1^{(3)} - 2\epsilon_2 k_2 T_\epsilon(q_2^2,t) + 2\epsilon_2 q_2\frac{[\tilde{B}_0(t)-\tilde{B}_0(q_2^2)]}{t-q_2^2} \qquad \text{[B.12]}\\ &- 2\epsilon_2 k_1 T_\epsilon(q_2^2,u) - 2\epsilon_2 q_2\frac{[\tilde{B}_0(u)-\tilde{B}_0(q_2^2)]}{u-q_2^2}\end{aligned}$$

$$c_2^{(3)} = \mathbf{Box}_2^{(3)} + \frac{2}{t}(t\tilde{C}_0(t)+1)\epsilon_1 k_1 + \frac{2}{u}(u\tilde{C}_0(u)+1)\epsilon_1 k_2 \quad \text{[B.13]}$$

$$\begin{aligned}
T_b(q^2,t) &= \frac{1}{t-q^2}\{2q^2[\tilde{B}_0(t)-\tilde{B}_0(q^2)]+t\tilde{B}_0(t) \\
&\quad -q^2\tilde{B}_0(q^2)\}-2q^2\tilde{C}_0(q^2,t) && \text{[B.14]} \\
T_\epsilon(q^2,t) &= \frac{1}{t-q^2}\{[\tilde{B}_0(t)-\tilde{B}_0(q^2)]\frac{2t+3q^2}{t-q^2}+2\tilde{B}_0(q^2)+1-2q^2\tilde{C}_0(q^2,t)\} && \text{[B.15]} \\
T_\epsilon(0,t) &= \frac{1}{t}(2\tilde{B}_0(t)+1) && \text{[B.16]} \\
T_b(0,t) &= \tilde{B}_0(t) && \text{[B.17]}
\end{aligned}$$

Here the coefficients $\mathbf{Box}_i^j$ for $j=1,2,3$ and $i=b,q,1,2$ are expressed in terms of the Passarino-Veltman $\tilde{D}_{ij}$ functions.

$$\begin{aligned}
\mathbf{Box}_q^{(3)} &= -\tilde{D}_{27}(q_1,k_2,q_2)\epsilon_1\epsilon_2-2\tilde{D}_{311}(q_1,k_2,q_2)\epsilon_1\epsilon_2+2\tilde{D}_{313}(q_1,k_2,q_2)\epsilon_1\epsilon_2 \\
&- 8\tilde{D}_{12}(q_1,k_2,q_2)\epsilon_1k_2\epsilon_2k_2+8\tilde{D}_{13}(q_1,k_2,q_2)\epsilon_1k_2\epsilon_2k_2-4\tilde{D}_{22}(q_1,k_2,q_2)\epsilon_1k_2\epsilon_2k_2 \\
&- 8\tilde{D}_{24}(q_1,k_2,q_2)\epsilon_1k_2\epsilon_2k_2+12\tilde{D}_{26}(q_1,k_2,q_2)\epsilon_1k_2\epsilon_2k_2-4\tilde{D}_{36}(q_1,k_2,q_2)\epsilon_1k_2\epsilon_2k_2 \\
&+ 4\tilde{D}_{38}(q_1,k_2,q_2)\epsilon_1k_2\epsilon_2k_2+\frac{3}{2}\tilde{D}_{0}(q_1,k_2,q_2)\epsilon_1q_2\epsilon_2k_2+\frac{3}{2}\tilde{D}_{12}(q_1,k_2,q_2)\epsilon_1q_2\epsilon_2k_2 \\
&+ 4\tilde{D}_{23}(q_1,k_2,q_2)\epsilon_1q_2\epsilon_2k_2-8\tilde{D}_{25}(q_1,k_2,q_2)\epsilon_1q_2\epsilon_2k_2+4\tilde{D}_{26}(q_1,k_2,q_2)\epsilon_1q_2\epsilon_1k_2 \\
&- 4\tilde{D}_{310}(q_1,k_2,q_2)\epsilon_1q_2\epsilon_2k_2+4\tilde{D}_{39}(q_1,k_2,q_2)\epsilon_1q_2\epsilon_2k_2-\frac{3}{2}\tilde{D}_{0}(q_1,k_2,q_2)\epsilon_1k_2\epsilon_2q_1 \\
&- \frac{19}{2}\tilde{D}_{12}(q_1,k_2,q_2)\epsilon_1k_2\epsilon_2q_1+8\tilde{D}_{13}(q_1,k_2,q_2)\epsilon_1k_2\epsilon_2q_1-12\tilde{D}_{24}(q_1,k_2,q_2)\epsilon_1k_2\epsilon_2q_1 \\
&+ 8\tilde{D}_{25}(q_1,k_2,q_2)\epsilon_1k_2\epsilon_2q_1+4\tilde{D}_{26}(q_1,k_2,q_2)\epsilon_1k_2\epsilon_2q_1+4\tilde{D}_{310}(q_1,k_2,q_2)\epsilon_1k_2\epsilon_2q_1 \\
&- 4\tilde{D}_{34}(q_1,k_2,q_2)\epsilon_1k_2\epsilon_2q_1+4\tilde{D}_{23}(q_1,k_2,q_2)\epsilon_1q_2\epsilon_2q_1-4\tilde{D}_{25}(q_1,k_2,q_2)\epsilon_1q_2\epsilon_2q_1 \\
&- 4\tilde{D}_{35}(q_1,k_2,q_2)\epsilon_1q_2\epsilon_2q_1+4\tilde{D}_{37}(q_1,k_2,q_2)\epsilon_1q_2\epsilon_2q_1-\frac{3}{2}\tilde{D}_{0}(q_1,k_2,q_2)\epsilon_1k_2\epsilon_2q_2 \\
&- \frac{11}{2}\tilde{D}_{12}(q_1,k_2,q_2)\epsilon_1k_2\epsilon_2q_2+4\tilde{D}_{13}(q_1,k_2,q_2)\epsilon_1k_2\epsilon_2q_2+8\tilde{D}_{23}(q_1,k_2,q_2)\epsilon_1k_2\epsilon_2q_2 \\
&- 4\tilde{D}_{24}(q_1,k_2,q_2)\epsilon_1k_2\epsilon_2q_2-4\tilde{D}_{26}(q_1,k_2,q_2)\epsilon_1k_2\epsilon_2q_2-4\tilde{D}_{310}(q_1,k_2,q_2)\epsilon_1k_2\epsilon_2q_2 \\
&+ 4\tilde{D}_{39}(q_1,k_2,q_2)\epsilon_1k_2\epsilon_2q_2+4\tilde{D}_{23}(q_1,k_2,q_2)\epsilon_1q_2\epsilon_2q_2-4\tilde{D}_{25}(q_1,k_2,q_2)\epsilon_1q_2\epsilon_2q_2 \\
&+ 4\tilde{D}_{33}(q_1,k_2,q_2)\epsilon_1q_2\epsilon_2q_2-4\tilde{D}_{37}(q_1,k_2,q_2)\epsilon_1q_2\epsilon_2q_2-\frac{1}{2}\tilde{D}_{12}(q_1,k_2,q_2)\epsilon_1\epsilon_2q_2^2 \\
&+ \frac{1}{2}\tilde{D}_{13}(q_1,k_2,q_2)\epsilon_1\epsilon_2q_2^2+\frac{1}{2}\tilde{D}_{23}(q_1,k_2,q_2)\epsilon_1\epsilon_2q_2^2)-\frac{1}{2}\tilde{D}_{24}(q_1,k_2,q_2)\epsilon_1\epsilon_2q_2^2 \\
&- \tilde{D}_{310}(q_1,k_2,q_2)\epsilon_1\epsilon_2q_2^2-\tilde{D}_{33}(q_1,k_2,q_2)\epsilon_1\epsilon_2q_2^2+\tilde{D}_{37}(q_1,k_2,q_2)\epsilon_1\epsilon_2q_2^2
\end{aligned}$$

$$
\begin{aligned}
&+ \quad \tilde{D}_{39}(q_1,k_2,q_2)\epsilon_1\epsilon_2 q_2^2 - \tilde{D}_0(q_1,k_2,q_2)\epsilon_1\epsilon_2 t - \frac{3}{2}\tilde{D}_{11}(q_1,k_2,q_2)\epsilon_1\epsilon_2 t \\
&+ \quad \frac{1}{2}\tilde{D}_{12}(q_1,k_2,q_2)\epsilon_1\epsilon_2 t - \frac{1}{2}\tilde{D}_{21}(q_1,k_2,q_2)\epsilon_1\epsilon_2 t + \frac{1}{2}\tilde{D}_{24}(q_1,k_2,q_2)\epsilon_1\epsilon_2 t \\
&+ \quad \tilde{D}_{310}(q_1,k_2,q_2)\epsilon_1\epsilon_2 t - \tilde{D}_{35}(q_1,k_2,q_2)\epsilon_1\epsilon_2 t + \tilde{D}_{37}(q_1,k_2,q_2)\epsilon_1\epsilon_2 t \\
&- \quad \tilde{D}_{39}(q_1,k_2,q_2)\epsilon_1\epsilon_2 t - \frac{11}{2}\tilde{D}_{11}(q_1,k_2,q_2)\epsilon_1\epsilon_2 u + \frac{3}{2}\tilde{D}_{12}(q_1,k_2,q_2)\epsilon_1\epsilon_2 u \\
&- \quad \tilde{D}_{13}(q_1,k_2,q_2)\epsilon_1\epsilon_2 u + \frac{1}{2}\tilde{D}_{21}(q_1,k_2,q_2)\epsilon_1\epsilon_2 u + \tilde{D}_{23}(q_1,k_2,q_2)\epsilon_1\epsilon_2 u \\
&+ \quad \frac{3}{2}\tilde{D}_{24}(q_1,k_2,q_2)\epsilon_1\epsilon_2 u - 2\tilde{D}_{25}(q_1,k_2,q_2)\epsilon_1\epsilon_2 u - \tilde{D}_{26}(q_1,k_2,q_2)\epsilon_1\epsilon_2 u \\
&- \quad \tilde{D}_{310}(q_1,k_2,q_2)\epsilon_1\epsilon_2 u + \tilde{D}_{34}(q_1,k_2,q_2)\epsilon_1\epsilon_2 u - \tilde{D}_{35}(q_1,k_2,q_2)\epsilon_1\epsilon_2 u \\
&+ \quad \tilde{D}_{37}(q_1,k_2,q_2)\epsilon_1\epsilon_2 u
\end{aligned} \tag{B.18}
$$

$$
\begin{aligned}
\mathbf{Box}_1^{(3)} &= 24\tilde{D}_{27}(q_1,k_2,q_2)\epsilon_2 k_2 + 20\tilde{D}_{312}(q_1,k_2,q_2)\epsilon_2 k_2 + 22\tilde{D}_{27}(q_1,k_2,q_2)\epsilon_2 q_1 \\
&+ 20\tilde{D}_{311}(q_1,k_2,q_2)\epsilon_2 q_1 + 12\tilde{D}_{27}(q_1,k_2,q_2)\epsilon_2 q_2 + 20\tilde{D}_{313}(q_1,k_2,q_2)\epsilon_2 q_2 \\
&- 4\tilde{D}_{23}(q_1,k_2,q_2)\epsilon_2 k_2 q_2^2 + 4\tilde{D}_{26}(q_1,k_2,q_2)\epsilon_2 k_2 q_2^2 + 2\tilde{D}_{38}(q_1,k_2,q_2)\epsilon_2 k_2 q_2^2 \\
&- 2\tilde{D}_{39}(q_1,k_2,q_2)\epsilon_2 k_2 q_2^2 + \tilde{D}_{12}(q_1,k_2,q_2)\epsilon_2 q_1 q_2^2 - \tilde{D}_{13}(q_1,k_2,q_2)\epsilon_2 q_1 q_2^2 \\
&- 3\tilde{D}_{23}(q_1,k_2,q_2)\epsilon_2 q_1 q_2^2 + \tilde{D}_{24}(q_1,k_2,q_2)\epsilon_2 q_1 q_2^2 + 2\tilde{D}_{26}(q_1,k_2,q_2)\epsilon_2 q_1 q_2^2 \\
&+ 2\tilde{D}_{310}(q_1,k_2,q_2)\epsilon_2 q_1 q_2^2 - 2\tilde{D}_{37}(q_1,k_2,q_2)\epsilon_2 q_1 q_2^2 - 2\tilde{D}_{23}(q_1,k_2,q_2)\epsilon_2 q_2 q_2^2 \\
&+ 2\tilde{D}_{26}(q_1,k_2,q_2)\epsilon_2 q_2 q_2^2 - 2\tilde{D}_{33}(q_1,k_2,q_2)\epsilon_2 q_2 q_2^2 + 2\tilde{D}_{39}(q_1,k_2,q_2)\epsilon_2 q_2 q_2^2 \\
&+ \frac{3}{2}\tilde{D}_0(q_1,k_2,q_2)\epsilon_2 k_2 t + \frac{3}{2}\tilde{D}_{12}(q_1,k_2,q_2)\epsilon_2 k_2 t + 4\tilde{D}_{13}(q_1,k_2,q_2)\epsilon_2 k_2 t \\
&+ 2\tilde{D}_{25}(q_1,k_2,q_2)\epsilon_2 k_2 t + 2\tilde{D}_{26}(q_1,k_2,q_2)\epsilon_2 k_2 t + 2\tilde{D}_{310}(q_1,k_2,q_2)\epsilon_2 k_2 t \\
&- 2\tilde{D}_{38}(q_1,k_2,q_2)\epsilon_2 k_2 t + 2\tilde{D}_0(q_1,k_2,q_2)\epsilon_2 q_1 t + 3\tilde{D}_{11}(q_1,k_2,q_2)\epsilon_2 q_1 t \\
&- \tilde{D}_{12}(q_1,k_2,q_2)\epsilon_2 q_1 t + 4\tilde{D}_{13}(q_1,k_2,q_2)\epsilon_2 q_1 t + \tilde{D}_{21}(q_1,k_2,q_2)\epsilon_2 q_1 t \\
&- \tilde{D}_{24}(q_1,k_2,q_2)\epsilon_2 q_1 t + 6\tilde{D}_{25}(q_1,k_2,q_2)\epsilon_2 q_1 t - 2\tilde{D}_{26}(q_1,k_2,q_2)\epsilon_2 q_1 t \\
&- 2\tilde{D}_{310}(q_1,k_2,q_2)\epsilon_2 q_1 t + 2\tilde{D}_{35}(q_1,k_2,q_2)\epsilon_2 q_1 t + 4\tilde{D}_{13}(q_1,k_2,q_2)\epsilon_2 q_2 t \\
&+ 4\tilde{D}_{23}(q_1,k_2,q_2)\epsilon_2 q_2 t + 2\tilde{D}_{25}(q_1,k_2,q_2)\epsilon_2 q_2 t - 2\tilde{D}_{26}(q_1,k_2,q_2)\epsilon_2 q_2 t \\
&+ 2\tilde{D}_{37}(q_1,k_2,q_2)\epsilon_2 q_2 t - 2\tilde{D}_{39}(q_1,k_2,q_2)\epsilon_2 q_2 t + \frac{3}{2}\tilde{D}_0(q_1,k_2,q_2)\epsilon_2 k_2 u \\
&+ \frac{7}{2}\tilde{D}_{12}(q_1,k_2,q_2)\epsilon_2 k_2 u - 2\tilde{D}_{13}(q_1,k_2,q_2)\epsilon_2 k_2 u + 2d22\epsilon_2 k_2 u
\end{aligned}
$$

$$
\begin{aligned}
&- \quad 2\tilde{D}_{24}(q_1,k_2,q_2)\epsilon_2 k_2 u + 2\tilde{D}_{25}(q_1,k_2,q_2)\epsilon_2 k_2 u - 2\tilde{D}_{26}(q_1,k_2,q_2)\epsilon_2 k_2 u \\
&+ \quad 2\tilde{D}_{310}(q_1,k_2,q_2)\epsilon_2 k_2 u - 2\tilde{D}_{36}(q_1,k_2,q_2)\epsilon_2 k_2 u + \frac{3}{2}\tilde{D}_{0}(q_1,k_2,q_2)\epsilon_2 q_1 u \\
&+ \quad \tilde{D}_{11}(q_1,k_2,q_2)\epsilon_2 q_1 u + \frac{5}{2}\tilde{D}_{12}(q_1,k_2,q_2)\epsilon_2 q_1 u - 2\tilde{D}_{13}(q_1,k_2,q_2)\epsilon_2 q_1 u \\
&- \quad \tilde{D}_{21}(q_1,k_2,q_2)\epsilon_2 q_1 u + \tilde{D}_{24}(q_1,k_2,q_2)\epsilon_2 q_1 u - 2\tilde{D}_{34}(q_1,k_2,q_2)\epsilon_2 q_1 u \\
&+ \quad 2\tilde{D}_{35}(q_1,k_2,q_2)\epsilon_2 q_1 u + \frac{3}{2}\tilde{D}_{0}(q_1,k_2,q_2)\epsilon_2 q_2 u + \frac{3}{2}\tilde{D}_{12}(q_1,k_2,q_2)\epsilon_2 q_2 u \\
&- \quad 2\tilde{D}_{23}(q_1,k_2,q_2)\epsilon_2 q_2 u + 2\tilde{D}_{26}(q_1,k_2,q_2)\epsilon_2 q_2 u - 2\tilde{D}_{310}(q_1,k_2,q_2)\epsilon_2 q_2 u \\
&+ \quad 2\tilde{D}_{37}(q_1,k_2,q_2)\epsilon_2 q_2 u
\end{aligned} \qquad [B.19]
$$

$$
\begin{aligned}
\mathbf{Box}_2^{(3)} \;=\;& -12\tilde{D}_{27}(q_1,k_2,q_2)\epsilon_1 k_2 - 4\tilde{D}_{312}(q_1,k_2,q_2)\epsilon_1 k_2 - 6\tilde{D}_{27}(q_1,k_2,q_2)\epsilon_1 q_2 \\
&- \quad 4\tilde{D}_{313}(q_1,k_2,q_2)\epsilon_1 q_2 - 3\tilde{D}_{0}(q_1,k_2,q_2)\epsilon_1 k_2 q_2^2 - 7\tilde{D}_{12}(q_1,k_2,q_2)\epsilon_1 k_2 q_2^2 \\
&+ \quad 2\tilde{D}_{13}(q_1,k_2,q_2)\epsilon_1 k_2 q_2^2 - 2\tilde{D}_{22}(q_1,k_2,q_2)\epsilon_1 k_2 q_2^2 + 6\tilde{D}_{23}(q_1,k_2,q_2)\epsilon_1 k_2 q_2^2 \\
&- \quad 2\tilde{D}_{24}(q_1,k_2,q_2)\epsilon_1 k_2 q_2^2 + 4\tilde{D}_{25}(q_1,k_2,q_2)\epsilon_1 k_2 q_2^2 - 8\tilde{D}_{26}(q_1,k_2,q_2)\epsilon_1 k_2 q_2^2 \\
&- \quad 2\tilde{D}_{38}(q_1,k_2,q_2)\epsilon_1 k_2 q_2^2 + 2\tilde{D}_{39}(q_1,k_2,q_2)\epsilon_1 k_2 q_2^2 - \frac{3}{2}\tilde{D}_{0}(q_1,k_2,q_2)\epsilon_1 q_2 q_2^2 \\
&- \quad \frac{5}{2}\tilde{D}_{12}(q_1,k_2,q_2)\epsilon_1 q_2 q_2^2 - \tilde{D}_{13}(q_1,k_2,q_2)\epsilon_1 q_2 q_2^2 + 3\tilde{D}_{23}(q_1,k_2,q_2)\epsilon_1 q_2 q_2^2 \\
&- \quad \tilde{D}_{24}(q_1,k_2,q_2)\epsilon_1 q_2 q_2^2 + 2\tilde{D}_{25}(q_1,k_2,q_2)\epsilon_1 q_2 q_2^2 - 6\tilde{D}_{26}(q_1,k_2,q_2)\epsilon_1 q_2 q_2^2 \\
&+ \quad 2\tilde{D}_{33}(q_1,k_2,q_2)\epsilon_1 q_2 q_2^2 - 2\tilde{D}_{39}(q_1,k_2,q_2)\epsilon_1 q_2 q_2^2 + \frac{3}{2}\tilde{D}_{0}(q_1,k_2,q_2)\epsilon_1 k_2 t \\
&- \quad 4\tilde{D}_{11}(q_1,k_2,q_2)\epsilon_1 k_2 t + \frac{11}{2}\tilde{D}_{12}(q_1,k_2,q_2)\epsilon_1 k_2 t - 2\tilde{D}_{21}(q_1,k_2,q_2)\epsilon_1 k_2 t \\
&+ \quad 2\tilde{D}_{22}(q_1,k_2,q_2)\epsilon_1 k_2 t - 6\tilde{D}_{25}(q_1,k_2,q_2)\epsilon_1 k_2 t + 6\tilde{D}_{26}(q_1,k_2,q_2)\epsilon_1 k_2 t \\
&- \quad 2\tilde{D}_{310}(q_1,k_2,q_2)\epsilon_1 k_2 t + 2\tilde{D}_{38}(q_1,k_2,q_2)\epsilon_1 k_2 t - \frac{1}{2}\tilde{D}_{0}(q_1,k_2,q_2)\epsilon_1 q_2 t \\
&- \quad 3\tilde{D}_{11}(q_1,k_2,q_2)\epsilon_1 q_2 t + \frac{5}{2}\tilde{D}_{12}(q_1,k_2,q_2)\epsilon_1 q_2 t - \tilde{D}_{21}(q_1,k_2,q_2)\epsilon_1 q_2 t \\
&+ \quad \tilde{D}_{24}(q_1,k_2,q_2)\epsilon_1 q_2 t - 6\tilde{D}_{25}(q_1,k_2,q_2)\epsilon_1 q_2 t + 6\tilde{D}_{26}(q_1,k_2,q_2)\epsilon_1 q_2 t \\
&- \quad 2\tilde{D}_{37}(q_1,k_2,q_2)\epsilon_1 q_2 t + 2\tilde{D}_{39}(q_1,k_2,q_2)\epsilon_1 q_2 t + \frac{7}{2}\tilde{D}_{0}(q_1,k_2,q_2)\epsilon_1 k_2 u \\
&+ \quad \frac{23}{2}\tilde{D}_{12}(q_1,k_2,q_2)\epsilon_1 k_2 u - 6\tilde{D}_{13}(q_1,k_2,q_2)\epsilon_1 k_2 u - 2\tilde{D}_{21}(q_1,k_2,q_2)\epsilon_1 k_2 u \\
&+ \quad 2\tilde{D}_{22}(q_1,k_2,q_2)\epsilon_1 k_2 u + 10\tilde{D}_{24}(q_1,k_2,q_2)\epsilon_1 k_2 u - 6\tilde{D}_{25}(q_1,k_2,q_2)\epsilon_1 k_2 u \\
&- \quad 2\tilde{D}_{26}(q_1,k_2,q_2)\epsilon_1 k_2 u - 2\tilde{D}_{310}(q_1,k_2,q_2)\epsilon_1 k_2 u + 2\tilde{D}_{36}(q_1,k_2,q_2)\epsilon_1 k_2 u
\end{aligned}
$$

$$
\begin{aligned}
&+ \quad 2\tilde{D}_0(q_1,k_2,q_2)\epsilon_1 q_2 u - \tilde{D}_{11}(q_1,k_2,q_2)\epsilon_1 q_2 u + 5\tilde{D}_{12}(q_1,k_2,q_2)\epsilon_1 q_2 u \\
&- \quad \tilde{D}_{21}(q_1,k_2,q_2)\epsilon_1 q_2 u - 2\tilde{D}_{23}(q_1,k_2,q_2)\epsilon_1 q_2 u + 3\tilde{D}_{24}(q_1,k_2,q_2)\epsilon_1 q_2 u \\
&+ \quad 2\tilde{D}_{26}(q_1,k_2,q_2)\epsilon_1 q_2 u + 2\tilde{D}_{310}(q_1,k_2,q_2)\epsilon_1 q_2 u \\
&- \quad 2\tilde{D}_{37}(q_1,k_2,q_2)\epsilon_1 q_2 u \qquad \text{[B.20]}
\end{aligned}
$$

$$
\begin{aligned}
\mathbf{Box}_b^{(3)} &= (6\tilde{D}_{27}(q_1,k_2,q_2) + \frac{3}{2}\tilde{D}_0(q_1,k_2,q_2)q_2^2 + \frac{5}{2}\tilde{D}_{12}(q_1,k_2,q_2)q_2^2 \\
&- \tilde{D}_{13}(q_1,k_2,q_2)q_2^2 - 3\tilde{D}_{23}(q_1,k_2,q_2)q_2^2 + \tilde{D}_{24}(q_1,k_2,q_2)q_2^2 \\
&- 2\tilde{D}_{25}(q_1,k_2,q_2)q_2^2 + 4\tilde{D}_{26}(q_1,k_2,q_2)q_2^2 + \frac{1}{2}\tilde{D}_0(q_1,k_2,q_2)t \\
&+ 3\tilde{D}_{11}(q_1,k_2,q_2)t - \frac{5}{2}\tilde{D}_{12}(q_1,k_2,q_2)t + \tilde{D}_{21}(q_1,k_2,q_2)t \\
&- \tilde{D}_{24}(q_1,k_2,q_2)t + 4\tilde{D}_{25}(q_1,k_2,q_2)t - 4\tilde{D}_{26}(q_1,k_2,q_2)t - \frac{3}{2}\tilde{D}_0(q_1,k_2,q_2)u \\
&- \tilde{D}_{11}(q_1,k_2,q_2)u - \frac{9}{2}\tilde{D}_{12}(q_1,k_2,q_2)u + 4\tilde{D}_{13}(q_1,k_2,q_2)u \\
&+ \tilde{D}_{21}(q_1,k_2,q_2)u - 5\tilde{D}_{24}(q_1,k_2,q_2)u + 4\tilde{D}_{25}(q_1,k_2,q_2)u)/2 \qquad \text{[B.21]}
\end{aligned}
$$

$$
\begin{aligned}
\mathbf{Box}_1^{(1)} &= -(\epsilon_1 q_1(-8\tilde{D}_{27}(k_2,q_2,q_1) - 8\tilde{D}_{312}(k_2,q_2,q_1) - (\tilde{D}_{11}(k_2,q_2,q_1) \\
&- \tilde{D}_{12}(k_2,q_2,q_1) + \tilde{D}_{13}(k_2,q_2,q_1) - 4\tilde{D}_{22}(k_2,q_2,q_1) \\
&+ 4\tilde{D}_{24}(k_2,q_2,q_1))q_2^2 + \tilde{D}_{11}(k_2,q_2,q_1)s - \tilde{D}_{12}(k_2,q_2,q_1)s \\
&+ \tilde{D}_{13}(k_2,q_2,q_1)s - 4\tilde{D}_{22}(k_2,q_2,q_1)s + 4\tilde{D}_{24}(k_2,q_2,q_1)s \\
&+ \tilde{D}_{11}(k_2,q_2,q_1)t - \tilde{D}_{12}(k_2,q_2,q_1)t + \tilde{D}_{13}(k_2,q_2,q_1)t \\
&- 4\tilde{D}_{22}(k_2,q_2,q_1)t + 4\tilde{D}_{24}(k_2,q_2,q_1)t)) + \epsilon_2 q_1(8\tilde{D}_{27}(k_2,q_2,q_1) \\
&+ 8\tilde{D}_{313}(k_2,q_2,q_1) + (\tilde{D}_{11}(k_2,q_2,q_1) - \tilde{D}_{12}(k_2,q_2,q_1) \\
&+ \tilde{D}_{13}(k_2,q_2,q_1) - 4\tilde{D}_{22}(k_2,q_2,q_1) + 4\tilde{D}_{24}(k_2,q_2,q_1))q_2^2 \\
&- \tilde{D}_{11}(k_2,q_2,q_1)t - 3\tilde{D}_{12}(k_2,q_2,q_1)t + 3\tilde{D}_{13}(k_2,q_2,q_1)t \\
&- 4\tilde{D}_{24}(k_2,q_2,q_1)t + 4\tilde{D}_{26}(k_2,q_2,q_1)t) - \epsilon_2 k_2(16\tilde{D}_{311}(k_2,q_2,q_1) \\
&- 24\tilde{D}_{312}(k_2,q_2,q_1) - (\tilde{D}_{11}(k_2,q_2,q_1) - \tilde{D}_{12}(k_2,q_2,q_1)
\end{aligned}
$$

$$
\begin{aligned}
+ &\quad \tilde{D}_{13}(k_2,q_2,q_1) + 4\tilde{D}_{25}(k_2,q_2,q_1) - 4\tilde{D}_{26}(k_2,q_2,q_1) \\
- &\quad 8\tilde{D}_{310}(k_2,q_2,q_1) - 4\tilde{D}_{32}(k_2,q_2,q_1) - 4\tilde{D}_{34}(k_2,q_2,q_1) \\
+ &\quad 4\tilde{D}_{35}(k_2,q_2,q_1) + 8\tilde{D}_{36}(k_2,q_2,q_1) + 4\tilde{D}_{38}(k_2,q_2,q_1))q_2^2 \\
+ &\quad 5\tilde{D}_{11}(k_2,q_2,q_1)s - 5\tilde{D}_{12}(k_2,q_2,q_1)s + \tilde{D}_{13}(k_2,q_2,q_1)s \\
+ &\quad 4\tilde{D}_{21}(k_2,q_2,q_1)s - 4\tilde{D}_{24}(k_2,q_2,q_1)s + 4\tilde{D}_{25}(k_2,q_2,q_1)s \\
- &\quad 4\tilde{D}_{26}(k_2,q_2,q_1)s - 8\tilde{D}_{310}(k_2,q_2,q_1)s + 4\tilde{D}_{35}(k_2,q_2,q_1)s \\
+ &\quad 4\tilde{D}_{38}(k_2,q_2,q_1)s - 4\tilde{D}_{12}(k_2,q_2,q_1)t + 4\tilde{D}_{13}(k_2,q_2,q_1)t \\
+ &\quad 4\tilde{D}_{22}(k_2,q_2,q_1)t - 8\tilde{D}_{24}(k_2,q_2,q_1)t + 8\tilde{D}_{25}(k_2,q_2,q_1)t \\
- &\quad 4\tilde{D}_{26}(k_2,q_2,q_1)t - 4\tilde{D}_{310}(k_2,q_2,q_1)t - 4\tilde{D}_{34}(k_2,q_2,q_1)t \\
+ &\quad 4\tilde{D}_{35}(k_2,q_2,q_1)t + 4\tilde{D}_{36}(k_2,q_2,q_1)t)
\end{aligned}
\tag{B.22}
$$

$$
\begin{aligned}
\mathbf{Box}_2^{(1)} \quad = &\quad \epsilon_1 k_2(8\tilde{D}_{311}(k_2,q_2,q_1) - 24\tilde{D}_{313}(k_2,q_2,q_1) - (\tilde{D}_{11}(k_2,q_2,q_1) \\
+ &\quad 3\tilde{D}_{12}(k_2,q_2,q_1) - 3\tilde{D}_{13}(k_2,q_2,q_1) - 4\tilde{D}_{22}(k_2,q_2,q_1) \\
+ &\quad 8\tilde{D}_{24}(k_2,q_2,q_1) - 4\tilde{D}_{25}(k_2,q_2,q_1) + 4\tilde{D}_{310}(k_2,q_2,q_1) \\
- &\quad 4\tilde{D}_{37}(k_2,q_2,q_1) - 4\tilde{D}_{38}(k_2,q_2,q_1) + 4\tilde{D}_{39}(k_2,q_2,q_1))q_2^2 \\
- &\quad \tilde{D}_{11}(k_2,q_2,q_1)s + \tilde{D}_{12}(k_2,q_2,q_1)s - 5\tilde{D}_{13}(k_2,q_2,q_1)s \\
- &\quad 8\tilde{D}_{25}(k_2,q_2,q_1)s + 4\tilde{D}_{26}(k_2,q_2,q_1)s - 4\tilde{D}_{37}(k_2,q_2,q_1)s \\
+ &\quad 4\tilde{D}_{39}(k_2,q_2,q_1)s + 4\tilde{D}_{12}(k_2,q_2,q_1)t - 4\tilde{D}_{13}(k_2,q_2,q_1)t \\
- &\quad 4\tilde{D}_{23}(k_2,q_2,q_1)t + 4\tilde{D}_{24}(k_2,q_2,q_1)t - 4\tilde{D}_{25}(k_2,q_2,q_1)t \\
+ &\quad 4\tilde{D}_{26}(k_2,q_2,q_1)t + 4\tilde{D}_{310}(k_2,q_2,q_1)t - 4\tilde{D}_{37}(k_2,q_2,q_1)t) \\
- &\quad \epsilon_1 q_2(8\tilde{D}_{27}(k_2,q_2,q_1) - 8\tilde{D}_{312}(k_2,q_2,q_1) + 24\tilde{D}_{313}(k_2,q_2,q_1) \\
+ &\quad (\tilde{D}_{11}(k_2,q_2,q_1) + 3\tilde{D}_{12}(k_2,q_2,q_1) - 3\tilde{D}_{13}(k_2,q_2,q_1) \\
- &\quad 4\tilde{D}_{22}(k_2,q_2,q_1) + 8\tilde{D}_{24}(k_2,q_2,q_1) - 4\tilde{D}_{25}(k_2,q_2,q_1) \\
+ &\quad 4\tilde{D}_{310}(k_2,q_2,q_1) - 4\tilde{D}_{37}(k_2,q_2,q_1) - 4\tilde{D}_{38}(k_2,q_2,q_1) \\
+ &\quad 4\tilde{D}_{39}(k_2,q_2,q_1))q_2^2 + \tilde{D}_{11}(k_2,q_2,q_1)s - \tilde{D}_{12}(k_2,q_2,q_1)s
\end{aligned}
$$

$$
\begin{aligned}
&+ \quad 5\tilde{D}_{13}(k_2,q_2,q_1)s + 8\tilde{D}_{25}(k_2,q_2,q_1)s - 4\tilde{D}_{26}(k_2,q_2,q_1)s \\
&+ \quad 4\tilde{D}_{37}(k_2,q_2,q_1)s - 4\tilde{D}_{39}(k_2,q_2,q_1)s - \tilde{D}_{11}(k_2,q_2,q_1)t \\
&- \quad 7\tilde{D}_{12}(k_2,q_2,q_1)t + 7\tilde{D}_{13}(k_2,q_2,q_1)t + 4\tilde{D}_{23}(k_2,q_2,q_1)t \\
&- \quad 8\tilde{D}_{24}(k_2,q_2,q_1)t + 4\tilde{D}_{25}(k_2,q_2,q_1)t - 4\tilde{D}_{310}(k_2,q_2,q_1)t \\
&+ \quad 4\tilde{D}_{37}(k_2,q_2,q_1)t)
\end{aligned}
\tag{B.23}
$$

$$
\begin{aligned}
\mathbf{Box}_q^{(1)} \;=\;& 8\tilde{D}_{312}(k_2,q_2,q_1)\epsilon_1\epsilon_2 - 8\tilde{D}_{313}(k_2,q_2,q_1)\epsilon_1\epsilon_2 + 8\tilde{D}_{12}(k_2,q_2,q_1)\epsilon_1 k_2\epsilon_2 k_2 \\
-\;& 8\tilde{D}_{13}(k_2,q_2,q_1)\epsilon_1 k_2\epsilon_2 k_2 + 12\tilde{D}_{24}(k_2,q_2,q_1)\epsilon_1 k_2\epsilon_2 k_2 - 12\tilde{D}_{25}(k_2,q_2,q_1)\epsilon_1 k_2\epsilon_2 k_2 \\
+\;& 4\tilde{D}_{34}(k_2,q_2,q_1)\epsilon_1 k_2\epsilon_2 k_2 - 4\tilde{D}_{35}(k_2,q_2,q_1)\epsilon_1 k_2\epsilon_2 k_2 + \tilde{D}_{11}(k_2,q_2,q_1)\epsilon_1 q_2\epsilon_2 k_2 \\
+\;& 7\tilde{D}_{12}(k_2,q_2,q_1)\epsilon_1 q_2\epsilon_2 k_2 - 7\tilde{D}_{13}(k_2,q_2,q_1)\epsilon_1 q_2\epsilon_2 k_2 + 4\tilde{D}_{22}(k_2,q_2,q_1)\epsilon_1 q_2\epsilon_2 k_2 \\
+\;& 8\tilde{D}_{24}(k_2,q_2,q_1)\epsilon_1 q_2\epsilon_2 k_2 - 4\tilde{D}_{25}(k_2,q_2,q_1)\epsilon_1 q_2\epsilon_2 k_2 - 8\tilde{D}_{26}(k_2,q_2,q_1)\epsilon_1 q_2\epsilon_2 k_2 \\
-\;& 4\tilde{D}_{310}(k_2,q_2,q_1)\epsilon_1 q_2\epsilon_2 k_2 + 4\tilde{D}_{36}(k_2,q_2,q_1)\epsilon_1 q_2\epsilon_2 k_2 - \tilde{D}_{11}(k_2,q_2,q_1)\epsilon_1 k_2\epsilon_2 q_1 \\
+\;& \tilde{D}_{12}(k_2,q_2,q_1)\epsilon_1 k_2\epsilon_2 q_1 - \tilde{D}_{13}(k_2,q_2,q_1)\epsilon_1 k_2\epsilon_2 q_1 - 4\tilde{D}_{23}(k_2,q_2,q_1)\epsilon_1 k_2\epsilon_2 q_1 \\
-\;& 4\tilde{D}_{25}(k_2,q_2,q_1)\epsilon_1 k_2\epsilon_2 q_1 + 8\tilde{D}_{26}(k_2,q_2,q_1)\epsilon_1 k_2\epsilon_2 q_1 + 4\tilde{D}_{310}(k_2,q_2,q_1)\epsilon_1 k_2\epsilon_2 q_1 \\
-\;& 4\tilde{D}_{37}(k_2,q_2,q_1)\epsilon_1 k_2\epsilon_2 q_1 - 4\tilde{D}_{23}(k_2,q_2,q_1)\epsilon_1 q_2\epsilon_2 q_1 + 4\tilde{D}_{26}(k_2,q_2,q_1)\epsilon_1 q_2\epsilon_2 q_1 \\
+\;& 4\tilde{D}_{38}(k_2,q_2,q_1)\epsilon_1 q_2\epsilon_2 q_1 - 4\tilde{D}_{39}(k_2,q_2,q_1)\epsilon_1 q_2\epsilon_2 q_1 - \tilde{D}_{11}(k_2,q_2,q_1)\epsilon_1 k_2\epsilon_1 q_1 \\
+\;& 5\tilde{D}_{12}(k_2,q_2,q_1)\epsilon_1 k_2\epsilon_1 q_1 - 5\tilde{D}_{13}(k_2,q_2,q_1)\epsilon_1 k_2\epsilon_1 q_1 + 8\tilde{D}_{22}(k_2,q_2,q_1)\epsilon_1 k_2\epsilon_1 q_1 \\
-\;& 4\tilde{D}_{25}(k_2,q_2,q_1)\epsilon_1 k_2\epsilon_1 q_1 - 4\tilde{D}_{26}(k_2,q_2,q_1)\epsilon_1 k_2\epsilon_1 q_1 - 4\tilde{D}_{310}(k_2,q_2,q_1)\epsilon_1 k_2\epsilon_1 q_1 \\
+\;& 4\tilde{D}_{36}(k_2,q_2,q_1)\epsilon_1 k_2\epsilon_1 q_1 + 4\tilde{D}_{12}(k_2,q_2,q_1)\epsilon_1 q_2\epsilon_1 q_1 - 4\tilde{D}_{13}(k_2,q_2,q_1)\epsilon_1 q_2\epsilon_1 q_1 \\
+\;& 8\tilde{D}_{22}(k_2,q_2,q_1)\epsilon_1 q_2\epsilon_1 q_1 - 8\tilde{D}_{26}(k_2,q_2,q_1)\epsilon_1 q_2\epsilon_1 q_1 + 4\tilde{D}_{32}(k_2,q_2,q_1)\epsilon_1 q_2\epsilon_1 q_1 \\
-\;& 4\tilde{D}_{38}(k_2,q_2,q_1)\epsilon_1 q_2\epsilon_1 q_1 - 4\tilde{D}_{310}(k_2,q_2,q_1)\epsilon_1\epsilon_2 q_2^2 - 2\tilde{D}_{32}(k_2,q_2,q_1)\epsilon_1\epsilon_2 q_2^2 \\
+\;& 2\tilde{D}_{36}(k_2,q_2,q_1)\epsilon_1\epsilon_2 q_2^2 + 2\tilde{D}_{37}(k_2,q_2,q_1)\epsilon_1\epsilon_2 q_2^2 + 4\tilde{D}_{38}(k_2,q_2,q_1)\epsilon_1\epsilon_2 q_2^2 \\
-\;& 2\tilde{D}_{39}(k_2,q_2,q_1)\epsilon_1\epsilon_2 q_2^2 - \frac{1}{2}\tilde{D}_{11}(k_2,q_2,q_1)\epsilon_1\epsilon_2 s + \frac{1}{2}\tilde{D}_{12}(k_2,q_2,q_1)\epsilon_1\epsilon_2 s \\
-\;& \frac{1}{2}\tilde{D}_{13}(k_2,q_2,q_1)\epsilon_1\epsilon_2 s - 2\tilde{D}_{25}(k_2,q_2,q_1)\epsilon_1\epsilon_2 s + 2\tilde{D}_{26}(k_2,q_2,q_1)\epsilon_1\epsilon_2 s \\
+\;& 2\tilde{D}_{310}(k_2,q_2,q_1)\epsilon_1\epsilon_2 s - 2\tilde{D}_{37}(k_2,q_2,q_1)\epsilon_1\epsilon_2 s - 2\tilde{D}_{38}(k_2,q_2,q_1)\epsilon_1\epsilon_2 s
\end{aligned}
$$

$$
\begin{aligned}
+ &\quad 2\tilde{D}_{39}(k_2,q_2,q_1)\epsilon_1\epsilon_2 s - 2\tilde{D}_{22}(k_2,q_2,q_1)\epsilon_1\epsilon_2 t - 2\tilde{D}_{23}(k_2,q_2,q_1)\epsilon_1\epsilon_2 t \\
+ &\quad 4\tilde{D}_{26}(k_2,q_2,q_1)\epsilon_1\epsilon_2 t + 4\tilde{D}_{310}(k_2,q_2,q_1)\epsilon_1\epsilon_2 t - 2\tilde{D}_{36}(k_2,q_2,q_1)\epsilon_1\epsilon_2 t \\
- &\quad 2\tilde{D}_{37}(k_2,q_2,q_1)\epsilon_1\epsilon_2 t
\end{aligned}
\qquad [B.24]
$$

$$
\begin{aligned}
\mathbf{Box}_b^{(1)} &= -4\tilde{D}_{27}(k_2,q_2,q_1) - 12\tilde{D}_{312}(k_2,q_2,q_1) + 12\tilde{D}_{313}(k_2,q_2,q_1) \\
&+ 4\tilde{D}_{310}(k_2,q_2,q_1)q_2^2 + 2\tilde{D}_{32}(k_2,q_2,q_1)q_2^2 - 2\tilde{D}_{36}(k_2,q_2,q_1)q_2^2 \\
&- 2\tilde{D}_{37}(k_2,q_2,q_1)q_2^2 - 4\tilde{D}_{38}(k_2,q_2,q_1)q_2^2 + 2\tilde{D}_{39}(k_2,q_2,q_1)q_2^2 \\
&- 2\tilde{D}_{0}(k_2,q_2,q_1)s - \tilde{D}_{11}(k_2,q_2,q_1)s - \tilde{D}_{12}(k_2,q_2,q_1)s \\
&+ \tilde{D}_{13}(k_2,q_2,q_1)s + 2\tilde{D}_{25}(k_2,q_2,q_1)s - 2\tilde{D}_{26}(k_2,q_2,q_1)s \\
&- 2\tilde{D}_{310}(k_2,q_2,q_1)s + 2\tilde{D}_{37}(k_2,q_2,q_1)s + 2\tilde{D}_{38}(k_2,q_2,q_1)s \\
&- 2\tilde{D}_{39}(k_2,q_2,q_1)s + 2\tilde{D}_{22}(k_2,q_2,q_1)t + 2\tilde{D}_{23}(k_2,q_2,q_1)t \\
&- 4\tilde{D}_{26}(k_2,q_2,q_1)t - 4\tilde{D}_{310}(k_2,q_2,q_1)t + 2\tilde{D}_{36}(k_2,q_2,q_1)t \\
&+ 2\tilde{D}_{37}(k_2,q_2,q_1)t
\end{aligned}
\qquad [B.25]
$$

$$
\begin{aligned}
\mathbf{Box}_1^{(2)} &= -(\epsilon_2 q_1(8\tilde{D}_{27}(k_2,q_1,q_2) - 8\tilde{D}_{312}(k_2,q_1,q_2) + 24\tilde{D}_{313}(k_2,q_1,q_2) \\
&- 4(\tilde{D}_{23}(k_2,q_1,q_2) - \tilde{D}_{26}(k_2,q_1,q_2) + \tilde{D}_{33}(k_2,q_1,q_2) \\
&- \tilde{D}_{39}(k_2,q_1,q_2))q_2^2 + \tilde{D}_{11}(k_2,q_1,q_2)s - \tilde{D}_{12}(k_2,q_1,q_2)s \\
&+ 5\tilde{D}_{13}(k_2,q_1,q_2)s + 8\tilde{D}_{25}(k_2,q_1,q_2)s - 4\tilde{D}_{26}(k_2,q_1,q_2)s \\
&+ 4\tilde{D}_{37}(k_2,q_1,q_2)s - 4\tilde{D}_{39}(k_2,q_1,q_2)s - \tilde{D}_{11}(k_2,q_1,q_2)u \\
&- 7\tilde{D}_{12}(k_2,q_1,q_2)u + 7\tilde{D}_{13}(k_2,q_1,q_2)u + 4\tilde{D}_{23}(k_2,q_1,q_2)u \\
&- 8\tilde{D}_{24}(k_2,q_1,q_2)u + 4\tilde{D}_{25}(k_2,q_1,q_2)u - 4\tilde{D}_{310}(k_2,q_1,q_2)u \\
&+ 4\tilde{D}_{37}(k_2,q_1,q_2)u)) - \epsilon_2 q_2(8\tilde{D}_{27}(k_2,q_1,q_2) + 16\tilde{D}_{313}(k_2,q_1,q_2) \\
&- 4(\tilde{D}_{23}(k_2,q_1,q_2) - \tilde{D}_{26}(k_2,q_1,q_2) + \tilde{D}_{33}(k_2,q_1,q_2) \\
&- \tilde{D}_{39}(k_2,q_1,q_2))q_2^2 + 4\tilde{D}_{13}(k_2,q_1,q_2)s + 4\tilde{D}_{23}(k_2,q_1,q_2)s \\
&+ 4\tilde{D}_{25}(k_2,q_1,q_2)s - 4\tilde{D}_{26}(k_2,q_1,q_2)s + 4\tilde{D}_{37}(k_2,q_1,q_2)s
\end{aligned}
$$

$$
\begin{aligned}
&- \quad 4\tilde{D}_{39}(k_2,q_1,q_2)s - \tilde{D}_{11}(k_2,q_1,q_2)u - 3\tilde{D}_{12}(k_2,q_1,q_2)u \\
&+ \quad 3\tilde{D}_{13}(k_2,q_1,q_2)u + 8\tilde{D}_{23}(k_2,q_1,q_2)u - 4\tilde{D}_{24}(k_2,q_1,q_2)u \\
&- \quad 4\tilde{D}_{26}(k_2,q_1,q_2)u - 4\tilde{D}_{310}(k_2,q_1,q_2)u + 4\tilde{D}_{37}(k_2,q_1,q_2)u) \\
&- \quad \epsilon_2 k_2(-8\tilde{D}_{311}(k_2,q_1,q_2) + 24\tilde{D}_{313}(k_2,q_1,q_2) - (\tilde{D}_{11}(k_2,q_1,q_2) \\
&- \quad \tilde{D}_{12}(k_2,q_1,q_2) + \tilde{D}_{13}(k_2,q_1,q_2) + 4\tilde{D}_{25}(k_2,q_1,q_2) \\
&- \quad 4\tilde{D}_{26}(k_2,q_1,q_2) + 4\tilde{D}_{33}(k_2,q_1,q_2) - 4\tilde{D}_{39}(k_2,q_1,q_2))q_2^2 \\
&+ \quad \tilde{D}_{11}(k_2,q_1,q_2)s - \tilde{D}_{12}(k_2,q_1,q_2)s + 5\tilde{D}_{13}(k_2,q_1,q_2)s \\
&+ \quad 8\tilde{D}_{25}(k_2,q_1,q_2)s - 4\tilde{D}_{26}(k_2,q_1,q_2)s + 4\tilde{D}_{37}(k_2,q_1,q_2)s \\
&- \quad 4\tilde{D}_{39}(k_2,q_1,q_2)s - 4\tilde{D}_{12}(k_2,q_1,q_2)u + 4\tilde{D}_{13}(k_2,q_1,q_2)u \\
&+ \quad 4\tilde{D}_{23}(k_2,q_1,q_2)u - 4\tilde{D}_{24}(k_2,q_1,q_2)u + 4\tilde{D}_{25}(k_2,q_1,q_2)u \\
&- \quad 4\tilde{D}_{26}(k_2,q_1,q_2)u - 4\tilde{D}_{310}(k_2,q_1,q_2)u + 4\tilde{D}_{37}(k_2,q_1,q_2)u) \qquad \text{[B.26]}
\end{aligned}
$$

$$
\begin{aligned}
\mathbf{Box}_2^{(2)} \quad &= \quad -(\epsilon_1 q_2(-8\tilde{D}_{27}(k_2,q_1,q_2) - 8\tilde{D}_{313}(k_2,q_1,q_2) + (\tilde{D}_{11}(k_2,q_1,q_2) \\
&+ \quad 3\tilde{D}_{12}(k_2,q_1,q_2) - 3\tilde{D}_{13}(k_2,q_1,q_2) + 4\tilde{D}_{24}(k_2,q_1,q_2) \\
&- \quad 4\tilde{D}_{26}(k_2,q_1,q_2))u)) - \epsilon_1 k_2(16\tilde{D}_{311}(k_2,q_1,q_2) - 24\tilde{D}_{312}(k_2,q_1,q_2) \\
&+ \quad (\tilde{D}_{11}(k_2,q_1,q_2) + 3\tilde{D}_{12}(k_2,q_1,q_2) - 3\tilde{D}_{13}(k_2,q_1,q_2) \\
&- \quad 4\tilde{D}_{23}(k_2,q_1,q_2) + 4\tilde{D}_{24}(k_2,q_1,q_2) + 4\tilde{D}_{310}(k_2,q_1,q_2) \\
&- \quad 4\tilde{D}_{37}(k_2,q_1,q_2) - 4\tilde{D}_{38}(k_2,q_1,q_2) + 4\tilde{D}_{39}(k_2,q_1,q_2))q_2^2 \\
&+ \quad 5\tilde{D}_{11}(k_2,q_1,q_2)s - 5\tilde{D}_{12}(k_2,q_1,q_2)s + \tilde{D}_{13}(k_2,q_1,q_2)s \\
&+ \quad 4\tilde{D}_{21}(k_2,q_1,q_2)s - 4\tilde{D}_{24}(k_2,q_1,q_2)s + 4\tilde{D}_{25}(k_2,q_1,q_2)s \\
&- \quad 4\tilde{D}_{26}(k_2,q_1,q_2)s - 8\tilde{D}_{310}(k_2,q_1,q_2)s + 4\tilde{D}_{35}(k_2,q_1,q_2)s \\
&+ \quad 4\tilde{D}_{38}(k_2,q_1,q_2)s - 4\tilde{D}_{12}(k_2,q_1,q_2)u + 4\tilde{D}_{13}(k_2,q_1,q_2)u \\
&+ \quad 4\tilde{D}_{22}(k_2,q_1,q_2)u - 8\tilde{D}_{24}(k_2,q_1,q_2)u + 8\tilde{D}_{25}(k_2,q_1,q_2)u \\
&- \quad 4\tilde{D}_{26}(k_2,q_1,q_2)u - 4\tilde{D}_{310}(k_2,q_1,q_2)u - 4\tilde{D}_{34}(k_2,q_1,q_2)u \\
&+ \quad 4\tilde{D}_{35}(k_2,q_1,q_2)u + 4\tilde{D}_{36}(k_2,q_1,q_2)u) \qquad \text{[B.27]}
\end{aligned}
$$

$$
\begin{aligned}
\mathbf{Box}_q^{(2)} &= -8\tilde{D}_{312}(k_2,q_1,q_2)\epsilon_1\epsilon_2+8\tilde{D}_{313}(k_2,q_1,q_2)\epsilon_1\epsilon_2-8\tilde{D}_{12}(k_2,q_1,q_2)\epsilon_1k_2\epsilon_2k_2\\
&+ 8\tilde{D}_{13}(k_2,q_1,q_2)\epsilon_1k_2\epsilon_2k_2-12\tilde{D}_{24}(k_2,q_1,q_2)\epsilon_1k_2\epsilon_2k_2+12\tilde{D}_{25}(k_2,q_1,q_2)\epsilon_1k_2\epsilon_2k_2\\
&- 4\tilde{D}_{34}(k_2,q_1,q_2)\epsilon_1k_2\epsilon_2k_2+4\tilde{D}_{35}(k_2,q_1,q_2)\epsilon_1k_2\epsilon_2k_2+\tilde{D}_{11}(k_2,q_1,q_2)\epsilon_1q_2\epsilon_2k_2\\
&- \tilde{D}_{12}(k_2,q_1,q_2)\epsilon_1q_2\epsilon_2k_2+\tilde{D}_{13}(k_2,q_1,q_2)\epsilon_1q_2\epsilon_2k_2+4\tilde{D}_{23}(k_2,q_1,q_2)\epsilon_1q_2\epsilon_2k_2\\
&+ 4\tilde{D}_{25}(k_2,q_1,q_2)\epsilon_1q_2\epsilon_2k_2-8\tilde{D}_{26}(k_2,q_1,q_2)\epsilon_1q_2\epsilon_2k_2-4\tilde{D}_{310}(k_2,q_1,q_2)\epsilon_1q_2\epsilon_2k_2\\
&+ 4\tilde{D}_{37}(k_2,q_1,q_2)\epsilon_1q_2\epsilon_2k_2-\tilde{D}_{11}(k_2,q_1,q_2)\epsilon_1k_2\epsilon_2q_1-7\tilde{D}_{12}(k_2,q_1,q_2)\epsilon_1k_2\epsilon_2q_1\\
&+ 7\tilde{D}_{13}(k_2,q_1,q_2)\epsilon_1k_2\epsilon_2q_1-4\tilde{D}_{22}(k_2,q_1,q_2)\epsilon_1k_2\epsilon_2q_1-8\tilde{D}_{24}(k_2,q_1,q_2)\epsilon_1k_2\epsilon_2q_1\\
&+ 4\tilde{D}_{25}(k_2,q_1,q_2)\epsilon_1k_2\epsilon_2q_1+8\tilde{D}_{26}(k_2,q_1,q_2)\epsilon_1k_2\epsilon_2q_1+4\tilde{D}_{310}(k_2,q_1,q_2)\epsilon_1k_2\epsilon_2q_1\\
&- 4\tilde{D}_{36}(k_2,q_1,q_2)\epsilon_1k_2\epsilon_2q_1+4\tilde{D}_{23}(k_2,q_1,q_2)\epsilon_1q_2\epsilon_2q_1-4\tilde{D}_{26}(k_2,q_1,q_2)\epsilon_1q_2\epsilon_2q_1\\
&- 4\tilde{D}_{38}(k_2,q_1,q_2)\epsilon_1q_2\epsilon_2q_1+4\tilde{D}_{39}(k_2,q_1,q_2)\epsilon_1q_2\epsilon_2q_1-\tilde{D}_{11}(k_2,q_1,q_2)\epsilon_1k_2\epsilon_2q_2\\
&- 3\tilde{D}_{12}(k_2,q_1,q_2)\epsilon_1k_2\epsilon_2q_2+3\tilde{D}_{13}(k_2,q_1,q_2)\epsilon_1k_2\epsilon_2q_2+8\tilde{D}_{23}(k_2,q_1,q_2)\epsilon_1k_2\epsilon_2q_2\\
&- 4\tilde{D}_{24}(k_2,q_1,q_2)\epsilon_1k_2\epsilon_2q_2-4\tilde{D}_{26}(k_2,q_1,q_2)\epsilon_1k_2\epsilon_2q_2-4\tilde{D}_{310}(k_2,q_1,q_2)\epsilon_1k_2\epsilon_2q_2\\
&+ 4\tilde{D}_{37}(k_2,q_1,q_2)\epsilon_1k_2\epsilon_2q_2+4\tilde{D}_{23}(k_2,q_1,q_2)\epsilon_1q_2\epsilon_2q_2-4\tilde{D}_{26}(k_2,q_1,q_2)\epsilon_1q_2\epsilon_2q_2\\
&+ 4\tilde{D}_{33}(k_2,q_1,q_2)\epsilon_1q_2\epsilon_2q_2-4\tilde{D}_{39}(k_2,q_1,q_2)\epsilon_1q_2\epsilon_2q_2-2\tilde{D}_{33}(k_2,q_1,q_2)\epsilon_1\epsilon_2q_2^2\\
&- 2\tilde{D}_{38}(k_2,q_1,q_2)\epsilon_1\epsilon_2q_2^2+4\tilde{D}_{39}(k_2,q_1,q_2)\epsilon_1\epsilon_2q_2^2+\frac{1}{2}\tilde{D}_{11}(k_2,q_1,q_2)\epsilon_1\epsilon_2s\\
&- \frac{1}{2}\tilde{D}_{12}(k_2,q_1,q_2)\epsilon_1\epsilon_2s+\frac{1}{2}\tilde{D}_{13}(k_2,q_1,q_2)\epsilon_1\epsilon_2s+2\tilde{D}_{25}(k_2,q_1,q_2)\epsilon_1\epsilon_2s\\
&- 2\tilde{D}_{26}(k_2,q_1,q_2)\epsilon_1\epsilon_2s-2\tilde{D}_{310}(k_2,q_1,q_2)\epsilon_1\epsilon_2s+2\tilde{D}_{37}(k_2,q_1,q_2)\epsilon_1\epsilon_2s\\
&+ 2\tilde{D}_{38}(k_2,q_1,q_2)\epsilon_1\epsilon_2s-2\tilde{D}_{39}(k_2,q_1,q_2)\epsilon_1\epsilon_2s+2\tilde{D}_{22}(k_2,q_1,q_2)\epsilon_1\epsilon_2u\\
&+ 2\tilde{D}_{23}(k_2,q_1,q_2)\epsilon_1\epsilon_2u-4\tilde{D}_{26}(k_2,q_1,q_2)\epsilon_1\epsilon_2u-4\tilde{D}_{310}(k_2,q_1,q_2)\epsilon_1\epsilon_2u\\
&+ 2\tilde{D}_{36}(k_2,q_1,q_2)\epsilon_1\epsilon_2u+2\tilde{D}_{37}(k_2,q_1,q_2)\epsilon_1\epsilon_2u
\end{aligned}
\tag{B.28}
$$

$$
\begin{aligned}
\mathbf{Box}_b^{(2)} &= -4\tilde{D}_{27}(k_2,q_1,q_2)-12\tilde{D}_{312}(k_2,q_1,q_2)+12\tilde{D}_{313}(k_2,q_1,q_2)\\
&- 2\tilde{D}_{33}(k_2,q_1,q_2)q_2^2-2\tilde{D}_{38}(k_2,q_1,q_2)q_2^2+4\tilde{D}_{39}(k_2,q_1,q_2)q_2^2\\
&- 2\tilde{D}_{0}(k_2,q_1,q_2)s-\tilde{D}_{11}(k_2,q_1,q_2)s-\tilde{D}_{12}(k_2,q_1,q_2)s\\
&+ \tilde{D}_{13}(k_2,q_1,q_2)s+2\tilde{D}_{25}(k_2,q_1,q_2)s-2\tilde{D}_{26}(k_2,q_1,q_2)s
\end{aligned}
$$

$$
\begin{aligned}
- & \quad 2\tilde{D}_{310}(k_2,q_1,q_2)s + 2\tilde{D}_{37}(k_2,q_1,q_2)s + 2\tilde{D}_{38}(k_2,q_1,q_2)s \\
- & \quad 2\tilde{D}_{39}(k_2,q_1,q_2)s + 2\tilde{D}_{22}(k_2,q_1,q_2)u + 2\tilde{D}_{23}(k_2,q_1,q_2)u \\
- & \quad 4\tilde{D}_{26}(k_2,q_1,q_2)u - 4\tilde{D}_{310}(k_2,q_1,q_2)u + 2\tilde{D}_{36}(k_2,q_1,q_2)u \\
+ & \quad 2\tilde{D}_{37}(k_2,q_1,q_2)u \qquad \text{[B.29]}
\end{aligned}
$$

Appendix C: Scalar integrals

In this appendix all relevant scalar integrals used for the one-loop QCD calculations are given. All scalar integrals are computed in $d = 4 - 2\epsilon$ space-time dimensions.

For virtual corrections considered in this thesis, only the one-mass box [55, 56], is needed. Specifically, we need the case in which $k_1^2 = k_2^2 = q_1^2 = 0$ and $q_2^2 \neq 0$. The one-mass box in the unphysical region, $-s = -(k_1 - k_2)^2 > 0, -t = -(k_1 - q_1)^2 > 0, -q_2^2 > 0$ is

$$\begin{aligned} D_0(k_2, q_2, q_1) &= \int \frac{d^d k}{i\pi^2} \frac{1}{[k^2][(k-k_2)^2][(k-k_2-q_2)^2][(k-k_2-q_2-q_1)^2]} \\ &= \pi^{-\epsilon}(\mu^2)^{-\epsilon}\Gamma(1+\epsilon) \\ &\cdot \left\{ \frac{2}{st}\frac{1}{\epsilon^2} + \frac{2}{st}\frac{1}{\epsilon}\left[\ln\left(\frac{-q_2^2}{\mu^2}\right) - \ln\left(\frac{-s}{\mu^2}\right) - \ln\left(\frac{-t}{\mu^2}\right)\right] + \tilde{D}_0(k_2, q_2, q_1) + \mathcal{O}(\epsilon)\right\} \end{aligned} \tag{C.1}$$

where

$$\begin{aligned} \tilde{D}_0(k_2, q_2, q_1) &= \frac{1}{st}\left[\ln^2\left(\frac{-s}{\mu^2}\right) + \ln^2\left(\frac{-t}{\mu^2}\right) - \ln^2\left(\frac{-q_2^2}{\mu^2}\right)\right. \\ &- \left. \ln\left(\frac{-s}{\mu^2}\right) + \ln\left(\frac{-t}{\mu^2}\right) - 2\,\mathrm{Li}_2\left(1 - \frac{q_2^2}{t}\right) - 2\,\mathrm{Li}_2\left(1 - \frac{q_2^2}{s}\right) - \frac{2\pi^2}{3}\right]. \end{aligned} \tag{C.2}$$

For the present application, the invariant, q_2^2 is always space-like while the Mandelstam invariants, s and t, may either be time-like or space-like. Results for physical kinematic regions can be obtained by analytic continuation by replacing the time-like invariant by $t \to t + i0^+$ or $s \to s + i0^+$.

In addition, to the one-mass box, one needs expressions for the 3-point and 2-point scalar integrals in $d = 4 - 2\epsilon$ space-time dimensions. For the 3-point scalar integral

$$C_0(p_1^2, p_2^2, (p_1+p_2)^2) = \int \frac{d^d k}{i\pi^2} \frac{1}{[-k^2 - i0^+][-(k+p_1)^2 - i0^+][-(k+p_1+p_2)^2 - i0^+]} \tag{C.3}$$

two cases are needed.

a. The two-mass triangle. Either, $p_1^2 = 0$ or $p_2^2 = 0$ and $p_3^2 = (p_1+p_2)^2 \neq 0$.

$$\begin{aligned} C_0(p_1^2, 0, p_3^2) &= \pi^{-\epsilon}(\mu^2)^{-\epsilon}\Gamma(1+\epsilon) \\ &\cdot \left\{\frac{1}{-p_3^2 - p_1^2}(\ln(-p_3^2/\mu^2) - \ln(-p_1^2/\mu^2))\frac{1}{\epsilon} + \tilde{C}_0(p_1^2, 0, p_3^2) + \mathcal{O}(\epsilon)\right\} \end{aligned} \tag{C.4}$$

$$\tilde{C}_0(p_1^2, 0, p_3^2) = \frac{1}{2}\frac{1}{-p_3^2 - p_1^2}\left(\ln^2(-p_1^2/\mu^2) - \ln^2(-p_3^2/\mu^2)\right) \tag{C.5}$$

b. The one-mass triangle. The case for which $p_1^2 = p_2^2 = 0$ and $p_3^2 = (p_1 + p_2)^2 \neq 0$.

$$\begin{aligned} C_0(0,0,p_3^2) &= \pi^{-\epsilon}(\mu^2)^{-\epsilon}\Gamma(1+\epsilon)\left\{\frac{1}{-p_3^2}\frac{1}{\epsilon^2}\right. \\ &- \left.\frac{1}{-p_3^2}\ln(-p_3^2/\mu^2)\frac{1}{\epsilon} + \tilde{C}_0(0,0,p_3^2) + \mathcal{O}(\epsilon)\right\} \end{aligned} \quad \text{[C.6]}$$

$$\tilde{C}_0(0,0,p_3^2) = -\frac{\pi^2}{6}\frac{1}{-p_3^2} + \frac{1}{-p_3^2}\frac{1}{2}\ln^2(-p_3^2/\mu^2) \quad \text{[C.7]}$$

The scalar 2-point integral is

$$\begin{aligned} B_0(q^2) &= \int \frac{d^dk}{i\pi^2}\frac{1}{[-k^2 - i0^+][-(k-q)^2 - i0^+]} \\ &= \pi^{-\epsilon}(\mu^2)^{-\epsilon}\Gamma(1+\epsilon)\left[\frac{1}{\epsilon} + \tilde{B}_0(q^2) + \mathcal{O}(\epsilon)\right] \end{aligned} \quad \text{[C.8]}$$

with

$$\tilde{B}_0(q^2) = 2 - \ln\frac{-q^2 - i0^+}{\mu^2}. \quad \text{[C.9]}$$

BIBLIOGRAPHY

[1] S. Glashow, Nucl. Phys. 22 (1961) 579; S. Weinberg, Phys. Rev. Lett. 19 (1967) 1264; A. Salam, in “Elementary Particle Theory”, ed. N. Svartholm, Almqvist and Wiksells, Stockholm (1969) p. 367.

[2] C.N. Yang and R. Mills, Phys. Rev. 96 (1954) 191.

[3] M. Gell-Mann, Phys. Lett. 8 (1964) 214; G. Zweig, CERN-Report 8182/TH401 (1964); H. Fritzsch, M. Gell-Mann and H. Leutwyler, Phys. Lett. B47 (1973) 365; D. Gross and F. Wilczek, Phys. Rev. Lett. 30 (1973) 1343; H.D. Politzer, Phys. Rev. Lett. 30 (1973) 1346; G. ’t Hooft, Marseille Conference on Yang–Mills fields (1972).

[4] P.W. Higgs, Phys. Rev. Lett. 13 (1964) 508; *ibid.* Phys. Rev. 145 (1966) 1156; F. Englert and R. Brout, Phys. Rev. Lett. 13 (1964) 321; G.S. Guralnik, C.R. Hagen and T. Kibble, Phys. Rev. Lett. 13 (1965) 585; T. Kibble, Phys. Rev. 155 (1967) 1554.

[5] S.L. Adler and W.A. Bardeen, Phys. Rev. 182 (1969) 1517; R. Jackiw, Lectures on “Current Algebra and its Applications”, Princeton University Press, 1972.

[6] C. Bouchiat, J. Iliopoulos and Ph. Meyer, Phys. Lett. 38B (1972) 519.

[7] G. ’t Hooft, Nucl. Phys. B33 (1971) 173; *ibid.* Nucl. Phys. B35 (1971) 167; G. ’t Hooft and M. Veltman, Nucl. Phys. B44 (1972) 189.

[8] A. Djouadi, N. Spira and P. Zerwas, Phys. Lett. **B264**, 440 (1991); M. Spira, A. Djouadi, D. Graudenz and P.M. Zerwas, Nucl. Phys. **B453**, 17 (1995); S. Dawson, Nucl. Phys. **B359**, 283 (1991); S. Catani, D. de Florian, M. Grazzini and P. Nason, in arXiv:hep-ph/0204316.

[9] S. Catani, D. de Florian and M. Grazzini, JHEP **0105**, 025 (2001) [arXiv:hep-ph/0102227]; R. Harlander and W. Kilgore, Phys. Rev. **D64**, 013015 (2001) [arXiv:hep-ph/0102241]; R. Harlander and W. Kilgore, Phys. Rev. Lett. **88**, 201801 (2002) [arXiv:hep-ph/0201206]; C. Anastasiou and K. Melnikov, Nucl. Phys. **B646**, 220 (2002) [arXiv:[hep-ph/0207004]; V. Ravindran, J. Smith and W.L. van Neerven, arXiv:hep-ph/0302135.

[10] T. Figy, C. Oleari and D. Zeppenfeld, Phys. Rev. D **68**, 073005 (2003) [arXiv:hep-ph/0306109].

[11] E. L. Berger and J. Campbell, Phys. Rev. D **70**, 073011 (2004) [arXiv:hep-ph/0403194].

[12] T. Han, G. Valencia and S. Willenbrock, Phys. Rev. Lett. **69**, 3274 (1992) [arXiv:hep-ph/9206246].

[13] T. Figy and D. Zeppenfeld, Phys. Lett. B **591**, 297 (2004) [arXiv:hep-ph/0403297].

[14] J. D. Bjorken, Phys. Rev. D **47**, 101 (1993).

[15] D. L. Rainwater, R. Szalapski and D. Zeppenfeld, Phys. Rev. D **54**, 6680 (1996) [arXiv:hep-ph/9605444].

[16] V. D. Barger, R. J. N. Phillips and D. Zeppenfeld, Phys. Lett. B **346**, 106 (1995) [arXiv:hep-ph/9412276].

[17] N. Kauer, T. Plehn, D. L. Rainwater and D. Zeppenfeld, Phys. Lett. B **503**, 113 (2001) [arXiv:hep-ph/0012351].

[18] V. D. Barger, K. m. Cheung, T. Han and D. Zeppenfeld, Phys. Rev. D **48**, 5433 (1993) [arXiv:hep-ph/9305277].

[19] V. D. Barger, K. m. Cheung, T. Han and D. Zeppenfeld, Phys. Rev. D **44**, 2701 (1991) [Erratum-ibid. D **48**, 5444 (1993)].

[20] A. Duff and D. Zeppenfeld, Phys. Rev. D **50**, 3204 (1994) [arXiv:hep-ph/9312357].

[21] S. Catani and M. H. Seymour, Nucl. Phys. B **485**, 291 (1997) [Erratum-ibid. B **510**, 503 (1997)] [arXiv:hep-ph/9605323].

[22] G. L. Bayatian *et al.*, CMS Technical Proposal, report CERN/LHCC/94-38x (1994); R. Kinnunen and D. Denegri, CMS NOTE 1997/057; R. Kinnunen and A. Nikitenko, CMS TN/97-106; R. Kinnunen and D. Denegri, arXiv:hep-ph/9907291; V. Drollinger, T. Müller and D. Denegri, arXiv:hep-ph/0111312.

[23] ATLAS Collaboration, ATLAS TDR, report CERN/LHCC/99-15 (1999); E. Richter-Was and M. Sapinski, Acta Phys. Polon. B **30**, 1001 (1999); B. P. Kersevan and E. Richter-Was, Eur. Phys. J. C **25**, 379 (2002) [arXiv:hep-ph/0203148].

[24] D. Zeppenfeld, R. Kinnunen, A. Nikitenko and E. Richter-Was, Phys. Rev. **D62**, 013009 (2000) [arXiv:hep-ph/0002036]; D. Zeppenfeld, in *Proc. of the APS/DPF/DPB Summer Study on the Future of Particle Physics (Snowmass 2001)* ed. N. Graf, eConf **C010630**, P123 (2001) [arXiv:hep-ph/0203123]; A. Belyaev and L. Reina, JHEP **0208**, 041 (2002) [arXiv:hep-ph/0205270].

[25] D. Rainwater, D. Zeppenfeld and K. Hagiwara, Phys. Rev. D **59**, 014037 (1999) [arXiv:hep-ph/9808468]; T. Plehn, D. Rainwater and D. Zeppenfeld, Phys. Rev. **D61**, 093005 (2000) [arXiv:hep-ph/9911385]; S. Asai et al., ATL-PHYS-2003-005.

[26] C. M. Buttar, R. S. Harper and K. Jakobs, ATL-PHYS-2002-033; K. Cranmer et al., ATL-PHYS-2003-002 and ATL-PHYS-2003-007; S. Asai et al., ATL-PHYS-2003-005.

[27] D. L. Rainwater and D. Zeppenfeld, Phys. Rev. D **60**, 113004 (1999) [Erratum-ibid. D **61**, 099901 (2000)] [arXiv:hep-ph/9906218].

[28] D. Rainwater and D. Zeppenfeld, JHEP **9712**, 005 (1997) [arXiv:hep-ph/9712271]. K. Cranmer, B. Mellado, W. Quayle and S. L. Wu, arXiv:hep-ph/0401088.

[29] O. J. Eboli and D. Zeppenfeld, Phys. Lett. B **495**, 147 (2000) [arXiv:hep-ph/0009158]; B. Di Girolamo, A. Nikitenko, L. Neukermans, K. Mazumdar and D. Zeppenfeld, in arXiv:hep-ph/0203056.

[30] K. Hagiwara and D. Zeppenfeld, Nucl. Phys. B **274**, 1 (1986); K. Hagiwara and D. Zeppenfeld, Nucl. Phys. B **313**, 560 (1989).

[31] G. P. Lepage, J. Comput. Phys. **27**, 192 (1978).

[32] M. Spira, Fortsch. Phys. **46**, 203 (1998) [arXiv:hep-ph/9705337].

[33] J. Pumplin, D. R. Stump, J. Huston, H. L. Lai, P. Nadolsky and W. K. Tung, JHEP **0207**, 012 (2002) [arXiv:hep-ph/0201195].

[34] S. Catani, Yu. L. Dokshitzer and B. R. Webber, Phys. Lett. B **285** 291 (1992); S. Catani, Yu. L. Dokshitzer, M. H. Seymour and B. R. Webber, Nucl. Phys. B **406** 187 (1993); S. D. Ellis and D. E. Soper, Phys. Rev. **D48** 3160 (1993).

[35] G. C. Blazey *et al.*, arXiv:hep-ex/0005012.

[36] V. Cavasinni, D. Costanzo, E. Mazzoni and I. Vivarelli, ATL-PHYS-2002-010.

[37] J. Campbell and K. Ellis, MCFM - Monte Carlo for FeMtobarn processes, http://mcfm.fnal.gov/.

[38] B. Jager, C. Oleari and D. Zeppenfeld, arXiv:hep-ph/0603177.

[39] B. Jager, C. Oleari and D. Zeppenfeld, arXiv:hep-ph/0604200.

[40] C. Oleari and D. Zeppenfeld, Phys. Rev. D **69**, 093004 (2004) [arXiv:hep-ph/0310156].

[41] S. Asai *et al.*, arXiv:hep-ph/0402254.

[42] T. Plehn, D. Rainwater and D. Zeppenfeld, Phys. Rev. Lett. **88**, 051801 (2002) [arXiv:hep-ph/0105325].

[43] K. Odagiri, JHEP **0303**, 009 (2003) [arXiv:hep-ph/0212215].

[44] W. Buchmüller and D. Wyler, Nucl. Phys. B **268**, 621 (1986).

[45] K. Hagiwara, S. Ishihara, R. Szalapski and D. Zeppenfeld, Phys. Rev. D **48**, 2182 (1993).

[46] V. Del Duca, W. Kilgore, C. Oleari, C. Schmidt and D. Zeppenfeld, Phys. Rev. Lett. **87**, 122001 (2001) [arXiv:hep-ph/0105129]; Nucl. Phys. B **616**, 367 (2001) [arXiv:hep-ph/0108030].

[47] A. H. Mueller and H. Navelet, Nucl. Phys. B **282**, 727 (1987); V. Del Duca and C. R. Schmidt, Phys. Rev. D **49**, 4510 (1994) [arXiv:hep-ph/9311290]; W. J. Stirling, Nucl. Phys. B **423**, 56 (1994) [arXiv:hep-ph/9401266]; S. Abachi *et al.* [D0 Collaboration], Phys. Rev. Lett. **77**, 595 (1996) [arXiv:hep-ex/9603010]; L. H. Orr and W. J. Stirling, Phys. Rev. D **56**, 5875 (1997) [arXiv:hep-ph/9706529]; J. Kwiecinski, A. D. Martin, L. Motyka and J. Outhwaite, Phys. Lett. B **514**, 355 (2001) [arXiv:hep-ph/0105039].

[48] T. Stelzer and W. F. Long, Comput. Phys. Commun. **81**, 357 (1994) [arXiv:hep-ph/9401258].

[49] G. Passarino and M. J. G. Veltman, Nucl. Phys. B **160**, 151 (1979).

[50] J. M. Campbell and R. K. Ellis, Phys. Rev. D **62**, 114012 (2000) [arXiv:hep-ph/0006304].

[51] V. Del Duca, A. Frizzo and F. Maltoni, JHEP **0405**, 064 (2004) [arXiv:hep-ph/0404013].

[52] R. K. Ellis, W. T. Giele and G. Zanderighi, arXiv:hep-ph/0602185.

[53] A. Denner and S. Dittmaier, Nucl. Phys. B **734**, 62 (2006) [arXiv:hep-ph/0509141].

[54] A. Denner, S. Dittmaier, M. Roth and L. H. Wieders, Nucl. Phys. B **724**, 247 (2005) [arXiv:hep-ph/0505042].

[55] Z. Bern, L. J. Dixon and D. A. Kosower, Nucl. Phys. B **412**, 751 (1994) [arXiv:hep-ph/9306240].

[56] S. Papadopoulos, A. P. Contogouris and J. Ralston, Phys. Rev. D **25**, 2218 (1982).